Development of a 3-electrode system for Gas Phase Dynamic Electrochemistry

Toks Fowowe

University College London

A Thesis submitted for the degree of Doctor of Philosophy

September 2011

I, Toks Fowowe confirm that the work presented in this thesis is my own. Where information has been derived from other sources, I confirm that this has been indicated in the thesis.

Dedicated to my immediate family here in the United Kingdom and extended family in Cameroon and Nigeria.

God Bless.

ACKNOWLEDGEMENTS

Obtaining a PhD is as much a personal challenge as it is a learning process that depends heavily on the quality of the supervision one is under. For this, I must hail great thanks to my supervisor, Dr Daren Caruana. He not only gave me the opportunity to pursue my PhD studies here at University College London but also shaped me into the scientist I am today through guidance, encouragement and endless support. I must also thank him for the constructive criticism and comments he has given on the present document, which would not have been possible without his presence.

I would like to thank past and present gas phase electrochemistry group members including Dr Dimitris Sarantaridis, Dr Emina Hadzifejzovic, Dr Jason Butler, Matthew Li, and Atif Elahi for their intellectual discussion as well as humour. My thanks are also extended to Dr Katherine Holt and her entire electrochemistry group for their useful discussions regarding all aspects of liquid phase electrochemistry.

The help received from the technical staff within the chemistry department is deeply appreciated. In particularly I must give special thanks to Mr Jim Stevenson who with his technical expertise helped to build all electrode assemblies. A day never passed when a smile was not on his face even though he knew I was about to indebt him with more work. Jim, enjoy going part time work and eventual retirement. Other members of the technical staff that I am grateful to have interacted with are Dr Steve Firth, Dave Knapp and Joe Nolan.

I would like to thank Prof John Foord and his group members, namely Dr Jingping Hu and Mr Dong Myung Shin at the University of Oxford for their assistance in using their XPS instrument.

The research council, EPSRC, is also acknowledged for their funded of this project.

I wish to thank all my friends, especially the Morales-Prado Family for showing me so much comfort and love especially during the write up period when I became very anti-social and would not explain my PhD for the hundredth time. Hopefully all your questions are answered in this thesis.

Finally, I thank my family for not only showing me the different paths to choose from in life but also supporting my choice to pursue my PhD programme.

ABSTRACT

The principles of potentiometry from liquid phase electrochemistry have already been applied to the gas phase by considering a flame as an ionised gaseous environment which can behave as a dilute electrolyte. This study focused on the design, construction and optimisation of a 3-electrode electrochemical cell for direct electron transfer in the gas phase. Three electrochemical cells were developed with the final design deemed satisfactory to conduct electrochemical measurements. Particular attention was given to the development of the reference electrode, which allows for stable voltage measurements. The reference electrodes analysed for their voltage stability and polarisability were metal wires, a dynamic type electrode and metal / metal oxide powders packed into ceramic supports. Through extensive studies, titanium wire (which forms a solid oxide layer once placed in the flame) was deemed to behave as a stable reference electrode. In conjunction with the electrode assembly and the titanium metal wire reference electrode, two metal salt clusters were individually introduced into the flame. The metal salt clusters were characterised by their reproducible electrochemical responses through cyclic voltammetry. Three negative peaks were observed when ammonium molybdate tetrahydrate was introduced into the flame. In contrast, four negative peaks were observed (at different voltage positions) when the metal salt cluster was replaced with ammonium metatungstate hydrate. The results suggest that electroreduction is indeed possible in the gas phase with reproducible Faradaic current responses being observed. The results are well supported by unambiguous correlation of the reduction potentials for peaks observed for the metal salt clusters to the vertical electron detachment energies obtained from photoelectron emission spectroscopy. The developed electrochemical cell and technique can be used to further characterise other chemical compounds.

TABLE OF CONTENTS

LIST OF FIGURES

LIST OF TABLES

1 Introduction

1.1 Aim

The principles of potentiometry from liquid phase electrochemistry have already been successfully applied to gas phase electrochemistry by our group and Goodings *et al*.[1] However, the ability to directly study electron transfer in the gas phase, particularly in flame plasmas has remained elusive. The study of electron transfer in the gas phase has almost exclusively been restricted to spectroscopic studies through electron attachment/dettachment.[2;3] It was thus the aims of this project to:

- Demonstrate electrochemical measurements can be obtained from inserting electrodes into a flame.
- Construct and develop a 3 electrode electrochemical cell capable of studying electron transfer in a flame medium. Particular attention will be placed on the reference electrode to ensure stable and reproducible electrochemical responses can be obtained.
- The electrochemical cell will be used to characterise the electrochemical reduction of two known neutral species in the gas phase, namely tungsten trioxide and molybdenum trioxide.

1.2 The Electrolyte

An electrolyte is described as the conducting medium which bridges electrodes to form a complete electrochemical cell enabling electrochemistry to proceed.[4] Electrochemistry can be defined as a branch of chemistry that investigates

electron transfer reactions that take place at the interface between two phases, most commonly between a solid and an electrolyte.[5] Traditionally, electrochemistry is performed in aqueous and non aqueous solutions but many advantages exist when the solvent is replaced with a gas. In liquid electrolytes the electrochemical reactions are limited by the electrolysis of the solvent which restricts the potential window from -2.5 V to 2.5 V in non aqueous solutions and -3 V to 3 V in ionic liquids.[6;7] The main advantage of using a gaseous plasma is the elimination of a solvent and therefore an extended potential window in excess of ± 100 V. The extension of the potential window enables chemistry at the solid-gas interface that is not possible at the solid-liquid interface.

Most electrochemical reactions between solid and liquid phases are limited by mass transport of reactants from the bulk of the solution to the electrode surface due to slow diffusion. To overcome such problems, the rotating disc electrode may be used to force convection to be the dominant mass transport mechanism. In gaseous plasmas, mass transport by diffusion is eliminated because the flow of reactant is dominated by convection through the use of a jet (hydrodynamic flow) of reactant(s) impinging onto the surface of the electrode. The increased flux of the plasma allows for a greater turnover of products. A summary of the key differences between liquid and gas electrolytes are shown in Table 1-1.

	Liquids	**Gases (plasma)**
Potential window	Defined by solvent – ca.5 V	Undetermined > ±100 V
Mass transport	Diffusion/forced convection	Migration/hydrodynamic flow
Electrochemical diffusion layer thickness	10-100 μm	1-10 mm
Typical diffusion coefficient	10^{-5} cm^2 s^{-1}	10^{-1} cm^2 s^{-1}
Dominant ions	Molecular or atomic anions and cations	Molecular or atomic cations and electrons

Table 1-1: A comparison of significant differences in liquid and gaseous (plasma) electrolytes.

1.3 Types of Plasmas

Plasmas are often described as a gaseous state of matter where the atoms or molecules have been ionised, producing an equal number of mobile ions and free electrons thus making the medium conductive. The charged species are present solely to complete the electrical circuit and transfer charge between electrodes, and therefore can be described as the background electrolyte. Plasmas can be divided into two types, either thermal or non-thermal. In a thermal plasma the electron and ion temperature are equal, whereas in non-thermal plasmas the electron temperature is typically orders of magnitude higher (see Figure 1-1, where T_e is the electron temperature and N_e is the electron density).

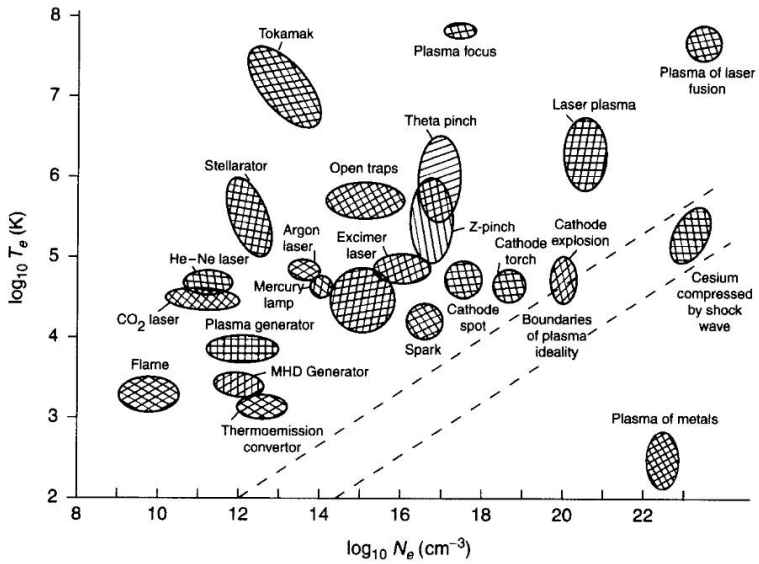

Figure 1-1: Graph showing the different plasma types and their corresponding electron temperature and density (reproduced from reference 8).

1.3.1 Review of electrochemistry in non-thermal plasmas

There are many types of non-thermal plasmas but much of the literature has focused on discharge and radio frequency (RF) generated plasmas. Discharge plasmas are created when two electrodes are separated by a gas and an electric field is applied. Different discharge plasmas can be created by varying the applied voltage. As a potential difference is applied, electrons are emitted from the cathode and form an avalanche known as the Townsend discharge.[9] As the electron avalanche progresses towards the anode, the positive ions formed from the gas are attracted to the cathode (ignoring recombination with passing electrons). As the ions strike the cathode they are able to ionise and create secondary electrons. This emission is dependent on the cathode material, type of gas and applied electric field. By applying a high enough electric field it causes one positive ion to be able to create another one electron, hence the discharge becomes self-sustaining and a Townsend discharge is formed.[9;10] Discharge plasmas have been well studied due to their wide use especially in surface modification such as etching deposition of thin films,[11] enhancing adhesive properties[12] and surface cleaning.[13]

The majority of electrochemical research using discharge plasmas has focussed on plasma electrolytic oxidation. However, some literature does exist for anodic plasma oxidation by Vennekamp and Janek. They have published work in the field of plasma electrochemistry to study morphology and film growth. They reported on the plasma electrochemical growth of ion-conducting silver chloride ($AgCl$) and silver bromide ($AgBr$) on silver (Ag) substrates using chlorine (Cl_2) and bromine (Br_2) RF plasmas.[14;15] Through the use of the solid electrolyte, Ag^+ cations were transported through the Ag anode to the interface with the plasma. The product was formed at the interface using the cations supplied by the electrode together with the anions and electrons supplied by the gaseous plasma electrolyte (Figure 1-2).

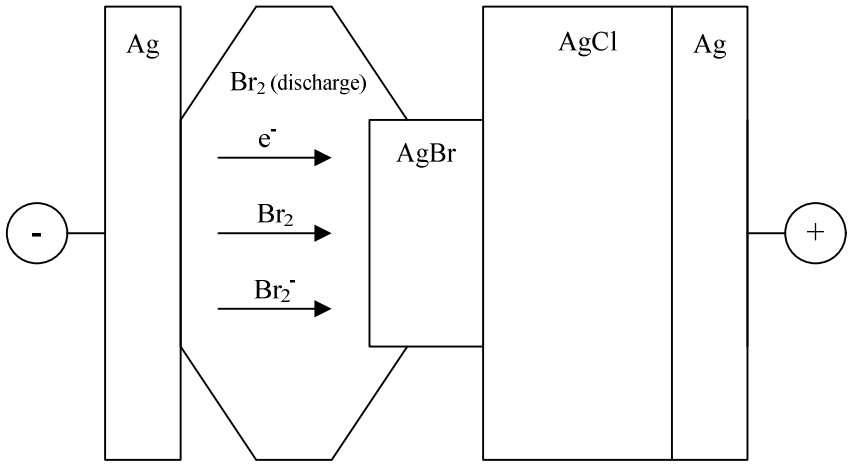

Figure 1-2: Plasma-electrochemical deposition of AgBr on Ag substrate (reproduced from reference 14).

Radio frequency plasmas can be created from either capacitively coupled or inductively coupled plasmas. In capacitively coupled RF plasmas, two electrodes are placed surrounding the gas typically with pressures 1-10^3 Pa and in some cases the electrodes have a dielectric to insulate the chamber walls. A frequency between 1-100 MHz is applied but often 13.56 MHz is used.[16] Between the electrodes the oscillating frequency accelerates both ions and electrons; however heavy ions cannot maintain the rapid oscillations of the electric field and at high enough frequencies this leaves the electrons to fully oscillate alone.[17] In inductively coupled RF plasmas, a coil is wrapped around the chamber containing a gas and a current is passed. It is the magnetic flux generated in the coil which then gives rise to a solenoid RF electric field, which then acts on the ions and electrons.[18]

In addition to the set-up described for plasma anodic oxidation, Janek and Vennekamp continued their work by including a RF plasma to research thermodynamic and kinetic properties of the plasma electrolyte.[19-21] A Ag electrode was placed opposite a graphite electrode and an induction coil was placed around both electrodes to generate a RF plasma (Figure 1-3).

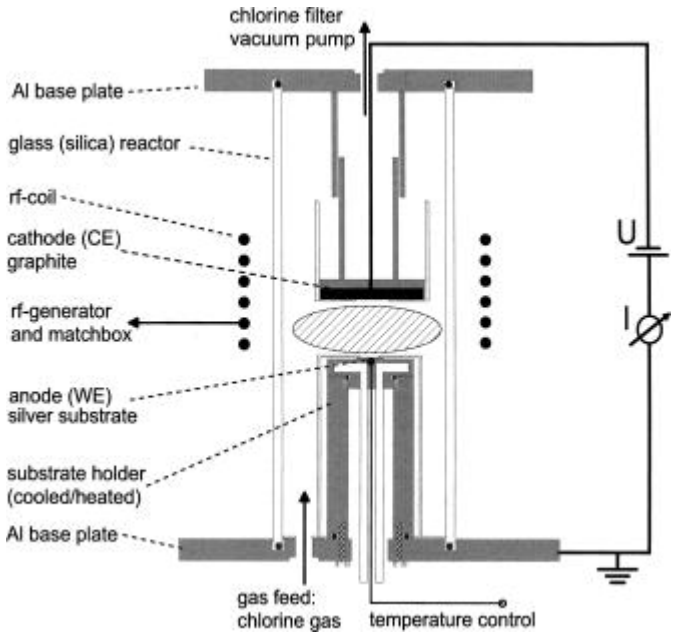

Figure 1-3: Schematic representation of the RF plasma reactor for anodic plasma oxidation in chlorine gas (reproduced from reference 20).

In their work, they demonstrated a $AgCl$ surface could be grown and Ag^+ ions could be transported through the $AgCl$ layer such that the rate limiting step was the electron transfer between Ag^+ and Cl^- ions produced in the electronegative plasma. Park and Economou developed a continuum model to also analyse the transport of charged particles within a chlorine RF plasma.[22]

Radio frequency plasmas have also been used to study the deposition of thin films composed of species introduced into the plasma. Ogumi has reported the deposition in a RF plasma over a 1-2 hours period.[23;24] An argon plasma containing zirconium tetrachloride ($ZrCl_4$) and yttrium trichloride (YCl_3) gases was created and stabilised between two parallel platinum (Pt) electrodes using a 13.5 MHz generator. A further two porous Pt electrodes were used to grow a thin layer of yttria-stabilised zirconia (YSZ) on a calcia-stabilised zirconia (CSZ) substrate. When no voltage was applied to the electrodes, no layer was grown but when a high voltage was applied (130 V), a layer was formed. They proposed the mechanism involved the reduction of H_2O to form O^{2-} ions. The

ions pass through the oxygen conducting CSZ substrate and react with the $ZrCl_4$ and YCl_3 gases in the plasma forming the YSZ layer.

1.3.2 Review of electrochemistry in thermal plasmas

An arc plasma is a common type of thermal plasma and is created in a similar fashion to discharge plasmas. A potential is applied between two electrodes to create an arc between them. The arc plasma requires a higher voltage than a discharge plasma to create the highly ionised gas. Due to their high heat source, arc plasmas have found many applications including plasma spraying, etching, chemical vapour deposition, sputtering and other industrial processes.[25-28]

The few reports of electrochemistry at a metal-plasma interface using an arc plasma are by Kawabuchi.[29] Using a hollow anode cylinder created from powdered metals namely ZrO_2, HfO_2, ThO_2, CeO_2, they created a plasma comprised of MO_2^+, MO^+, M^+ ions (where M represent the metal), and have shown that these metal oxides can be deposited on a cathode sheet. The material was identified using X-ray diffraction and deposition rates were determined by weight. Kawabuchi concluded that electrolysis was responsible for the deposition process.

A less commonly known example of thermal plasma are flames, which can be described as weak plasmas because of their relatively low extent of ionisation compared to other plasmas.[30] Flames are relatively easy to control in the laboratory and there is a large body of literature describing the physical and chemical properties mostly from spectroscopic[31] and mass spectrometry[32] investigations.

It has only recently been reported that it is possible to create a gas phase electrochemical cell by inserting two different metal electrodes into a conducting

flame.[33] By inserting electrodes that have low ionisation potentials and high melting points into a one-compartment flame, gaseous sheaths were produced at the metal surfaces due to cations being formed. In this work, Caruana and McCormack measured a potential difference between two electrodes in a fuel rich CH_4-O_2-N_2 flame. Six metals were used as electrodes and an electrochemical series was created showing the relative position of the metals measured against different electrodes. The electrochemical potentials established across the metal-gas interfaces were stable and precise, giving supporting the use of a flame plasma as an electrolyte source.

The potential difference (E_{cell}), which is an additive contribution of the Nernst potential and the diffusion (junction) potential for a whole electrochemical cell may be written as follows (equation 1-1):

$$E_{cell} = \Delta\phi^{R}_{electrode-gas} - \Delta\phi^{L}_{electrode-gas} + \Delta\phi_{diff} \quad \textbf{1-1}$$

where $\Delta\phi^{R}_{electrode-gas}$ and $\Delta\phi^{L}_{electrode-gas}$ refer to the Nernst potential difference of the right and left electrode, respectively. The final term describes the diffusion potential ($\Delta\phi_{diff}$) at a junction between two flowing flame plasmas containing a gradient of charged species and is given by equation 1-2:

$$\Delta\phi_{diff} = (\Delta\phi^{R}_{gas} - \Delta\phi^{L}_{gas}) \quad \textbf{1-2}$$

where $\Delta\phi^{R}_{gas}$ and $\Delta\phi^{L}_{gas}$ refer to the potentials of the right and left compartment, respectively, each containing different concentrations of the same charged species (homocation) or different charged species (heterocation).

Caruana and McCormack's work continued with the development of an adapted version of their one-compartment flame into a two-compartment flame (Figure 1-4). Using this they were able to introduce constant streams of additives into

either or both flame compartments, essentially allowing for the relative concentrations of cations and electrons to be manipulated independently.

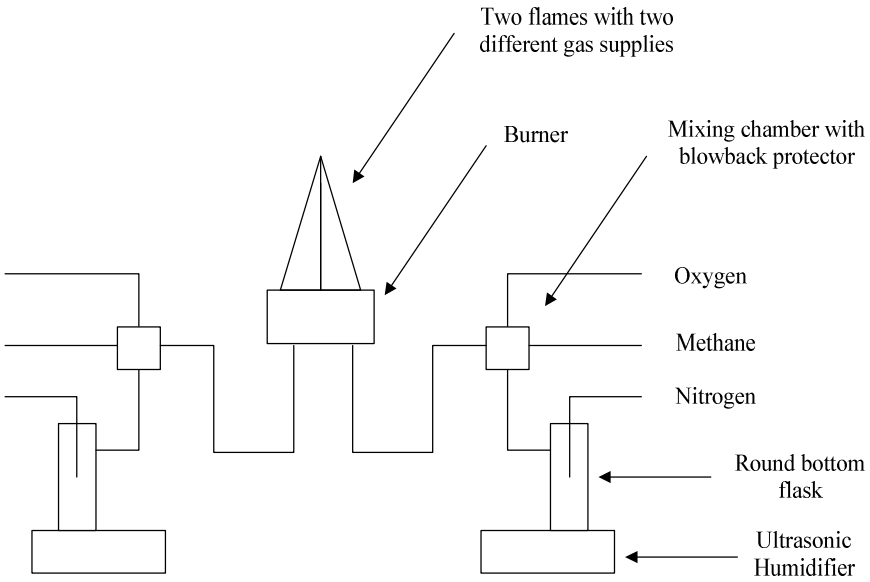

Figure 1-4: Schematic representation of the gas flow system supporting two flames (reproduced from reference 34).

This experimental set-up allowed the ratio of salt concentrations introduced into both flames to be controlled enabling a concentration gradient to be developed at the interface between the two flames, giving rise to a diffusion potential. Caruana and McCormack were able to calculate the magnitude of the diffusion potential contribution to the overall potential difference observed in a flame by applying the theory developed by Henderson for liquid-liquid diffusion potentials. An expression of the Henderson equation (1-3) that can be applied to calculate the diffusion potential of either a homocation or heterocation electrochemical cell is as follows:[34]

$$\Delta\phi_{diff} = \frac{\sum_i \frac{|z_i|u_i}{z_i}(n_i^L - n_i^R)}{\sum_i |z_i| u_i (n_i^L - n_i^R)} \frac{RT}{F} \ln \frac{\sum_i |z_i| u_i (n_i^R)}{\sum_i |z_i| u_i (n_i^L)} \quad \textbf{1-3}$$

Where n_i^R and n_i^L are the concentration of the ions and electrons in the right and left flames, respectively, u_i is the mobility of the charged species and z_i is the charge on the respective ions.

In one such study conducted by Caruana and McCormack,[34] caesium (Cs) was introduced into both flames, however only a constant concentration of 0.005 M Cs was added to the right hand side (RHS) flame while the concentration of Cs was varied in the left hand side (LHS) flame from 0.02 M to 1 x 10^{-6} M. The potential difference was measured using two similar Pt electrodes placed in the flame to complete the electrochemical cell. The predominant charged species within this cell were Cs^+ and e^- which led to a large difference in mobility between the two species, giving rise to a diffusion potential that would be the largest contribution to the potential difference observed. The Nernst potential contribution was small because both electrode reactions were under the same equilibrium conditions. Caruana and McCormack assigned a mobility of 5.0 cm^2 V^{-1} s^{-1} for Cs^+ in their study. However this value was subsequently retracted in further studies and given a more realistic mobility value of 15 cm^2 V^{-1} s^{-1}, which compared well with Mallard and Smyth[35] who calculated the mobility of a number of atomic ions in a similar flame. Due to the large difference in mobility between the cations and electrons (approximately 4000 cm^2 V^{-1} s^{-1}), the electrons travel faster than Cs^+ across a junction creating a concentration gradient resulting in a boundary developing with excess of Cs^+ on one side. This results in the development of an electric field which promotes the transfer of Cs^+ across the interface. The experimental and theoretical values for the diffusion potential were in good agreement with each other and suggest that equation 1-3 is suitable for calculating the diffusion potential

The results observed also intensified the view that the flame may be used as a suitable conducting electrolyte. Further work conducted by Goodings *et al*.[1] supported the above idea by measuring a similar magnitude of the diffusion potential generated within an electrochemical cell by placing a flame between two metal electrodes. The experimental set-up differed to that of Caruana and McCormack, making use of a metallic burner electrode supporting a flame which impinged on a metal nozzle plate electrode placed downstream to that of the burner.

A further five different electrochemical cells (two homocation and three heterocation) were investigated by Caruana. The cells investigated were: $CsOH - CsOH$, $KOH - KOH$, $CsOH - LiOH$, $KOH - LiOH$, and $KOH - CsOH$. The overall cell potential of the homocation cells were analysed with pairs of Pt and boron doped diamond (BDD) electrodes, with the magnitude of the voltages found to be on the millivolt scale. Despite the electrode material, both their gradients and intercepts were directly comparable, with the gradients being positive and the intercepts being predicted and satisfied by the Henderson equation.

The heterocation cells proved to behave differently under identical conditions. The gradient polarities for the $CsOH - LiOH$ cell were in opposite direction when pairs of Pt and BDD electrodes were used. A pair of BDD electrodes was used to investigate the two remaining electrochemical cells and the results showed a negative gradient and intercept for the $KOH - LiOH$ cell compared with a positive gradient and intercept observed for the $KOH - CsOH$ cell. To fully understand the behaviour of the heterocation cells, it was suggested that the experimental set-up should be improved with the possible inclusion of some system modeling to include thermal and convection gradients on the cation and electron flux.

Hadzifejzovic *et al*. proposed to link two theories namely, classical kinetic molecular theory and electrochemical theory of mixed potentials, to the potential

difference observed in the electrochemical cells. Hadzifejzovic *et al*. adapted Clements and Sym's expression (equation 1-4) for relating the floating potential with an in-balance electron concentration in the moving bulk plasma and adjacent to the thin sheath electrode with the electron temperature and neutral temperature in equilibrium.[36]

$$V_f \approx \frac{k}{e}(T_{e\infty} - T_{ew}) + \frac{kT_{e\infty}}{e}\ln\left(\frac{n_{e\infty}}{n_{ew}}\right) \qquad \textbf{1-4}$$

Where V_f is the floating potential, k is Boltzmann's constant, e is the electronic charge, T_e is the electron temperature, and n_e is the electron density. The subscripts ∞ and w denote values at the bulk plasma and electrode surface respectively.

The electrode temperature at the wall of the electrode was expected to be different than the temperature of the electrons in the bulk due to the cold boundary layer close to the electrode surface. For measurements described in the study, both electrodes experienced the same surface temperature and it was derived that the potential difference between the two electrodes may be given as equation 1-5:

$$E_{cell} \approx \frac{kT_{e_w^-}}{e}\ln\left(\frac{n_{e_{R\infty}^-}\, n_{e_{Lw}^-}}{n_{e_{Rw}^-}\, n_{e_{L\infty}^-}}\right) + \Delta\phi_{diff} \qquad \textbf{1-5}$$

The difference in floating potential given by equation 1-5 is dependent on the concentration of electrons in the two compartments at the electrode surface (Lw and Rw indicate the left and right electrode surface respectively) and the bulk flame ($L\infty$ and $R\infty$ indicate the left and right bulk flame) but more importantly the equation does not take into consideration the identity of the ionised species in the flame. It was therefore shown that the floating potential from the kinetic theory was unsatisfactory to explain the link between the potential differences

observed. Using an electrochemical approach, a direct link was made and a mixed potential was assigned to the potential differences observed. An equation was derived describing the overall cell potential in terms of mixed potential with the diffusion potential as shown in 1-6.

$$E_{cell} = \frac{\alpha(\Delta\phi^{\circ'}_{M/M^+} - \Delta\phi^{\circ'}_{N/N^+})}{\alpha_{e^-} - \alpha} + \frac{1}{f(\alpha_{e^-} + \alpha)}\left(\ln\frac{n_N^{\alpha} n_{e_{\bar{L}w}}^{\alpha_{e^-}}}{n_M^{\alpha} n_{e_{\bar{R}w}}^{\alpha_{e^-}}}\right) + \frac{1}{f(\alpha_{e^-} + \alpha)}\left[\ln\frac{i_{o_{N^+}} i_{o_{e\bar{R}}}}{i_{o_{e\bar{L}}} i_{o_{M^+}}}\right] + \frac{\alpha}{f(\alpha_{e^-} + \alpha)}\left(\ln\frac{n_{M^+}}{n_{N^+}}\right) + \Delta\phi_{diff} \quad \textbf{1-6}$$

Equation 1-6 describes the overall electrochemical cell potential in terms of mixed potential with the additive diffusion potential. The equation also critically predicts that the potential measured will be dependent on the identity of the cation in the two compartments (shown by the first term), potential dependence on the concentration of cations, electrons and metal atoms at the electrode surface (shown by the second term) and potential dependence on the exchange current which is dependent on the kinetics of the surface reactions and double layer potential. It has been shown through these two theories that it is not possible to simply use plasma physics to describe an electrochemical cell potential; however by incorporating both plasma physics and the mixed electrochemical theory; it is possible to take account of the potential difference measured across the electrochemical cells.

Hadzifejzovic *et al*. have also demonstrated that direct electrochemical reduction using a flame is possible.[37] A boron doped diamond electrode was placed in a flame containing copper (Cu) species. At open circuit, a layer of copper oxide (Cu_2O) on the surface of the BDD electrode was formed, most likely formed from the direct reaction with oxygen. *In situ* Raman spectroscopy was used to monitor the deposition process on the surface of the electrode through the decrease of the first order diamond peak and the increase of the characteristic

peaks of the cuprite-structured Cu_2O. During the electrochemical investigation (0 to -10 V), a reduction process from Cu^+ to Cu^0 had occurred at -1 V and -5 V which was supported through the sharp decrease in the Raman peak associated with BDD. Current measurements were also taken in tandem with the applied voltage and at -1 V and -5 V, and an increase in current was also observed.

1.4 Flames

A flame can be described as a specific type of combustion where the chemical reaction between an oxidant and fuel results in a hot glowing body of gas. Flames can be generally described either as a diffusion flame or as a premixed flame. In diffusion flames, the fuel burns as it is brought into contact with the air. The combustion processes are therefore mainly determined by the rate of diffusion of air and fuel. In larger diffusion flames, the mixing of gases may not only be due to diffusion but also turbulence and other movements of the gases. In premixed flames, the fuel and air or oxygen are simply premixed before they burn. The Bunsen burner can be used as an example to illustrate these types of flames. When the vent at the base of the burner is closed, a diffusion flame is created. In contrast, when the vent is opened and air is drawn inside, a premixed flame is created. Premixed flames have been the subject of much more scientific investigation compared to diffusion flames because they can be used to give information about a number of fundamental properties of the gas mixture such as its burning velocity and temperature.

The propagation of a flame involves the combination of fast chemical reactions, heat conduction and fluid flow. The understanding of the balance of heat and gas flow requires a detailed description of the complex chemistry and heat transfer of the flame. However the simplest flame involving oxygen and hydrogen involves the following chemical reaction (Reaction 1-1):

$$2H_2 + O_2 \rightarrow 2H_2O$$

Reaction 1-1

Although this reaction describes the overall chemistry that occurs in a flame, there are other products that are formed as intermediate species (approximately 40) which exist in the flame that play an important role in sustaining a flame.
To create a stable, steady and self sustained flame, a burner is used where the constant flow of fuel and oxidant combined at a specific point can be ignited. The flame is characterised by the upward flow of the unburned gases and the downward direction of burning gases, with the latter defining the burning velocity. Flames can also be characterised by the distribution of heat, by conduction downwards, convection upwards and radiation outwards.

1.4.1 Structure

Early researchers in flames, such as Bacon and Faraday, had noted that flames possess structure and identifiable zones, but it is only recently (through microstructure studies) that quantitative details have begun to appear. Fristom,[38;39] Gaydon[40;41] and Glassman[42] have generally described flames as having three distinguishable zones: a transport zone, primary reaction zone and a secondary reaction zone. The transport region is dominated by diffusion, thermal conduction, and thermal diffusion from the flame zone upstream. The primary reaction zone is where chemical reactions begin to take place producing reactive radicals. This zone is characterised by the temperature reaching a critical point allowing combustion to take place. The excess radicals formed in the primary reaction zone recombine toward final equilibrium in the secondary reaction zone.

1.4.2 Radical generation and ionisation processes

The flame chemistry of hydrogen/oxygen flames has been studied extensively in the past by many investigators including Eberius,[43] Brown and Fristrom.[44;45] However the mechanistic details of specific flame chemistries, especially the formation of free radicals which takes place in the primary reaction zone still remains elusive.

Free radicals species are central to flame reactions. In a hydrogen/oxygen flame, these free radical species are principally $H\bullet$, $O\bullet$, $OH\bullet$, $HO_2\bullet$. It has been shown that $HO_2\bullet$ are only present in small concentrations in near stoichiometric flames but becomes more important in hydrogen rich flames.[44]

In hydrogen/oxygen flames, the reactive radicals are produced most dominantly by Reaction 1-2 and Reaction 1-3.

$$H\bullet + O_2 \rightarrow OH\bullet + O\bullet$$

Reaction 1-2

$$O\bullet + H_2 \rightarrow OH\bullet + H\bullet$$

Reaction 1-3

The free radicals form the platform for the principal charge carriers to be created through Reaction 1-4.[46]

$$H\bullet + H\bullet + OH\bullet \rightarrow H_3O^+ + e^-$$

Reaction 1-4

The principal positively charged species is the hydronium ion, H_3O^+ and the sole negative species, e^-. The charge carriers are present in equal and small concentration, up to 10^9 ions cm^{-3}.

The rise of ionisation in flames has been known to occur through any of four separate processes, namely collisional (thermal) ionisation, electron transfer, ionisation by transfer of excitation and chemi-ionisation.

Collisional ionisation

As with most plasmas, the cations and electrons are formed predominantly by collisional (thermal) ionisation either through Reaction 1-5 and/or Reaction 1-6.

$$A + B \rightarrow A^+ + B + e^-$$

Reaction 1-5

$$A + e^- \rightarrow A^+ + e^- + e^-$$

Reaction 1-6

Where A represents an atom or molecule, A^+ represents an ionised atom or molecule, and B represents a neutral flame species.[47]

Two processes are possible by collisional ionisation, one being when an electron strikes a molecule, the majority of its kinetic energy is converted into internal energy, however when atoms or molecules collide together, only half of the relative kinetic energy can be converted. It can therefore be concluded that ionisation by electron collision occurs once the electron energy exceeds the ionisation potential as compared to higher energies needed for ionisation between atoms or molecules.

Electron transfer

Electron transfer involves the transfer of an electron from one atom to another atom or a molecule (Reaction 1-7). This reaction becomes energetically feasible at flame temperatures.

$$A + B \rightarrow A^+ + B^-$$

Reaction 1-7

Ionisation by transfer of excitation energy

Ionisation by transfer from an external source, e.g. a laser, relate to the excitation energy that is transferred from one species (B^*) to another which is adequate to cause ionisation of the atom or molecule that is the receiver (Reaction 1-8). If an energy deficit is produced, then there must be energy introduced usually by the conversion of kinetic energy into internal energy, however if there is an excess amount of energy, then this is carried away by the electron.

$$A + B^* \rightarrow A^+ + B + e^-$$

Reaction 1-8

Chemi-ionisation

Chemi-ionisation involves chemistry between neutral species that releases energy, leading to ionisation of the product species (Reaction 1-9 and Reaction 1-10). The energy needed for the reaction to occur either comes from excitation of the species or from the chemical rearrangement which may be sufficiently exothermic to cause ionisation.

$$A + B \rightarrow C^+ + D + e^-$$

Reaction 1-9

$$A + B \rightarrow C^+ + D^-$$

Reaction 1-10

Ionisation of ions with additives

The addition of small quantities of additives that have low ionisation potential, such as alkali metals can greatly enhance ionisation in the product gases of a flame. According to Jensen and Padley,[48] chemical processes were responsible for alkali metal ionisation, however was later retracted and it is now commonly accepted that the rise of ionisation of alkali metal occurs predominantly through thermoionisation by the electronically excited stage of the metal atom (A^*) as shown in Reaction 1-11.[47;49;50] The ionisation of other metals occurs through mainly collisional ionisation.

$$A + B \leftrightarrow A^* + B$$
$$A^* + B \rightarrow A^+ + e^- + B$$

Reaction 1-11

1.5 The Langmuir Probe

Plasma diagnostic tools are of great importance in the study of the gaseous electrolyte of flames. They are not only used to study the identity and position of ions but also the concentrations. Microwave absorption techniques have been used in the past to study ion and electron concentrations because they do not disturb the flame plasma; however it is limited through only being able to measure the average density of ions and electrons across a flame. Ideally in premixed flames, the primary reaction zone is the area of interest.[40] To overcome such problems, Langmuir probes were introduced, dating back to the pioneering work of Mott-Smith and Langmuir.[51] The electrostatic probe has been

extensively used ever since to determine the ion and electron concentration and electron temperature.[36;52-56]

The probe is usually a thin cylindrical wire or a small sphere which is inserted into the flame. A negative or positive voltage is applied to the wire relative to a second much larger electrode in the flame.[40] This set-up enables a current vs. voltage (probe characteristic) curve to be obtained, shown in Figure 1-5.

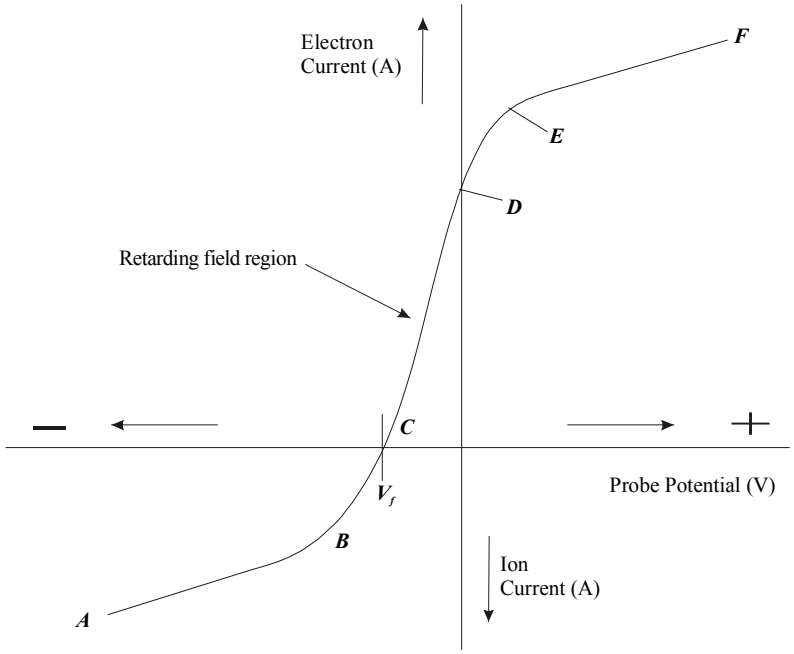

Figure 1-5: Current-voltage characteristics of a Langmuir probe inserted into a flame.

Between region *A* and *B* the probe is biased strongly negative with respect to the plasma which leads to electrons being repelled (Figure 1-6). Some electrons also reach the surface under these circumstances; however this is insignificant because the current to the probe is almost solely due to positive ionic current which is a measure of the positive ion concentration in the plasma or flame.

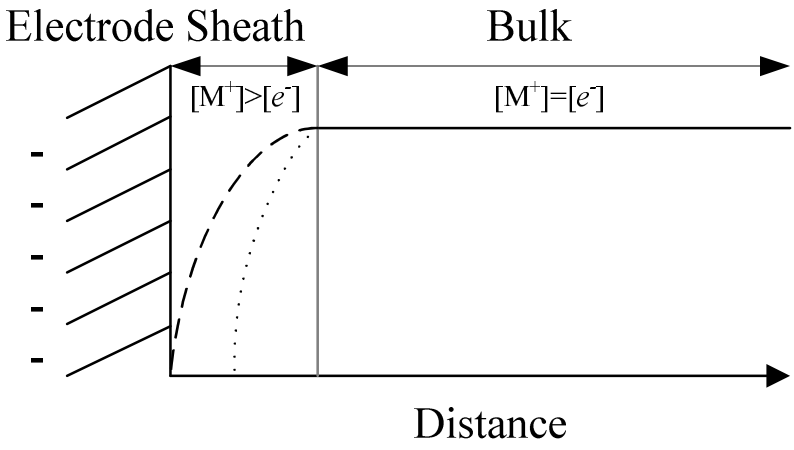

Figure 1-6: Distribution of charge (····e^-, – – M^+) approaching a negative probe.

As the potential is made less negative the ionic current falls, related to a reduction in the flux of positive ions reaching the probe. In the region between *B* and *C*, the electron current becomes observable and at point *C* the electron current becomes equal to the positive ion current. This equivalence point is known as the floating potential, V_f and can also be defined as the potential at which the net current is zero, i.e. the cation (i_{M^+}) and electron current (i_{e^-}) are equal. Between *C* and *D*, more electrons than positive ions reach the probe causing a reverse in the direction of the current. The probe is at the plasma potential at point *D* and receives thermal ions and electron currents randomly. Between the region *E* and *F*, the probe potential is sufficiently positive, leading to all the electrons within the plasma sheath being collected at the surface of the probe under the action of the attractive potential (Figure 1-7).

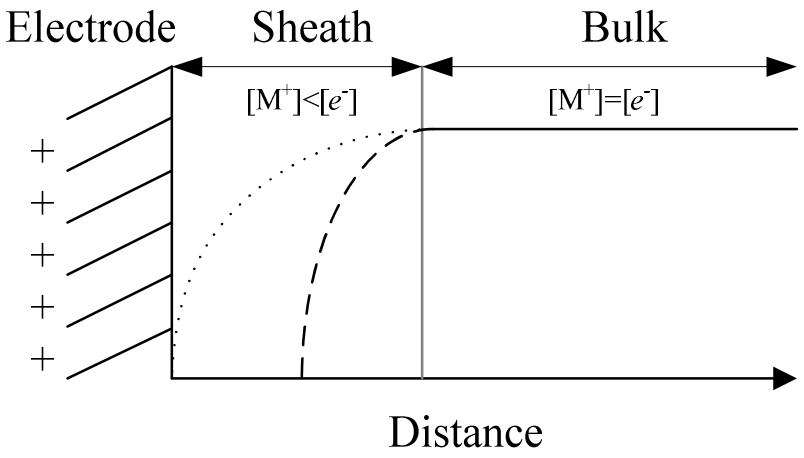

Figure 1-7: Distribution of charge (····e^-, – – M^+) approaching a positive probe.

The sheath region of the probe is different when the polarity is changed. With a positive electrode, the sheath region is much bigger due to the mobility of electrons (which is significantly higher than cations), causing a larger flux of electrons to be attracted by the electric field and entering the sheath from the bulk as compared to cations. This difference in sheath size is also responsible for the difference in the measured current. A larger electron current is measured because more electrons are present around the probe surface as compared to the measured cation current which is small due to less cations being present around the probe surface. The region of the curve corresponding to the retarding field region can be used to determine the electron temperature.

Various authors have attempted to measure ion concentration in flames using the Langmuir probe and have reported values as high as 10^{17} ions m^{-3}.[57] However the technique has been criticised because of effects such as flame disturbances and significant drifting during measurements.[58] King and Calcote[59] investigated the effect of probe size on ion concentration measurements in flames and showed that a larger probe measured a lower value of ion concentration which meant that the measured value of ion concentration had to be corrected for probe size in order to obtain a true value in the plasma. Recently Goodings has used both mass

spectrometry and electric probes to study and evaluate the products of ionisation, ions and free electrons in flames.[30;60]

1.6 Electrode–Electrolyte Interface

Modern electrochemical studies are based upon interfaces between electrical conducting or semiconducting solids and liquid phases. However as reviewed previously, the interface between a conducting solid and a gaseous plasma offers an innovative interface for electrochemistry to occur. Although the solid-liquid interface has been studied extensively, the same does not apply for the solid-gas interface. Here, the similarities and contrasts between the two interfaces are described.

The solid-liquid interface has been likened to that of a capacitor. A capacitor can be described as an electrical circuit element composed of two metal sheets separated by a dielectric material. The behaviour of a capacitor is described in equation 1-7.

$$\frac{q}{E} = C \qquad \textbf{1-7}$$

Where q is the charge stored on the capacitor, E is the potential across the capacitor, and C is the capacitance. Once a potential is applied across a capacitor, charge will build up on its metal plates until q satisfies equation 1-7. During the charging process, the charge on the capacitor consists of an excess of electrons on one plate and a deficiency of electrons on the other plate.

When a potential is applied to a solid electrode, a charge will exist on the electrode, q^S and the exact opposite but equal charge in the liquid, q^L. The charge on the solid electrode, q^S represents an excess or deficiency of electron

and is located very close to the surface of the electrode. In contrast, the charge in the liquid, q^L represents an excess of cations or anions in the vicinity of the electrode surface.[61] The electrical double layer, first proposed by Helmholtz in 1953 has been used to describe the arrangement of charged species and oriented dipoles existing at the solid-liquid interface.

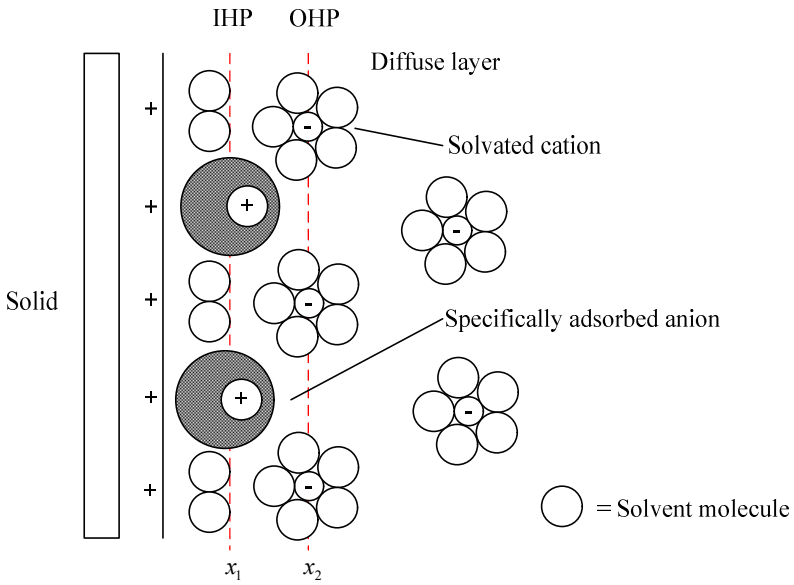

Figure 1-8: Proposed model of the double-layer region under conditions where anions are specifically adsorbed.

The electrical double layer is made of two layers, the inner layer and diffuse layer. The inner layer (closest to the electrode) contains specifically adsorbed solvent molecules and sometimes other ions or molecules. The locus of the electrical centres of the specifically adsorbed ions is called the inner Helmholtz plane (IHP), which is located at a distance x_1. The outer Helmholtz plane is located further away than the IHP and consists of non-specifically adsorbed solvated ions that can only approach the metal to a minimum distance x_2. The solvated ions only interact with the charged metal through long-range electrostatic forces. The non-specifically adsorbed ions are distributed throughout the diffuse layer which extends from the OHP into the bulk of the liquid.

The structural interface between a solid and gas is similar but much simpler than that between a solid and liquid interface, with the vicinity close to the electrode surface being known as the sheath. The electrostatic sheath contains only ions and electrons and can be seen as analogous to the double layer region. The dependence of the sheath size has previously been discussed in Section 1.5. Furthermore, as similarly observed at the solid-liquid interface, a potential drop, known as the cathodic drop, also exists at the solid-gas interface. In the presence of no solvent, Vijh has demonstrated a method to calculate the cathodic drop potentials by treating the metal and plasma as two isolated plasmas, separated at an interface.[62] By calculating the plasma resonant frequency at this interface, Vijh showed (experimentally and theoretically) that the cathodic drop arising from a metal-liquid interface (with a vacuum solvent) was the same as the plasma surface frequency of two plasmas in contact.[63]

At both the solid-liquid and solid-gas interfaces, two types of processes can occur resulting in a current response. Non-Faradaic processes can occur by changing the electrode potential or composition of the electrolyte. Examples of processes that result in non-Faradaic currents include adsorption or desorption. Importantly, non-Faradaic currents are not associated with charge transfer across the interface. Charge transfer reactions cause Faradaic currents to be observed and are governed by Faraday's laws, the amount of chemical reaction is proportional to the amount of electricity passed. It is therefore our primary interest to be concerned with Faradaic processes occurring at the solid-gas interface.

The Marcus Theory can be used to describe the movement of Faradaic current between solid-liquid interfaces as shown using the energy level diagram in Figure 1-9.

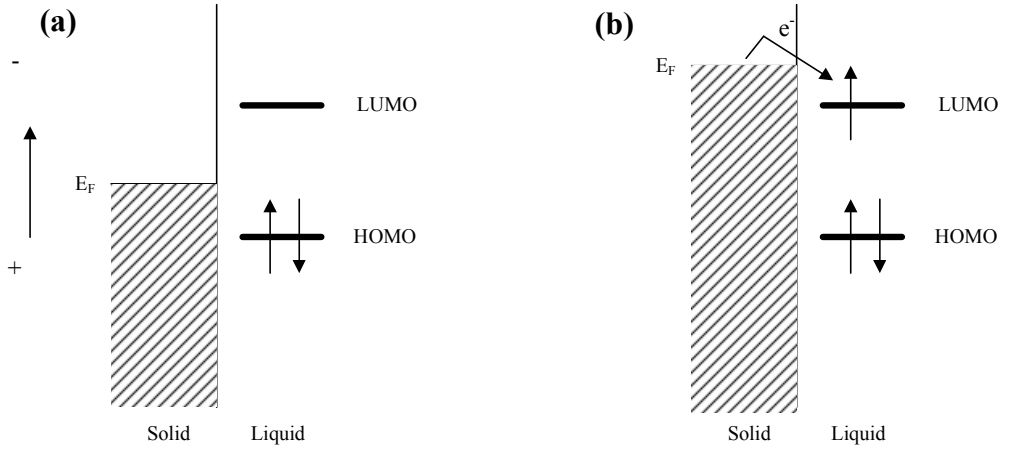

Figure 1-9: Electron transfer and energy levels (a) the electrode potential is insufficient to drive the reduction of a species and (b) at a more reductive potential where the electrode process becomes thermodynamically favourable.

The electrical potential applied to the solid electrode acts to increase or decrease the energy of the Fermi Level. In Figure 1-9a the energy state of the LUMO is higher than that of the solid's Fermi Level. Electrochemical reduction is therefore not favourable in this scenario because electrons in the solid do not have a high enough energy to transfer across the interface. To enable electrochemical reduction to occur, the electrode potential must be made more negative allowing the Fermi Level of the solid to be higher than that of the LUMO as shown in Figure 1-9b. The above energy diagram can also be applied to gaseous species that are adsorbed onto the surface of the working electrode and are then subsequently reduced.

A similar description of the electron transfer in the gas phase has not yet been completed; however analogous non-interfacial techniques, most notably photoelectron emission spectroscopy, has been used to study the attachment of electrons to neutral molecules and clusters in the gas phase. The electron affinity is the basic quantity in the relation between a neutral particle and its negative ion. The adiabatic electron affinity of a particle is formally defined as the energy difference between the neutral and the anion in their respective ground states. The vertical detachment energy is used to distinguish the geometry between the

anion and the neutral. The vertical detachment energy is obtained from the Franck-Condon transition in photodetachment from molecular anions, in complete analogy to adiabatic and vertical ionisation energies in photoionisation.[3] In the cases where very little geometry change takes place, the adiabatic electron affinity can be measured directly from optical adiabatic electron affinity.[64] A corresponding energy level diagram is presented further in this thesis (Chapter 7) demonstrating the proposed reduction of species in the gas phase.

Cyclic voltammetry is the most commonly encountered technique used to study dynamic electrochemistry between solid-liquid interfaces. This extremely useful diagnostic technique will be used here to study the electron attachment of redox active components added to the flame.

1.7 The Polarisable and Non-Polarisable Electrode

Generally two types of electrodes are used in electrochemistry, polarisable and non-polarisable electrodes. A polarisable electrode, i.e. a working electrode, has an interface of high resistance, allowing small passages of current to generate a high potential across it. A non polarisable interface can be likened to one of low resistance, effectively allowing significant current to pass with only minimal change of the potential across the interface. The stable potential of the non-polarisable electrode allows for the potential at the working electrode to be determined accurately. The current-potential relationship for both a non-polarisable and a nonpolarisable interface is shown schematically in Figure 1-10.

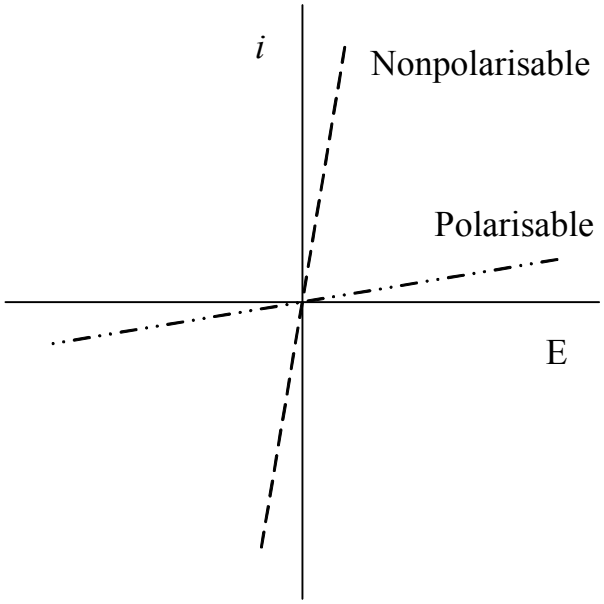

Figure 1-10: Schematic current-potential plot for polarisable and nonpolarisable interfaces.

The polarisation of a working electrode always occurs against a reference electrode. A reference electrode can also be defined as an electrode which has a stable and a well-known electrode potential referenced against the standard hydrogen electrode (0 V). This high stability of electrode potential is achieved through the reference electrode possessing the non polarisable interface.

The chemical basis of the non polarisable electrode is a redox reaction, around which the whole edifice of electrode potential rests. An example of a good reference electrode in the liquid phase is the saturated calomel electrode (SCE):

$$Hg_{(l)} \mid Hg_2Cl_{2(s)} \mid KCl_{(sat'd)}$$

Where Hg represents mercury, Hg_2Cl_2 represents mercurous chloride (calomel) and KCl represents potassium chloride.

The redox reaction in the SCE is as follows equation 1-8:

$$Hg_2Cl_2 + 2e^- \rightarrow 2Cl^- + 2Hg \quad \textbf{1-8}$$

This reaction is characterised by fast electrode kinetics, meaning that a sufficiently high current can be passed through the electrode with the 100% efficiency of the redox reaction. The mercury and calomel are both pure phases, so their activities are both unity and therefore the reference electrode potential will be independent of the amounts of the two solids. The Nernst equation 1-9 below shows the dependence of the potential of the SCE on the activity or effective concentration of chloride ions:

$$E_{cell} = E_{eq} - \frac{RT}{nF} \ln a_{Cl^-}{}^2 \quad \textbf{1-9}$$

By maintaining the concentration of the chloride ion (through a constant surplus of KCl crystals to ensure saturation), the potential of the SCE will also have a constant value. This makes the redox couple suitable for use as the basis of a reference electrode.

1.8 Thesis summary

The initial objective of this thesis is to develop and understand how a non-polarisable electrode interacts with a flame medium, similar to that of a SCE in the liquid phase. Chapters 2, 4, and 5 describe and critically analyse (through electrochemical measurements) the different types of reference electrodes that have been developed. The development of the electrochemical assembly (Chapter 6) will then be described in detail before dynamic electrochemistry results are reported (Chapter 7), in which known additives were introduced into the flame with the sole aim of characterising them through electrochemical reduction.

2 Experimental Set-up, Theory and Techniques

2.1 Introduction

This chapter shall begin by focussing on the design of the burner with which a flame was supported. Following on from this, the main experimental techniques used in this work will be described. This will include the electrochemical techniques, namely, cyclic voltammetry, zero current potentiometry, and chronopotentiometry. The other techniques described here (Raman Spectroscopy, X-ray Photoelectron Spectroscopy, X-ray Diffraction, and Thermal Analysis) were used to characterise and determine the chemical composition of the electrodes. A Thermal Imaging Pyrometer was used to measure the electrode surface temperature in the flame.

2.2 Materials

Three gases were used in creating a flame, hydrogen (99.9% purity) as a fuel source, oxygen (99.9% purity) as an oxidant and nitrogen (99.9% purity) acting as a diluent. All compressed gas cylinders were supplied by BOC. As extra safety measures, in addition to the blow back protectors which will be discussed below, both the hydrogen and oxygen gas cylinders were fitted with flashback arrestors to prevent an ignited flame from burning back into the cylinder(s) and causing an explosion. The flow ranges for each gas were controlled by digital mass flow controllers (Brooks® SLA5850) and/or manual mass flow controllers (Platon).

2.3 Burner

A Méker type burner was used throughout this study. The burner was designed to support two (dual) premixed flames from two independent gas inlets as shown in Figure 2-1.

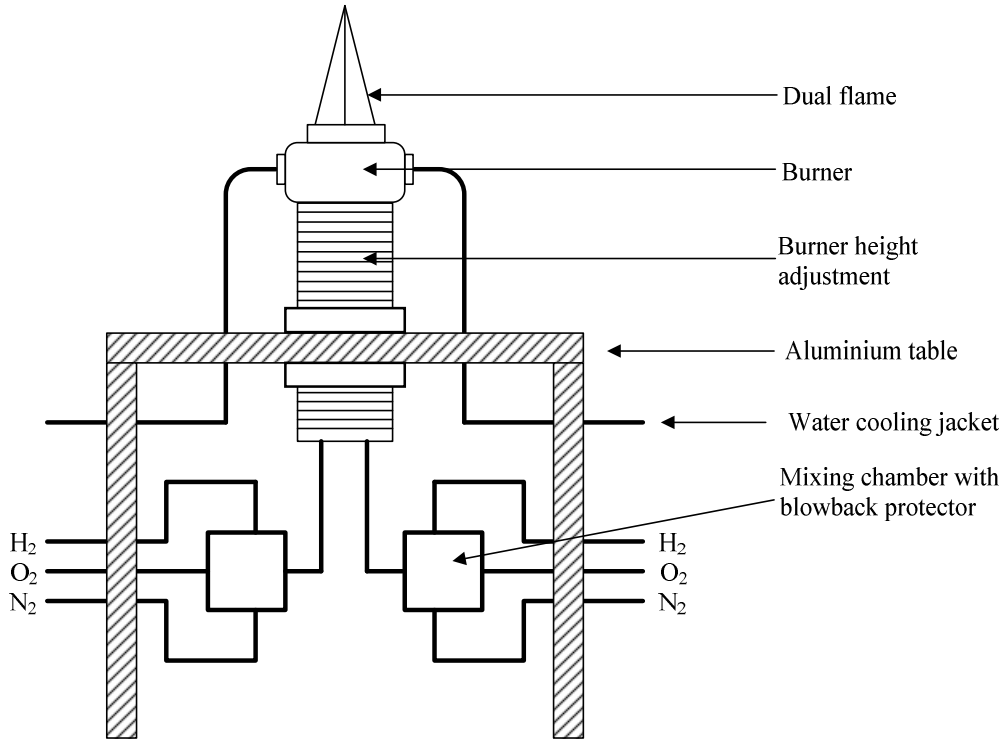

Figure 2-1: A schematic diagram representation of the two gas flow systems feeding the burner system producing a dual flame.

The burner was made using stainless steel and mounted vertically onto an earthed aluminum table. Flexible copper piping (approximately 2 meters in length) was used to carry the gas from the cylinders to the mixing chambers. Another 2 meters in length of stainless steel tubing was used to transport the gas from the mixing chamber to the burner to ensure thorough mixing of the gases and drying of the lines after additives were introduced (discussed below). A water cooling jacket was used to remove the excessive heat produced from the combustion process taking place at the burner. The mixing chambers were fitted with safety

blowback protectors to protect any flash backs occurring at the burner from reaching the gas cylinders.

In some cases, the two gas flow systems were joined in order to produce a single flame burner as shown in Figure 2-2. This was done to equalise the pressure on both sides of the flame. In this instance, the flame was described as a homogeneous flame with a single gas mixture.

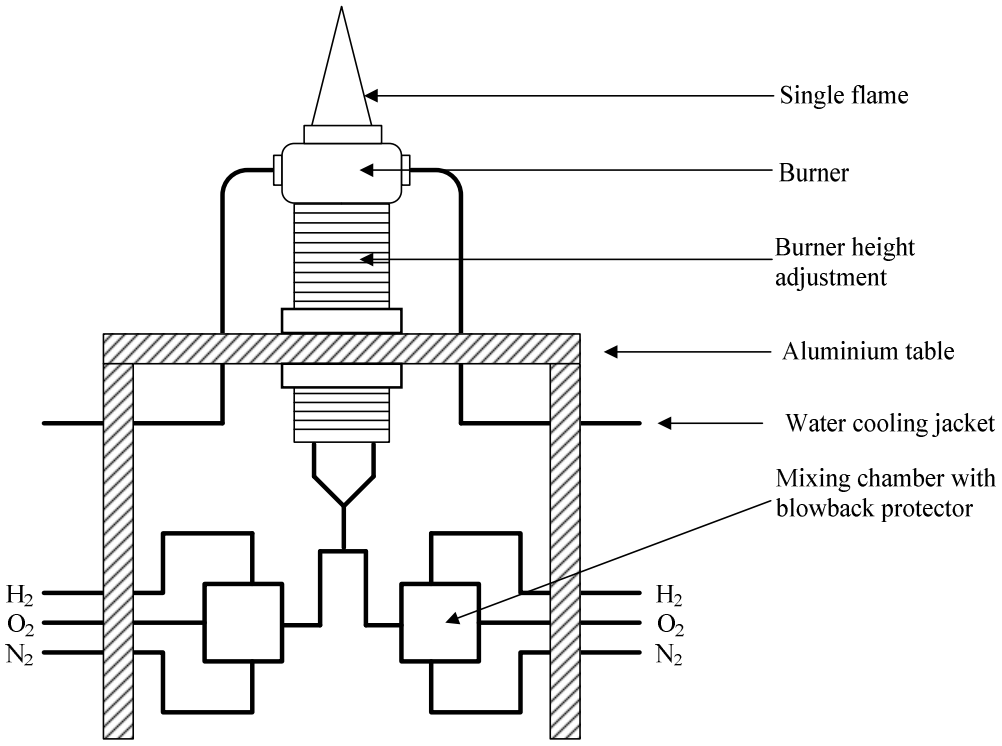

Figure 2-2 A schematic diagram representation of the two gas flow system feeding the burner system producing a homogenous single flame.

The nitrogen (N_2) gas line was modified just before the mixing chamber to allow additives in solution to be added to the flame. The solutions were introduced into the gas stream in the form of an aerosol created by an ultrasonic humidifier (Index Ltd. UK). The solutions (10-20 cm^3) made with deionised water from Milli-Q plus (> 0.05 S cm^{-2}) were added to round bottomed flasks through a side injection port by a syringe during an experiment (see Figure 2-3).

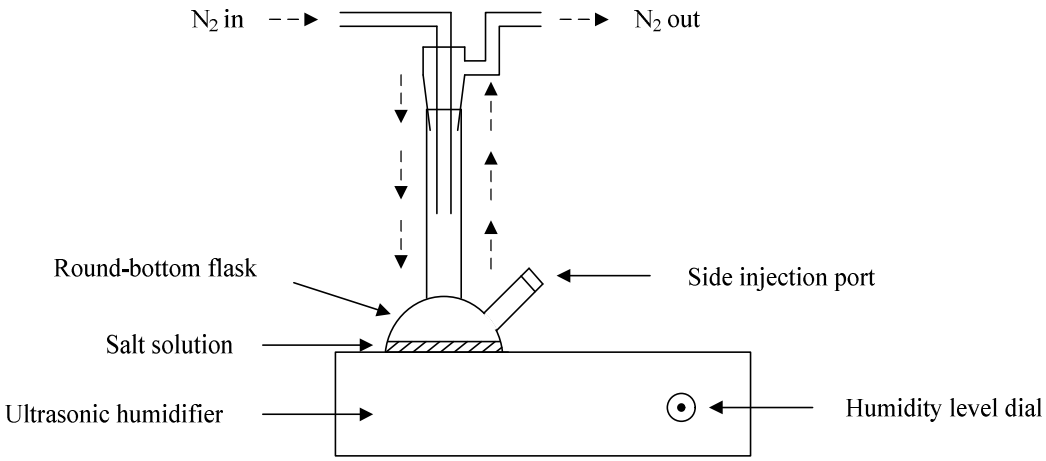

Figure 2-3: Schematic diagram representing the introduction of additives in solution into the flame via the N_2 gas line using an ultrasonic humidifier.

When a bare flame was needed (no additives), the gas lines were dried by passing N_2 at 0.2 L min^{-1} for a minimum of 2 hours prior to an experiment.

A burner top-plate was machined from an electrically insulating ceramic (MACOR®) purchased from Corning (RS). An electrically insulating burner top was essential for this work because a conducting burner top would actually bridge the two flames together and cause erroneous measurements and drift. The gas exit from the burner top was from two groups of 15 holes (0.5 mm diameter), arranged in an ordered, symmetrical fashion with both groups centrally aligned to form a hexagonal array (see Figure 2-4).

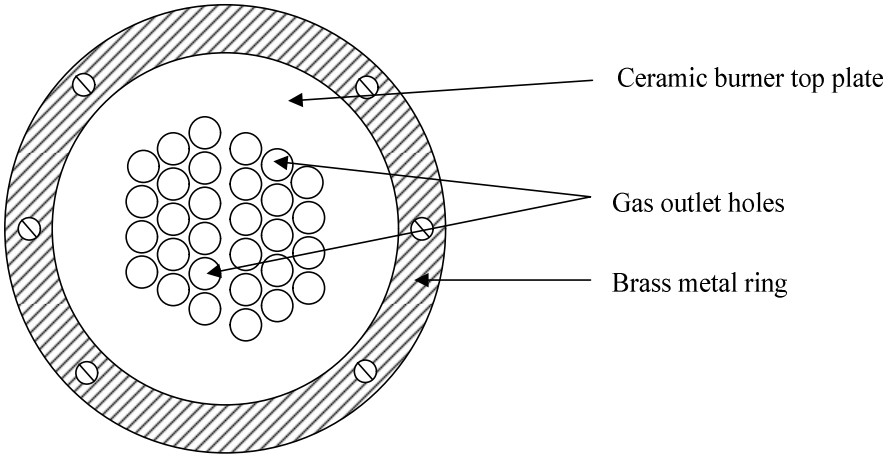

Figure 2-4: Top view schematic diagram representation of the burner set-up (not to scale).

The top plate was cleaned by skimming the top surface regularly. However, when the identity of an additive changed or when a bare flame was needed skimming took place immediately to reduce the possibility of cross contamination. In conjunction with this, the holes were carefully cleaned using a 0.5 mm diameter drill. The electrodes were positioned in the flame using two *x*, *y* and *z* micropositioner platforms with the horizontal axis of each platform motorised (PI, supplied by Lambda scientific, UK) and controlled remotely by a computer.

2.4 General procedure for turning flame on/off

With safety glasses worn during the entire experiment, the single and dual flames were turned on and off as follows: To start with, a steady total flow of 3.2 L min^{-1} of N_2 was passed through the burner. The flow of hydrogen (H_2) was then turned up to the desired flow (usually between 1.6 - 2.0 L min^{-1}). The gases were ignited, creating a diffusion flame. At this point, the oxygen (O_2) flow was increased to the desired flow (usually between 0.8 - 1.0 L min^{-1}). To safely turn off the flame, the flow of O_2 gas was slowly reduced to zero before allowing two minutes to pass to ensure all the O_2 had passed. The H_2 gas flow was then

also reduced to zero, before allowing the N_2 to run at 0.2 L min^{-1} for 30 minutes or for 2 hours after an additive-introduced flame experiment.

2.5 Electrochemical Techniques

2.5.1 Cyclic Voltammetry

2.5.1.1 Theory

Cyclic voltammetry (CV) is a type of potentiodynamic electrochemical measurement commonly used in electrochemistry. The main purpose of using this technique is to obtain detailed information about the electron transfer processes occurring within a conducting medium as demonstrated in equation 2-1.[65] The technique achieves this by measuring a current as a function of an applied voltage.

$$O_{(aq)} + ne^- \leftrightarrow R_{(aq)} \qquad \textbf{2-1}$$

In linear sweep voltammetry, the potential of the working electrode is ramped from an initial potential, E_1 to a final potential, E_2. However during CV, although the potential is ramped from E_1 to a switch potential, E_2, it is then reversed by ramping back down to E_1 as shown in Figure 2-5.

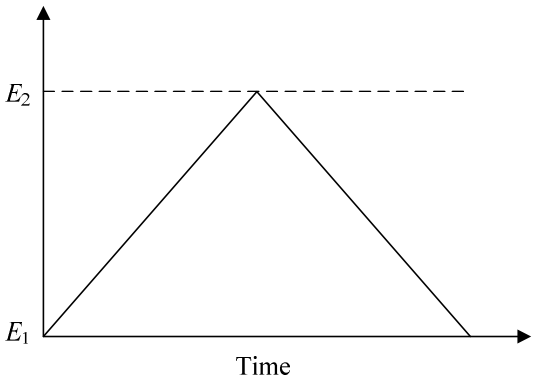

Figure 2-5: Variation of the applied potential as a function of time in a cyclic voltammogram experiment.

The applied potential is a function over which the cycle is run, known as a sweep, and this is controlled by the scan rate. The scan rate (υ) can be defined as the rate at which the potential of the electrode is changed, i.e. $\upsilon = \left(dE/dt\right)$.[4;6] The scan rates used for the forward and backward scans are usually the same unless stated otherwise and is cited as a positive number regardless of scan direction. The current response resulting from the applied voltage is shown in Figure 2-6. This is a typical response of a thermodynamically reversible CV in liquid electrochemistry.

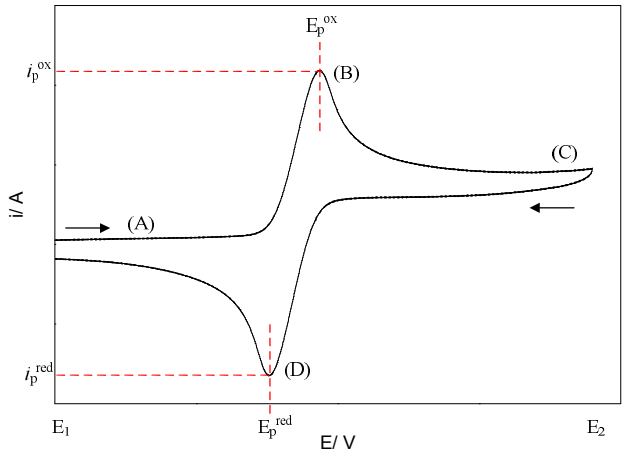

Figure 2-6: An example of a cyclic voltammogram for a reversible process in a liquid for a freely diffusing species.

The behaviour of the response can be described as follows. At point A, only the reduced species (R) of the redox couple is present and no current is observed because the initial potential applied is lower than the standard potential of the redox couple, thus no electron transfer can occur. As the potential is increased on the forward scan of the CV (upper, oxidative peak) and approaches the redox potential, an anodic current is measured and increases with potential. At point B, the redox potential is sufficiently positive that any R that reaches the electrode surface is instantaneously oxidised to the oxidised species (O), i.e. $R \rightarrow O + n\,e^-$. The current is now limited on the slowest rate of mass transport which is diffusion. Due to diffusion-controlled mass transport, rapid replenishment of new, fresh analyte to the electrode surface cannot occur; therefore, the current begins to decrease and reaches point C. As the scan is reversed, the opposite process happens. At point D, the redox potential is sufficiently negative that any O that reaches the electrode surface is instantaneously reduced to R, i.e. $O + n\,e^- \rightarrow R$. At the end of the CV, there is still a small amount of current which indicates a small amount of material in the vicinity of the electrode surface has still not been reduced but if the potential of the electrode was forced to a more negative potential all the material would be reduced and thus a zero current would be observed.[4;65;66]

The shape of the voltammogram can indicate amongst others diagnostic tests whether the redox couple is reversible or irreversible. A reversible redox couple with fast kinetics show significant current flows at small overpotentials and the magnitudes of the two peaks formed on the forward and backward scans are identical. A one electron transfer reversible redox couple should have the ratio of the peak current, i_p for both the oxidative and reductive scans be equal to one as shown in equation 2-2:[6]

$$\frac{i_p^{ox}}{i_p^{red}} = 1 \qquad \textbf{2-2}$$

2.5.1.2 Procedure/Data acquisition

The electrochemical cell used in theses studies consisted of three electrodes; counter electrode (CE), reference electrode (RE), and working electrode (WE) which were introduced into the flame (see Figure 2-7)

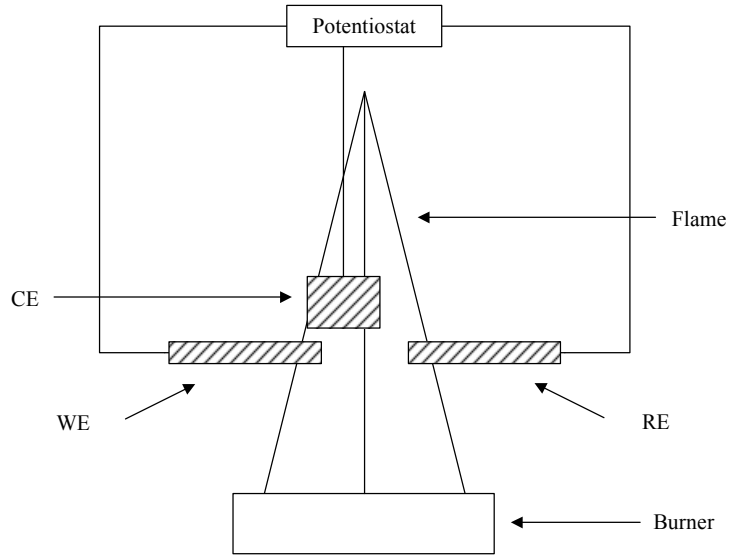

Figure 2-7: Schematic diagram of the electrode arrangement used for the measurement of current.

Chapter 6 will describe in greater detail the design and orientation of the electrochemical cell. All electrodes were connected to a potentiostat (see Figure 2-8) with a 100 V compliance voltage (Autolab PGStat100, Eco Chemie B.V. supplied by Windsor Scientific Ltd., UK) and current measurements as a function of applied voltage were recorded. A Potentiostat is extremely useful for investigations of reaction mechanisms related to redox chemistry.

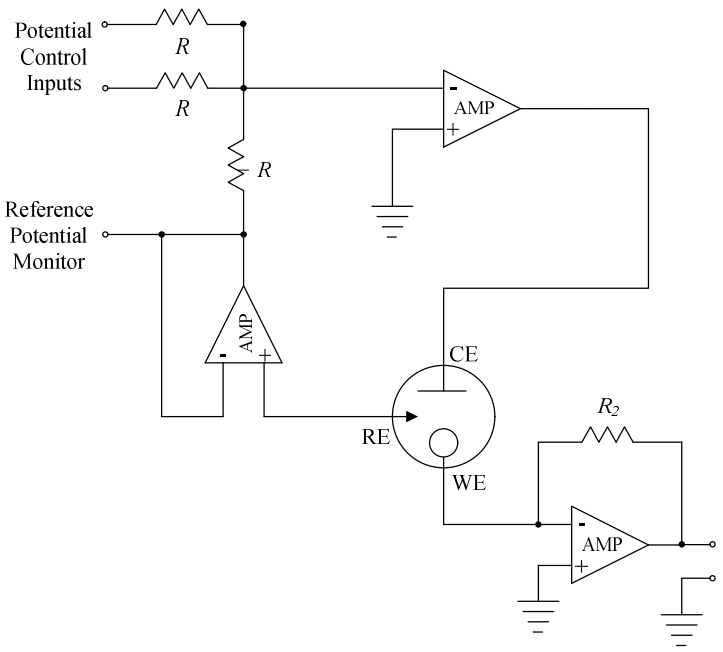

Figure 2-8: Potentiostat circuit for control of the reference electrode potential in a three-electrode cell (reproduced from reference 4).

2.5.2 Zero current redox potentiometry

2.5.2.1 Theory

Potentiometry is an electro-analytical method in which a potential is measured under the conditions of no current flow.[67] The measured potential may then be used to determine the concentration of some component of the analyte solution. The potential that arises in the electrochemical cell is the result of the Gibbs energy change that would occur if the reaction were to occur under equilibrium conditions.[5]

A typical electrochemical cell is shown in Figure 2-9. The cell comprises of two half cells, with each cell comprising of a redox couple. The electrode from each half cell is connected to a high impedance voltmeter which enables the cell

potential to be determined accurately at zero current. A salt bridge consisting of saturated salt solution completes the electrochemical cell to enable ionic charge to transfer between the two half cells.

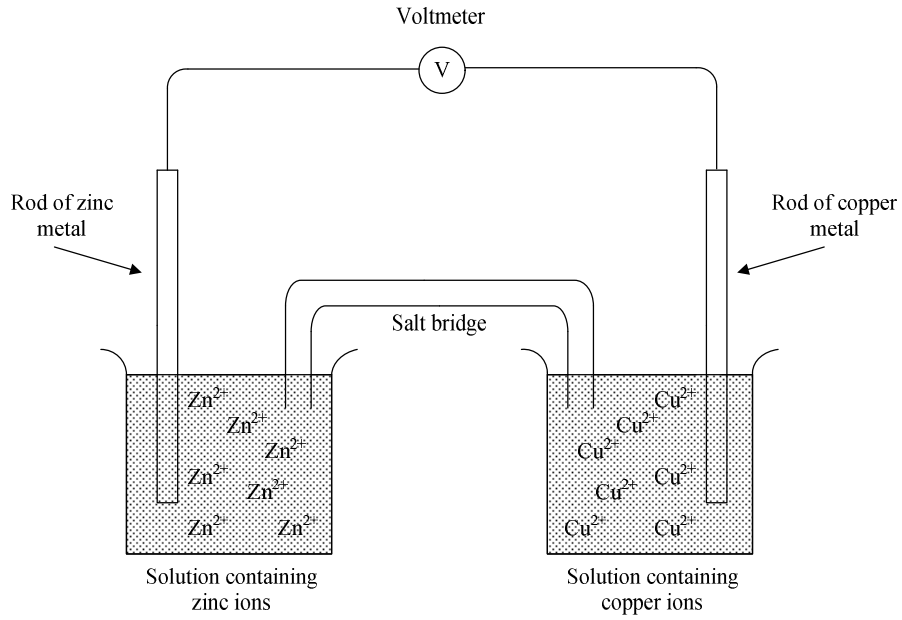

Figure 2-9: Schematic representation of the Daniell cell suitable for equilibrium electrochemical measurements.

However, if current were to flow, this cell reaction would proceed, oxidation would occur at the zinc side of the electrode (dissolving) because it is the more negative vs. SHE of the two cells, as follows (Reaction 2-1):

$$Zn^{0}{}_{(s)} \rightarrow Zn^{2+}{}_{(aq)} + 2e^{-}$$

Reaction 2-1

In addition, reduction will occur at the copper side of the electrode (depositing), as follows (Reaction 2-2):

$$Cu^{2+}{}_{(aq)} + 2e^{-} \rightarrow Cu^{0}{}_{(s)}$$

Reaction 2-2

Both half cells are complementary to each other and therefore the current flowing through both half cells will be equal and opposite of each other, giving the following overall reaction:

$$Zn^{0}_{(s)} + Cu^{2+}_{(aq)} \rightarrow Zn^{2+}_{(aq)} + Cu^{0}_{(s)}$$

Reaction 2-3

By convention, the more positive electrode is the right hand electrode (cathode), while the left hand electrode (anode) is the more negative. It is this difference in potential between the right hand (E_{RHS}) and left hand (E_{LHS}) electrodes which gives the electromotive force or cell potential (E_{cell}) shown in equation 2-3.

$$E_{cell} = E_{RHS} - E_{LHS} \qquad \textbf{2-3}$$

If the cell reaction was allowed to occur, the Gibbs energy of cell reaction (ΔG_{cell}) could be calculated from the cell potential to yield important thermodynamic information[5] through equation 2-4:

$$\Delta G_{cell} = -nFE_{cell} \qquad \textbf{2-4}$$

Where n is the number of electrons transferred in the cell reaction (if it was allowed to proceed) and F is the Faraday constant, which represents the charge on 1 mole of electrons.

According to the second law of thermodynamics, a spontaneous process at constant temperature and pressure will result in a decrease in Gibbs energy, thus having a negative ΔG_{cell} because the cell potential is by definition always positive (depending on how the electrical wires of the voltmeter are connected).[5]

2.5.2.2 Procedure/Data acquisition

For the experiments in the flame, the electrochemical cell consisted of two electrodes; placed 5 mm apart from each other. They were introduced into the flame at a height of 10 mm (see Figure 2-10) because this was found to be the optimum position with respect to stability of the measurements and noise effects. A data acquisition (DAQ) card (NI USB-6215, National Instruments) with an input impedance above 10 GΩ was used to measure the potential difference between the two electrodes. A LabVIEW Signal Express LE interactive software (National Instruments) was used to log the data.

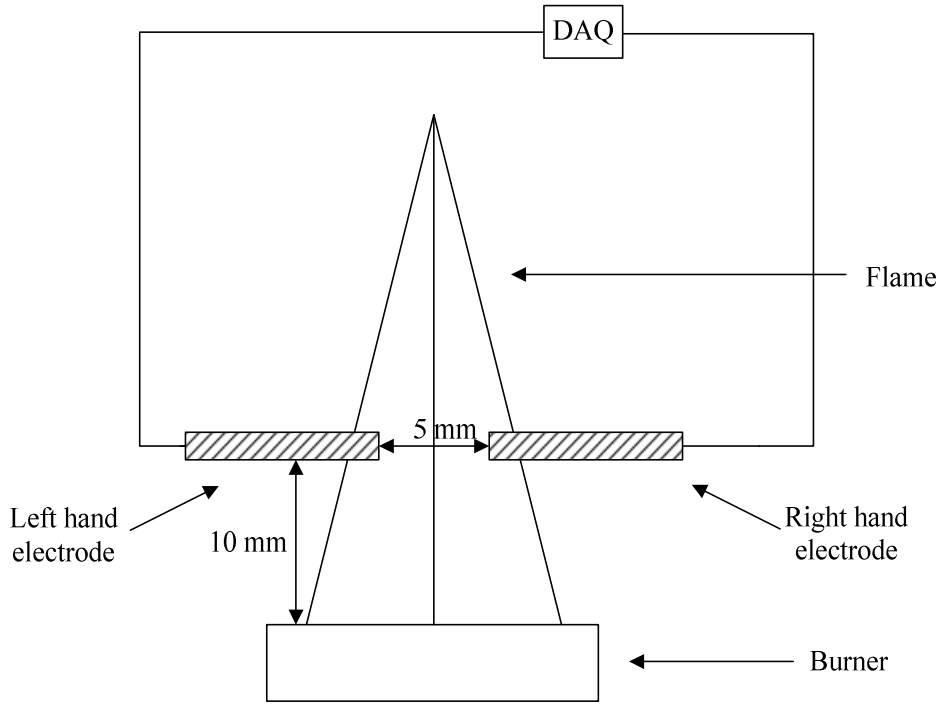

Figure 2-10: Schematic diagram of the electrode arrangement used for the measurement of potential difference

2.5.3 Chronopotentiometry

2.5.3.1 Theory

Chronopotentiometry is a technique where the potential is measured as a function of time at constant current.[66] The experiment is carried out by applying the controlled current between the working and counter electrode with a current source (called a galvanostat) and recording the potential between the working and reference electrodes. Initially as the current is applied, there is a fairly sharp decrease in the potential which is due to the charging of the double layer capacitance until a potential at which O is reduced to R is reached. The potential of the electrode then moves slowly towards a value characteristic of the redox couple determined by the Nernst equation, until eventually the surface concentration of O reaches essentially zero. The flux of O to the electrode surface then becomes insufficient to accept the applied current, and the potential begins to fall sharply until a new electrode process can occur.

2.5.3.2 Procedure/Data acquisition

The electrochemical cell was set-up in a similar fashion as that described for cyclic voltammetry measurements (see Figure 2-7). The WE and RE were placed 5 mm apart from each other in the flame at a height of 10 mm above the burner top. The CE was placed directly above the WE. All electrodes were connected to a potentiostat with a 100 V compliance voltage (Autolab PGStat100, Eco Chemie B.V. supplied by Windsor Scientific Ltd., UK) and voltage measurements were recorded as a function of passed current.

2.6 Characterisation Techniques

2.6.1 Raman Spectroscopy

2.6.1.1 Theory

Raman spectroscopy is a non destructive technique that can be used to study solid, liquid and gaseous samples. The spectroscopic technique utilises an electromagnetic wave, predominately from a laser source of monochromatic light which produces a scattering of light once it encounters a material. The sample absorbs the laser light and after interacting with the sample, the light is re-emitted. Upon interaction between the monochromatic light and the sample, the electron orbits within the molecules are perturbed with the same frequency (ν_o) as the electric field of the electromagnetic wave. An induced dipole moment occurs due to the perturbation or oscillation of the electron cloud leading to separation of charge within the molecules.

The strength of the induced dipole moment, P, is given by equation 2-5:

$$P = \alpha \overline{E} \qquad \textbf{2-5}$$

Where α is the polarisability and $\overline{E}$ is the strength of the electric field of the electromagnetic wave.[68] The polarisability of a material depends on its molecular structure and nature of the bonds.

The majority of the scattered light is emitted at the same frequency ν_o of the laser light, which is known as elastic Rayleigh scattering. However, it is possible that some light is emitted at a different frequency, ν_m and this is known as

inelastic scattering. The frequency of the emitted light is either shifted up or down in comparison with the original monochromatic frequency, ν_o, which is called the Raman effect.

The energy of a photon can be transferred to a Raman-active mode with a frequency, ν_m which results in the frequency of scattered light being reduced to $\nu_o - \nu_m$. This type of Raman frequency is known as Stokes frequency. However, if at the time of interaction between the photon and the material, the Raman active molecule is already in the excited vibrational state, an excessive energy of Raman active mode is released leading to the molecule to return to the basic vibrational state and the resulting frequency of scattered light goes up to $\nu_o + \nu_m$. This type of Raman frequency is known as Anti-Stokes frequency.

The Stokes and Anti-stokes are therefore material sensitive and so Raman spectroscopy will enable the monitoring of processes occurring at the electrode surfaces in the flame, especially the working electrode. These surface processes may include a range of possibilities, including oxidation, electrochemical reduction through the application of a voltage or even contamination from other materials or additives in the flame.

2.6.1.2 Experimental

An argon laser (514.5 nm) attached with a Raman spectrometer RA100 (Renishaw plc, UK) was employed for all Raman investigations. All Raman spectra were referenced against the silicon line at 520.4 cm^{-1}. *Ex situ* experiments were conducted using a 50x/0.75 objective lens, while a fibre optic probe (20x/0.35) was used for *in situ* experiments.

2.6.2 X-Ray Photoelectron Spectroscopy

2.6.2.1 Theory

Photoelectron spectroscopy is a non-destructive surface sensitive technique, which utilises photo-ionisation and analysis of the kinetic energy distribution of the emitted photoelectrons to study the composition and electronic state of the surface of a sample. X-ray Photoelectron Spectroscopy (XPS) uses soft X-rays to examine core electrons. The phenomenon of XPS is based on the photoelectric effect outlined in 1905 by Einstein where he described the concept of a photon being able to eject an electron from a surface when impinged on the surface.[69]

The energy of a photon of all types of electromagnetic radiation is given by the Einstein relation, $E = h\nu$, where E is energy, h is Planck's constant and ν is the frequency of the electromagnetic radiation.

In order to measure kinetic energy of emitted photoelectrons, XPS uses photons of specific energy (monochromatic) from the soft X-ray region. The most typically used X-rays are Al K_α (1486.6 eV) and Mg K_α (1253.6 eV). These photons have limited penetrating power in a solid, of the order of 1-10 μm.

When a sample is irradiated with X-rays, the photons interact with atoms on the surface resulting in total transfer of the photon energy to the electron. This photoelectric effect causes the core electron to be emitted by photoemission, as shown in Figure 2-11.

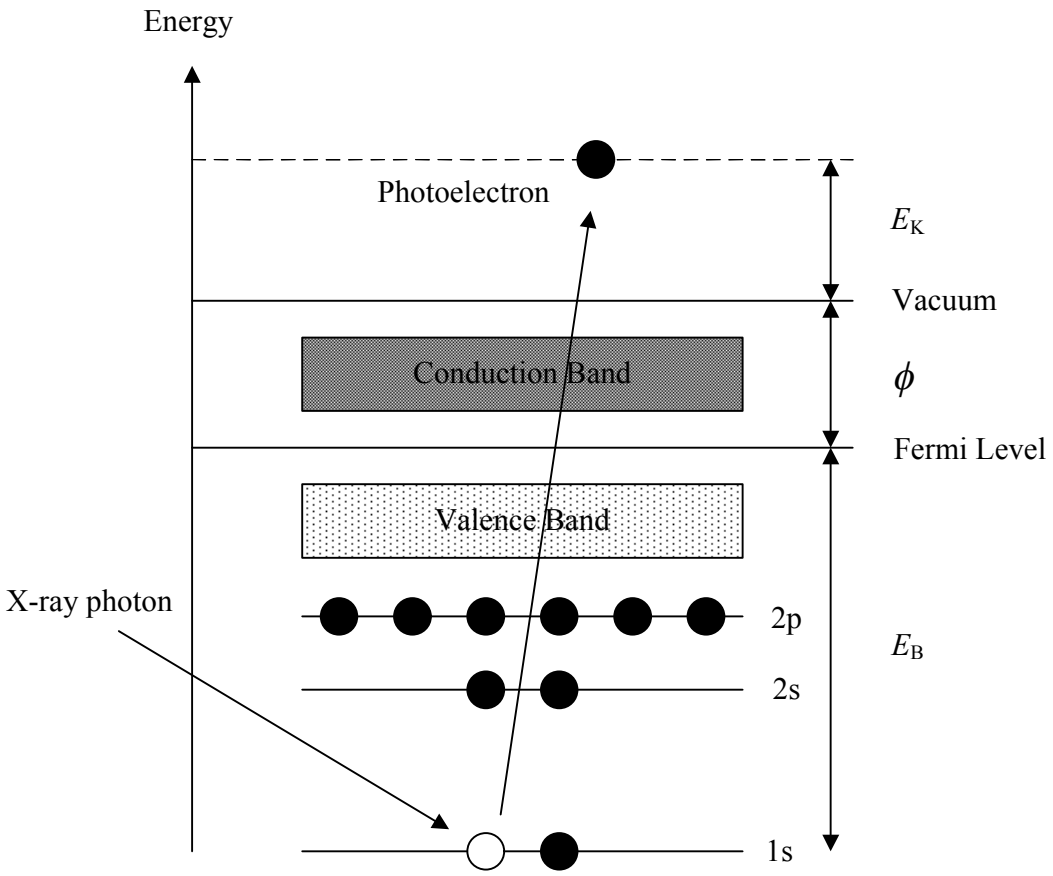

Figure 2-11: Photoemission process of an inner core electron achieved during XPS.

The emitted electron has a specific kinetic energy which can be correlated to its binding energy which is characteristic of each element and thus the photoemission from these orbitals can be used to analyse the composition of the solid material. In addition, for core electrons to be excited, the frequency of the excitation must be greater than the work function of the atom, which is a measure of the energy barrier at the surface for the ejection of an electron into vacuum.[70] Therefore, the relationship between binding energy of a core electron, kinetic energy of an emitted electron and the work function is described by equation 2-6:

$$E_B = h\nu - E_K - \phi \qquad \textbf{2-6}$$

Where E_B is the binding energy of the photoelectron with respect to the Fermi level of the sample, E_K is the kinetic energy of the photoelectron, and ϕ is the work function.

Although XPS is only concerned with emitted electrons that have lost no energy and produce photoemission peaks, some electrons do lose energy (from electron-photon or electron-electron interactions etc) but still escape to the surface and reach the detector. These electrons do not produce a photoemission peak however they do contribute to the background signal.

Koopmans' theory can be used to directly relate the experimental kinetic energies to the binding energies assuming that the energy and spatial distribution of the electrons remaining after photoemission is exactly the same as pre-irradiation.[71] It states that the binding energy is equal to the negative orbital energy of the emitted electron as follows (equation 2-7):

$$E_B = -\varepsilon \qquad \textbf{2-7}$$

where ε represents orbital energy.

However, the E_B is not necessarily equal to the energy of the orbital from which the photoelectron was emitted because reorganisation of the remaining electrons does occur through relaxation. The core hole will have an influence on the final state of the photoemitted electrons but this shift is never more than a few electron volts therefore Koopmans's theorem is commonly used.

Apart from hydrogen and helium (due to their orbital size being so small) all elements can be identified qualitatively via measuring the binding energy of its core electron and comparing with a list of E_B in the literature. Furthermore, the binding energy of a core electron is very sensitive to the chemical environment of that particular element. The binding energy of two identical elements in

different chemical environments of a particular chemical species will lead to change in their binding energy. The variation of binding energy will result in a shift of the corresponding XPS peak, known as a chemical shift. Hence, XPS is a useful characterisation technique for identifying elements and their environment. In addition to this, XPS is also useful in providing quantitative information.

2.6.2.2 Experimental

Measurements were performed using an in-house built XPS instrument at the Chemistry Research Laboratory at the University of Oxford. The measurements were performed under vacuum (~10^{-9} mbar pressure) using monochromatic Al K_α (1486.6 eV) X-ray radiation and the electrons were detected at normal emission. The XPS spectra were fitted using a class of functional forms based on the Gaussian and Lorentzian functions using the XPS fitting programme CasaXPS.

2.6.3 X-ray Diffraction

2.6.3.1 Theory

X-ray diffraction (XRD) is an extremely useful technique for structural characterisation of crystalline solids, which accounts for 95 % of all solid material. Single crystal XRD can be used to elucidate the molecular structure of novel compounds, either natural products or man made molecules. However, powder XRD diffraction is more commonly used for structural characterisation of known materials.[72] In contrast to single crystal XRD where a single crystal is used, in powder XRD the sample may be large crystals or in the form of a powder composed of microcrystals.[73] The underlying principles of both experiments are the same and is based on the constructive interference of

monochromatic X-rays and a crystalline substance (atoms arranged in a regular pattern).[74] These give rise to a diffraction pattern, thus the X-ray diffraction pattern of a pure substance can be considered a fingerprint of that material.

X-rays are generated in a cathode ray tube by heating a filament to produce electrons before being accelerated with aid of applied voltages towards a metal target material (typically copper or molybdenum) containing electrons. When the incoming electrons have sufficient energy to remove inner shell electrons from the target material, characteristic X-rays are produced. The vacant sites are immediately populated by electrons from higher 2*p* or 3*s* orbitals producing K_α and K_β radiation, respectively. The specific wavelengths of the resulting radiation are characteristic of the metal target material. The X-rays are filtered usually by monochromators to produce X-rays of a single wavelength required for diffraction. The K_α and K_β radiation of Cu is 1.5418 Å and 1.392 Å respectively, and are commonly used because these wavelengths are similar in magnitude to the inner atomic distances in a crystal structure.[75]

When X-rays interact with an atom, electrons surrounding the atom begin to oscillate with the same frequency as the incoming X-rays. The interaction will result in a high population of a scattered effect of the combining waves being put out of phase known as destructive interference. However, due to the ordered arrangement of atoms in crystals, constructive interference will happen but only in very few and specific directions causing the waves to be in phase, thus allowing the X-rays to leave the sample at various directions.[75;76]

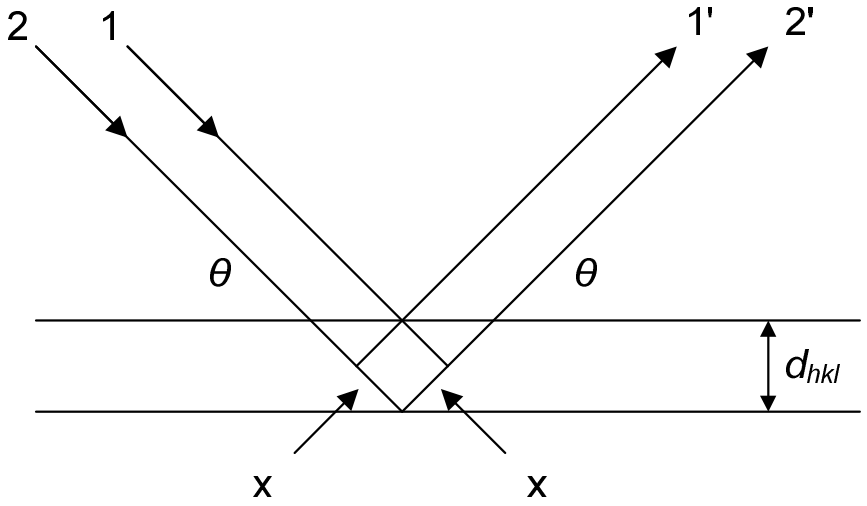

Figure 2-12: Schematic representation of Bragg's Law derived from constructive interference of monochromatic X-ray beam diffracting from parallel planes in the crystal structure.

As mentioned previously, crystals contain atoms which are arranged in a specific order in parallel planes with an interplanar spacing, *d*. The two parallel incident rays (1 and 2) hit the planes at the same angle θ. If the waves are in phase, a reflected beam of maximum intensity will result in waves 1' and 2'. It is therefore given that the path length (2x) between the two beams using trigonometry is $2d\sin\theta$. However, in order for constructive interference to occur between these waves, the path length between 1 to 1' and 2 to 2' must be an integral number of wavelengths, $n\lambda$. This then leads to the Bragg equation (equation 2-8):[76]

$$n\lambda = 2d\sin\theta \qquad \textbf{2-8}$$

Each unit cell is defined by three planes a, b, and c, and three angles α, β, and γ. At the origin of each cell is a lattice point, which must be parallel and equally spaced from another. These lattice points are used to form the Miller indices, and the three dimensions of each plane is identified by three indices, *h, k, l*.[74;77;78] The spacing between adjacent members of the hkl planes is designated d_{hkl}. The

Bragg equation is commonly expressed with respect to these indices as show in equation 2-9:

$$n\lambda = 2d_{hkl}\sin\theta \qquad \textbf{2-9}$$

The above equation can be applied to crystals of any symmetry. For example, a material with cubic symmetry will have the following relationship between d_{hkl}, *a, h, k,* and *l* (equation 2-10):

$$\frac{1}{d_{hkl}} = \left(\frac{h^2 + k^2 + l^2}{a^2}\right)^{\frac{1}{2}} \qquad \textbf{2-10}$$

Substituting this into the Bragg equation (2-11):

$$\sin^2\theta = \frac{\lambda^2}{4a^2}\left(h^2 + k^2 + l^2\right) \qquad \textbf{2-11}$$

This equation will allow one to obtain the unit cell parameters for a cubic structure. Other equations are available to substitute into the Bragg equation to obtain the unit cell parameters of the other six lattice systems.[79]

From measuring the diffraction of the beam from different sections of the electrode material, XRD will be used to determine the composition of the electrode on an atomic level.

2.6.3.2 Experimental

Samples were finely ground using a pestle and mortar to ensure a homogeneous sample was obtained and the crystals were randomly distributed. The sample was then pressed onto a sample holder so that a smooth flat surface was observed

before analysis proceeded. All XRD measurements were collected using a Bruker D4 ENDEAVOR diffractometer with a Cu K_α radiation. The diffractograms were recorded with a 2θ step of 0.05° per second from 5º to 85º.

2.6.4 Thermal Analysis

2.6.4.1 Theory

Thermal analysis comprises a group of techniques in which changes of physical or chemical properties of a substance are measured as a function of temperature and/or time, while the material is subjected to a controlled temperature programme.[80;81] The temperature is controlled by a program whereby the sample is continuously heated or cooled at a constant rate or through a stepwise isothermal method. Several methods are commonly used, however only differential scanning calorimetry (DSC) and thermogravimetric analysis (TGA) methods have been used here.

DSC measures the temperature and heat flow (the flow of energy into or out) associated with transitions in material of a sample (against a reference) as a function of time and temperature. The main advantage of DSC is that samples are very easily encapsulated with very little preparation which allows the measurements to be conducted easily and quickly.[82]

The technique provides qualitative and quantitative information about physical and chemical changes that involve endothermic or exothermic processes or changes in heat capacity using minimal amounts of sample.

Both the sample and reference are maintained at very nearly the same temperature throughout the experiment. The temperature program for a DSC

analysis is designed to allow the temperature of both the sample and reference holders to increase linearly as a function of time. In order for this technique to work, the reference sample should have a well-defined heat capacity (C_P) over the range of temperatures to be used. C_P relates to the amount of heat required to change the temperature of a material by a given amount. As the temperature increases, the sample may undergo a physical transformation such as phase transition. To ensure that both the sample and reference maintain the same temperature during a phase transition, either more or less heat will be required to flow to the sample depending on whether the process is exothermic or endothermic. The phase transition of a solid to a liquid is an endothermic process requiring more heat flowing to the sample to increase the temperature to that of the same rate as reference. In contrast, crystallisation processes, which are an exothermic process, require less heat to raise the sample temperature to that of the reference. These differences in heat flow between the sample and reference allow differential scanning calorimeters to measure the amount of heat absorbed or released during such phase transitions. The actual value of heat flow measured depends upon the effect of the reference and is not absolute. It is important that a stable instrumental response or baseline is produced to which any changes can be measured against.[81-84]

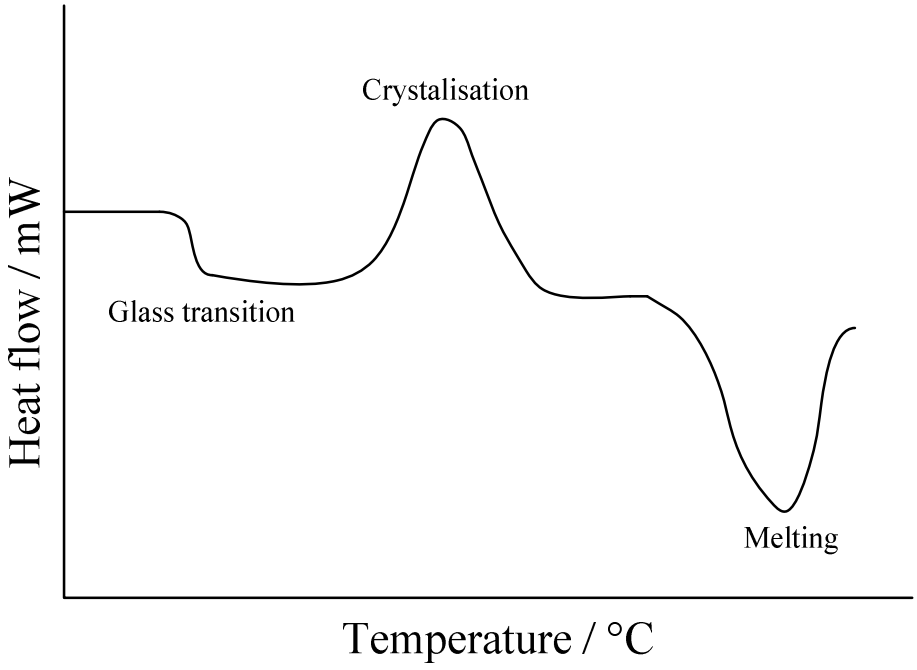

Figure 2-13: A schematic DSC curve demonstrating the appearance of several common features

Figure 2-13 is an example of a DSC experiment which is a curve of heat flow versus temperature or time. By integrating the peaks corresponding to specific transitions, it is possible to calculate enthalpies of transitions by equation 2-12:

$$\Delta H = KA \qquad \textbf{2-12}$$

Where ΔH is the enthalpy of transition, K is the calorimetric constant, and A is the area under the curve. The calorimetric constant will vary from instrument to instrument, and can be determined by analysing a well characterised sample with known enthalpies of transitions.

Thermogravimetric analysis is an experimental technique whereby the mass of a sample is measured as a function of sample temperature or time. As mentioned earlier, a strict temperature program is used. Thermogravimetric measurements can be recorded simultaneously with DTA. The atmosphere used in the TGA plays an important role and can be reactive, oxidising or inert. The resulting

curve from a TGA measurement is usually plotted as mass against temperature or time. Mass changes occur when the sample loses material in one of several different ways including evaporation or decomposition. In contrast, the sample may gain mass through other steps including oxidation.[81-83]

2.6.4.2 Experimental

Both DSC and TGA were performed on selected samples using a Netzsch STA 449C instrument. All samples were made homogeneous by grinding them using a pestle and mortar and approximately 30 mg of sample was placed into alumina crucibles for analysis. The samples were heated in air using a controlled temperature program over the temperature range of 0 to 1590 °C at a rate of 10 °C / min.

2.6.5 Thermal Imaging Pyrometry

2.6.5.1 Theory

Pyrometry is a non-destructive technique that involves intercepting and measuring infrared (thermal) radiation, which is emitted from all materials above 0 K by the motion of atoms and molecules on the surface of objects. Through the use of a pyrometer which incorporates an optical system with a detector, the emitted infrared energy can be related to an output signal, temperature. The output temperature (T) is related to the thermal radiation (W) through the Stefan-Boltzmann law (equation 2-13):

$$W = \varepsilon\sigma T^4 \qquad \textbf{2-13}$$

Where, σ is the constant of proportionality called the Stefan-Boltzmann constant, and ε is the emissivity of the material.

The intensity of the emitted radiation is a function of the temperature of the material, which means, the higher the temperature, the greater the intensity of infrared energy that is emitted.

Emissivity is a term representing a materials' ability to emit thermal radiation. Each material has different emissivity ranging from a theoretical 0 (completely non-emitting) to an equally theoretical 1 (completely emitting). A black body is a theoretical surface, which absorbs and re-radiates all the IR energy it receives. It does not reflect or transmit any IR energy and therefore will have an emissivity equal to 1. With this, the emissivity of a body is defined as the ratio of the radiant energy emitted by the body to the radiation compared to that emitted by a blackbody at the same temperature (equation 2-14):

$$\varepsilon = \frac{W_o}{W_{bb}} \qquad \textbf{2-14}$$

Where, W_o is the total radiant energy emitted by a body at a given temperature, W_{bb} is the total radiant energy emitted by a blackbody at the same temperature.

2.6.5.2 Experimental

A Mikron 9100 series thermal imaging pyrometer (supplied by Mikron Instrument Company Inc., USA) with a temperature range of 800-3000 K was used to determine the surface temperature of materials that were placed in the flame. The associated emissivity factor for each material was selected from the software.

2.7 Cleaning of glassware

All glassware was cleaned thoroughly by placing them into a clean bucket containing a 5% Decon 90 solution made with deionised water until it covered the glassware by 10 cm. The glassware was allowed to soak for at least 2 hours before being rinsed several times with deionised water from Milli-Q Gradient 18.2 MΩ cm (at 25°C) water system, and then left to dry overnight in an oven at 65 °C.

3 Metal/metal oxide wire reference electrodes

3.1 Introduction

Metal wires alone are not typically used as reference electrodes in the liquid phase (except in the case of pseudo reference electrodes) because they possess a single oxidation state. However, by placing a reactive metal wire into a high temperature medium, oxidation and/or ionisation of the metal can occur around the surface of the wire causing the metal to be present in more than one oxidation state.

The metal wire must be readily reactive towards oxygen-containing species in the flame to ensure an oxide layer forms on the surface of the wire. A metal with a high melting point will allow the wire to remain intact once it has been placed into the flame. The calculated adiabatic temperature for the flame was 2200 °C; however the actual flame temperature will be significantly lower (by *ca.* 1000 °C). Therefore, materials with a melting temperature above or around 1200 °C would be ideal candidates for reference electrodes. In addition, to increase the number of ions present around the surface of the electrodes, metals with low ionisation energy would be beneficial. The metals should be able to transfer heat efficiently through the material, and therefore should have high thermal conductivity values.

This chapter begins by describing and discussing a systematic study used to investigate the optimum height of the electrodes to conduct zero current potentiometry experiments, in particular, the effect on voltage stability and noise. Following this, the measured potential difference of five electrochemical cells (each having a different single metal wire) are stated and discussed. The discussion places particular emphasis on the two types of metal/metal oxide electrodes formed - metal wires that once placed in the flame predominantly

form a solid oxide layer on the surface and metal wires that form gaseous oxide sheaths which occur from the sublimation process of the metal oxide that is formed on the surface of the electrode. These latter electrodes are described as 'sacrificial' type electrodes.

3.2 Experimental

A number of metal wires summarised in Table 3-1 were used as electrode material and were chosen based on the criteria described in Section 3.1.

Metal	Purity (%)	Supplier	T_m (K)	IE (kJ/ mol)	WF (eV)	TC (W/ cm K)
W	99.9	Advent	3695	770	4.18 - 5.25	1.740
Mo	99.9	Goodfellow	2896	684	4.36 - 4.95	1.380
Nb	99.9	Advent	2742	652	3.95 - 4.87	0.537
Pt	99.9	Johnson Matthey	2042	868	5.70	0.716
Ti	> 99.6	Goodfellow	1943	659	4.33	0.219

Table 3-1: All metal wires (0.5 mm diameter) were used as single electrodes. The lengths of the wires were 50 mm. A number of properties for the metals are also shown, which were used to decide whether they may be suitable reference electrode candidates.[85] Abbreviations: T_m represents melting temperature, IE represents ionisation energy, WF represents work function, TC represents thermal conductivity at 25 °C

To measure the open circuit potential, the metal wires were individually connected to the positive terminal and a 30 mm length of graphite rod (3 mm diameter, Agar Scientific Ltd) was connected to the negative terminal of a digital storage oscilloscope (Tektronix, DPO 7054) in conjunction with an in-house built buffer amplifier (> 100 MΩ input impedance).

Refer to Chapter 2 for further details regarding experimental procedures.

3.3 Results and Discussion

The term ‘open circuit potential’ (OCP) is used throughout this work and can be described as the steady state potential at which no external current flows to or from the electrodes. The ‘noise’, i.e. voltage fluctuation, was measured through the standard deviation (SD), which was calculated from the mean potential.

3.3.1 Optimisation of electrode height

A series of experiments were conducted to determine the optimum height position of the electrodes in the flame. The experiments investigated the voltage behaviour as a function of height and time. A tungsten (W) wire was placed at three ascending heights (5 mm, 10 mm and 15 mm) above the burner top while a graphite rod was held constant at 10 mm above the burner top. The results are presented below in Figure 3-1.

The W wire electrode fully disintegrated at all three heights before 1000 s, at which point the experiment was stopped. The electrodes disintegrated at different rates, with the electrode held at 5 mm (Figure 3-1a) above the burner top disintegrating the fastest. The surface temperature of the electrode measured at 5 mm was 1585 ± 140 °C. The rate of the electrode disintegration decreased as the height was increased to 10 mm (Figure 3-1b), and decreased further at 15 mm (Figure 3-1c), corresponding to a reduction in the surface temperature of the electrode, 1350 ± 100 °C and 1025 ± 60 °C respectively.

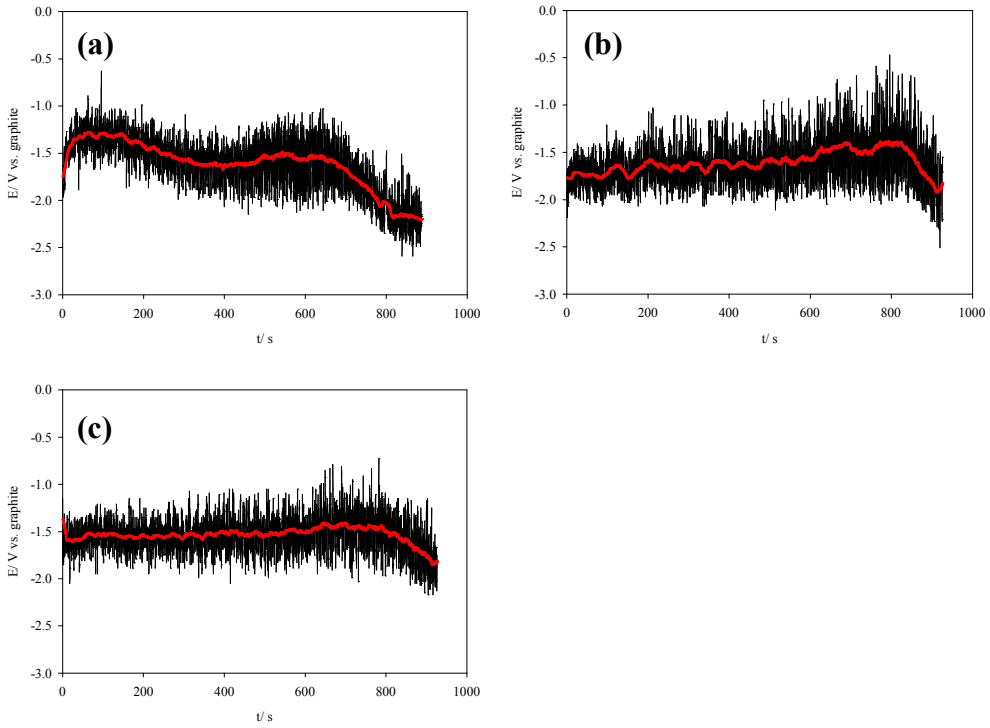

Figure 3-1: Time-based potentiometry experiment for W wire vs. graphite rod in a bare flame (H_2 / O_2: 1.2 / 0.4 $Lmin^{-1}$). The graphite rod was held constant at 10 mm above the burner top. The W wire was held at different heights (a) 5 mm, (b) 10 mm, and (c) 15 mm above the burner top. Raw data is shown in black. Running average with 200 points shown in red (200 points = 20 s).

Although the results presented in Figure 3-1 showed changes in the lifetime of the electrode, it also indicated that the initial potential was unaffected by varying the height. The small changes observed in the initial voltage for all three heights also suggested that the potential was unaffected over a large temperature range (approx. 550 °C), which supports the idea that differences in thermal conductivity values (presented in Table 3-1) between metals did not significantly contribute to the potential difference observed.

The voltage measured was unstable throughout the experiment when the W electrode was held at 5 mm. From 600 s until 890 s, the severity of the unstable voltage was apparent with a drastic voltage drift of 800 mV. The stability of the voltage did increase as the height of the W wire was moved up to 10 mm. A

similar but slightly less drastic voltage drift (710 mV) identical to that observed with the electrode held at 5 mm was seen after 800 s. The most stable voltage was obtained when the electrode was held at 15 mm. A voltage drift was also observed towards the end of the experiment (after 800 s); however it was less drastic than that observed with the electrode held at 5 mm and 10 mm, with the drift being measured at only 420 mV.

The drastic voltage drift that occurred towards the end of every experiment was believed to be due to the disintegration of the wire which occurred in the flame especially at the edge of the flame, as shown in the thermal images of the W wire presented in Figure 3-2.

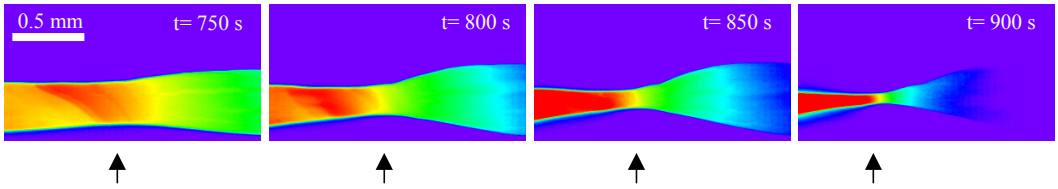

Figure 3-2: Thermal image of the degradation of the W electrode held at 15 mm above the burner top. ↑ indicates the edge of the flame. The wire on the left side of the arrow was in direct contact with the flame whereas the wire on the right side of the arrow was not in contact with the flame.

The thermal images show that the electrode began to dissolve from ca. 800 s and continued for 150 s. which coincided with the drastic voltage drift seen in Figure 3-1c.

The results suggested that 15 mm would be the optimum height to collect voltage readings; however the primary reaction zone is located between 5-10 mm above the burner top. It was decided that a height of 10 mm would be used, and all experiments from here on in were conducted using electrodes held at 10 mm above the burner top.

3.3.2 Potentiometry measurements using exposed metal wires

Tungsten (investigated in Section 3.3.1) and all other wires given in Table 3-1 were analysed using potentiometry. The time based voltage traces of these materials against a graphite rod are presented in Figure 3-3.

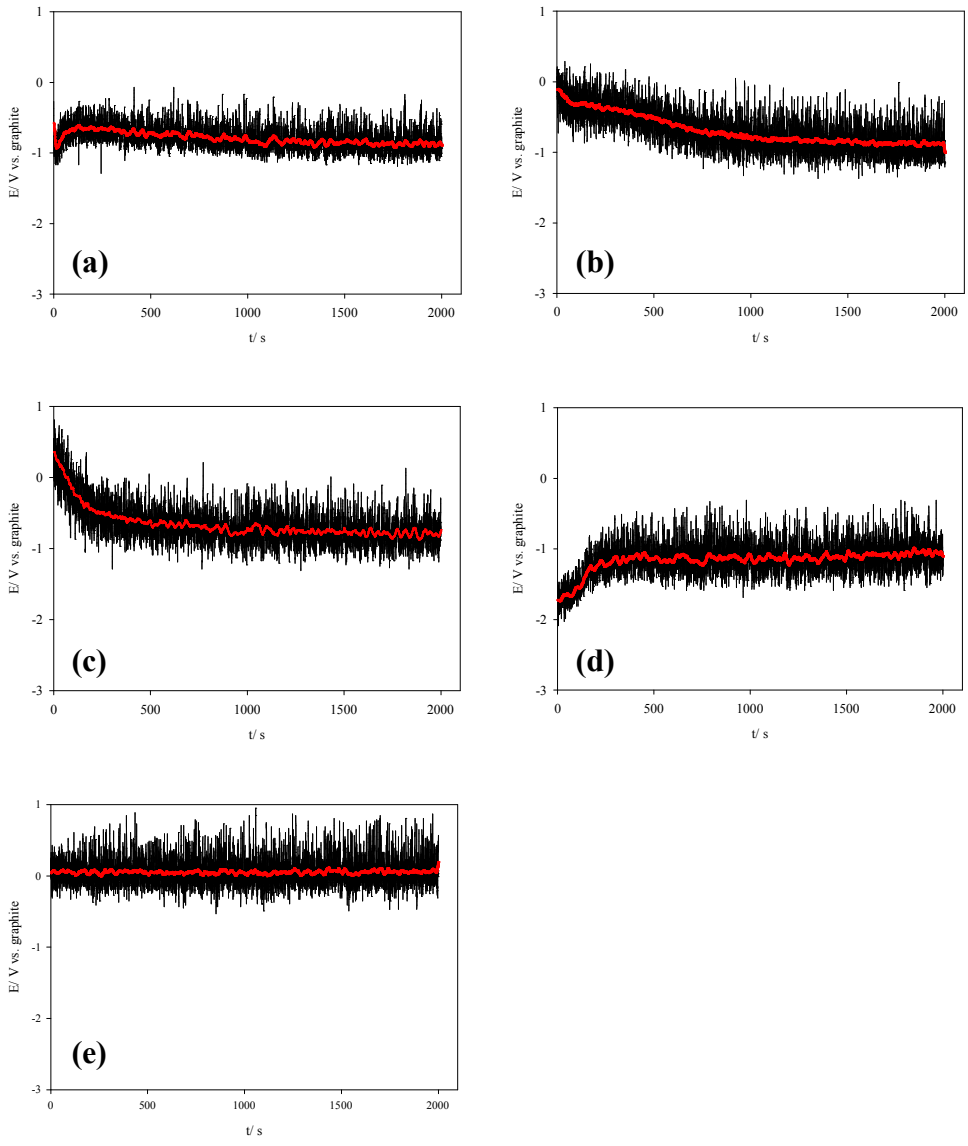

Figure 3-3: Time-based potentiometry experiments for (a) Nb wire, (b) Ti wire, (c) Pt wire, (d) Mo wire, and (e) graphite rod vs. graphite rod in a bare flame (H_2 / O_2: 1.2 / 0.4 $Lmin^{-1}$) held 10 mm above the burner top. Raw data is shown in black. Running average with 200 points shown in red (200 points = 20 s).

A steady stable voltage was attained immediately with W and niobium (Nb) (Figure 3-1b and Figure 3-3a respectively). In contrast, an initial positive or negative voltage drift developed with the remaining three metals. The voltage instability lasted for different times before it became relatively steady. The voltage response with titanium (Ti) wire (Figure 3-3b) became steady after 1000 s. A stable voltage response was observed with platinum (Pt) after 600 s (Figure 3-3c) but Pt is known to be a polarisable material and will not be discussed further in this chapter. The voltage response for molybdenum (Mo) became stable after 500 s (Figure 3-3d). The measured potential difference (E_{cell}) across all five electrochemical cells are summarised in Table 3-2.

Material	E_{cell} **vs. graphite (V)**
Graphite	0.05 ± 0.17
Ti	-0.66 ± 0.18
Nb	-0.79 ± 0.18
Pt	-0.80 ± 0.15
Mo	-1.11 ± 0.20
W	-1.61 ± 0.24

Table 3-2: Average potential difference and noise deviation of metal wire electrodes vs. graphite rod in a bare flame (H_2 / O_2: 1.2 / 0.4 $Lmin^{-1}$). Apart from W, the average potential differences were calculated from 600 s until 2000 s. The potential difference for W was calculated between 0 and 600 s. Each experiment was conducted three times to ensure reproducibility was observed.

The results presented in Table 3-2 indicate that each individual metal contributed to the overall potential difference measured in the flame. This indication was supported when the metal wire was replaced with a graphite rod, which gave an average potential difference value of 0.05 V (Figure 3-3e). The measured potential is thought to have arisen due to a range of processes that occurred on the surface of both the graphite and metal wire electrodes. The graphite electrode was seen to slowly erode over time when placed in the flame (visually illustrated in Section 6.4.1). The surface temperature of the graphite electrode was

measured at 950 ± 50 °C which was significantly lower than its sublimation temperature (3652 °C), suggesting that an etching process had occurred either through atomic hydrogen species etching the surface of the electrode or oxygen species attacking the graphite and producing carbon dioixde.[86-88] The slow erosion process would have contributed towards the potential difference observed but due to the large surface area of the electrode it will have occurred at a steady state in each of the four electrochemical cells. In addition, the reduction reaction (Reaction 3-1) may have occurred at the surface of the graphite electrode.

$$H_3O^+_{(g)} + e^- \rightarrow H_2O_{(g)} + H_{(g)}$$

Reaction 3-1

The steady state environment surrounding the graphite electrode suggests that the processes occurring at the surface of the metal electrode will have been the main contributor(s) towards the potential determining step.

Two types of oxides were identified to either exist surrounding the metal wires, namely a solid oxide layer or a gaseous oxide sheath. The formation of the oxide around the metal wire in conjunction with the thermal conditioning of the electrodes is likely to have caused the initial slope observed with many of the metals.

A solid oxide layer develops around the surface of the Ti and Nb metal wires (Figure 3-4) because the oxides do not sublime nor evaporate at the temperatures generated by the flame.

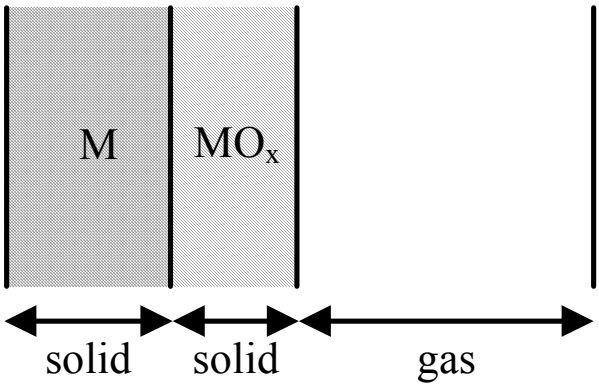

Figure 3-4: Schematic showing the formation of the oxide layer that develops around the metal wire once it is placed in a flame.

The solid oxide may have formed through the ionisation of the metal followed by oxidation, but a direct oxidation process is more likely to have taken place. The entrainment of molecular oxygen from the surrounding air will have provided oxygen containing species, such as OH^-, $OH\bullet$ and O^{2-}, amongst others which would have readily reacted with the metal (M) and/or ion (M^+) to form the metal oxide layer (MO_x) on the surface of the electrode. The oxide layer may have grown or been sustained by the thermally-activated, highly mobile movement of O^{2-} species within the bulk of the material through Reaction 3-2.[89]

The proposed oxidation reaction occurring at the surface of the metal wire electrode was thought to be the following:

$$M_{(s)} + \tfrac{x}{2} O^{2-}{}_{(s)} = MO_{\tfrac{x}{2}(s)} + xe^-$$

Reaction 3-2

The Nernst equation for Reaction 3-2 is given in equation 3-1 to assess the contribution of this reaction towards E_{M/MO_x}, where M represents Ti or Nb. Where E^O is defined as the standard electrode potential, R represents gas

constant, T is temperature, n is the number of electrons transferred in the cell reaction (if it was allowed to proceed), F is the Faraday constant, which represents the charge on 1 mole of electrons and a is the activity of species.

$$E_{\mathrm{M/MO_x}} = E^O + \frac{RT}{nF}\ln\frac{a_{\mathrm{MO_{x/2}}}}{a_{\mathrm{M}} \cdot a^{x/2}_{\mathrm{O^{2-}}}} \qquad \textbf{3-1}$$

Since the metal and metal oxide are present in the solid state, the activity ratio of these species will be unity. The $E_{\mathrm{M/MO_x}}$ will therefore be dependent upon the $\mathrm{O^{2-}}$ ion concentration and E^O value, defined as the standard electrode potential.

The E^O value was calculated using equation 3-2:

$$\Delta G^0 = -nFE^O \qquad \textbf{3-2}$$

Where ΔG^O is Gibbs energy of a cell reaction. ΔG^O can be calculated using equation 3-3, where ΔH^O is change in enthalpy of the system, ΔS^O is change in entropy in system.

$$\Delta G^O = \Delta H^O - T\Delta S^O \qquad \textbf{3-3}$$

The E^O values have been calculated for the oxidation reaction of Ti and Nb using $\mathrm{O^{2-}}$ species. Due to the absence of thermodynamic data for $\mathrm{O^{2-}}$ in the solid state, thermodynamic data for $\mathrm{O^{2-}}$ in the gas phase was obtained and used from ThermoVader program.

$$\mathrm{Ti} + 2\mathrm{O^{2-}} = \mathrm{TiO_2} + 4e^- \qquad E^O = 1.95\ \mathrm{V}$$

Reaction 3-3

$$2\mathrm{Nb} + 5\mathrm{O}^{2-} = \mathrm{Nb_2O_5} + 10e^- \qquad E^O = 1.45 \text{ V}$$

Reaction 3-4

As mentioned earlier, the Nernst equation has demonstrated that $E_{\mathrm{M/MO_x}}$ will be equal to E^O, thus $E_{\mathrm{Ti/TiO_e}}$ (Reaction 3-3) and $E_{\mathrm{Nb/Nb_2O_5}}$ (Reaction 3-4) should be 1.95 V and 1.45 V respectively. The $E_{\mathrm{M/MO_x}}$ values for these materials follow the same trend seen with E_{cell} values for Ti and Nb, with Ti being more positive (Table 3-2). However, a discrepancy does occur between the two sets of data. The difference in voltage between E_{cell} for Ti and Nb vs. graphite was 130 mV compared to a difference of 500 mV calculated above for $E_{\mathrm{Ti/TiO_e}}$ and $E_{\mathrm{Nb/Nb_2O_5}}$. The discrepancy suggests that E_{cell} was likely to be due to a mixed potential, dominated by oxidation reaction(s) and other surface reaction(s). There is evidence to suggest that a possible potential determining step in plasma systems is the rate of oxygen diffusion through the material. Rohnke *et al.* found that the surface exchange rate for a sample in oxygen-containing plasma was significantly higher than that in a molecular oxygen environment.[90] The possible surface reactions will be discussed further in this chapter.

Other oxygen species present in the flame at high concentrations such as $\mathrm{OH^-}$ and $\mathrm{OH}\bullet$ may contribute towards the oxidation of these metals through Reaction 3-5 and Reaction 3-6. If this is the case, E^0 would be:

$$\mathrm{Ti} + 2\mathrm{OH^-} = \mathrm{TiO_2} + 2\mathrm{H}\bullet + 2e^- \qquad E^O = 1.04 \text{ V}$$

Reaction 3-5

$$2\mathrm{Nb} + 5\mathrm{OH^-} = \mathrm{Nb_2O_5} + 5\mathrm{H}\bullet + 5e^- \qquad E^O = 0.10 \text{ V}$$

Reaction 3-6

The Nernst equation applied to the above reaction is shown below in equation 3-4.

$$E_{M/MO_x} = E^O + \frac{RT}{nF} \ln \frac{a_{MO_x} \cdot P_{H\bullet}{}^x}{a_M \cdot P_{OH^-}{}^x} \quad \textbf{3-4}$$

Equation 3-4 suggests that E_{M/MO_x} will be not only be dependent upon E^O but also the partial pressure of the gaseous species, $P_{H\bullet}$ and P_{OH^-}. To accurately calculate E_{M/MO_x} both $P_{H\bullet}$ and P_{OH^-} would need to be measured. There have been reports which have demonstrated that these flame species can be measured in a flame medium using a mass spectrometer.

Oxides such as WO_3 and MoO_3 sublime at relatively low temperatures (ca. 750 °C and 1155 °C respectively)[85] producing a gaseous sheath (Figure 3-5). The term 'sacrificial' is usually given to these types of electrodes because a fresh layer of metal is always exposed at the surface.

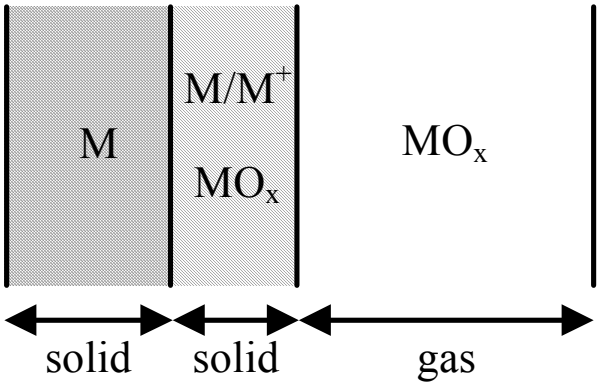

Figure 3-5: Schematic showing the formation and sublimation of an oxide which produces the gaseous sheath that develops in the immediate vicinity of the 'sacrificial' metal wire (Mo and W) once placed in a flame.

The sublimation process for WO_3 and MoO_3 is further supported by the increase in the noise of the voltage (shown by the standard deviation in Table

3-2) compared to the other metal wire electrodes which have noise values similar to graphite vs. graphite. This supports the argument that a solid oxide layer forms around the Ti and Nb wires and no sublimation occurs. The origin of the noise for Ti and Nb was probably due to the flame edge effects (surrounding the graphite electrode) where oxygen concentration was high due to air entrainment.

The proposed oxidation reaction occurring at the surface of W and Mo wires is similar to Reaction 3-2, however the reacting species was thought to be predominantly OH^- which formed the metal oxide to be present in the gaseous phase (Reaction 3-7).

$$M_{(s)} + xOH^-_{(g)} = MO_{x\,(s)} + xH\bullet_{(g)} + xe^-$$

Reaction 3-7

Although the free radical(s) formed are known to be stable at high temperature, they may further react with similar species to produce excited molecules or compounds such as $H_2{}^*$ or H_2O^*.

Equation 3-5 was used to assess the contribution of Reaction 3-7 towards E_{M/MO_x}, where M represents W or Mo.

$$E_{M/MO_x} = E^O + \frac{RT}{nF}\ln\frac{P_{MO_x}\cdot P_{H\bullet}{}^x}{a_M \cdot P_{OH^-}{}^x} \qquad \textbf{3-5}$$

The E^O values have been calculated for the oxidation reaction of W (Reaction 3-8) and Mo (Reaction 3-9) using OH^- species:

$$W + 3OH^- = WO_3 + 3H\bullet + 3e^- \qquad E^O = -2.51\ V$$

Reaction 3-8

$$Mo + 3OH^- = MoO_3 + 3H\bullet + 3e^- \qquad E^O = -2.36 \text{ V}$$

Reaction 3-9

The E^O values alone cannot be used to calculate E_{M/MO_x} for W and Mo because the relative partial pressures of P_{MO_x}, $P_{H\bullet}$ and P_{OH^-} must be taken into consideration. The E^O values do however follow the same trend observed with that of the E_{cell} values for W and Mo vs. graphite, with W being more negative (Table 3-2). Similar to Ti and Nb, there is a difference between the E_{cell} and E^O values. The difference between the E_{cell} for W and Mo was 500 mV compared to a difference of 150 mV calculated above for E_{W/WO_3} and E_{Mo/MoO_3}. The discrepancy again suggests that other individual or combined chemical processes contributed to the measurement of E_{cell}. It is however unlikely that O^{2-} species participated in the oxidation process.

The possible ionisation of all the metals has been considered as potential determining steps. The ionisation process is only likely to occur with W and Mo since a fresh metal surface is always exposed and they also both possess low ionisation energies. In contrast, the surface of both Ti and Nb metal wires were covered by their oxides preventing ionisation from occurring. As mentioned above, it is very unlikely that ions formed in the flame will remain unchanged close to the electrode, but they are more likely to react with other flame species. The E^O values for the ionisation reaction of the metal wires have been calculated but as expected they were not close or correlated to their respective E_{cell} values, suggesting that the ionisation process was not the potential determining steps but may contribute to the overall E_{cell} value. The formation of ions from the surface of the electrode would give rise to a concentration gradient where W^+ and Mo^+ ions will move from a high concentration to a low concentration. This additional process is termed the diffusion potential and can be described by the Henderson equation. Diffusion potential in flames has

already been described and is relatively large in magnitude because it is derived from the difference in mobility between the electrons and cations present in a flame.[1;34]

Figure 3-6 illustrates (on a potential scale) the likely reactions that are thought to contribute most significantly towards the E_{cell} value for the four electrochemical cells.

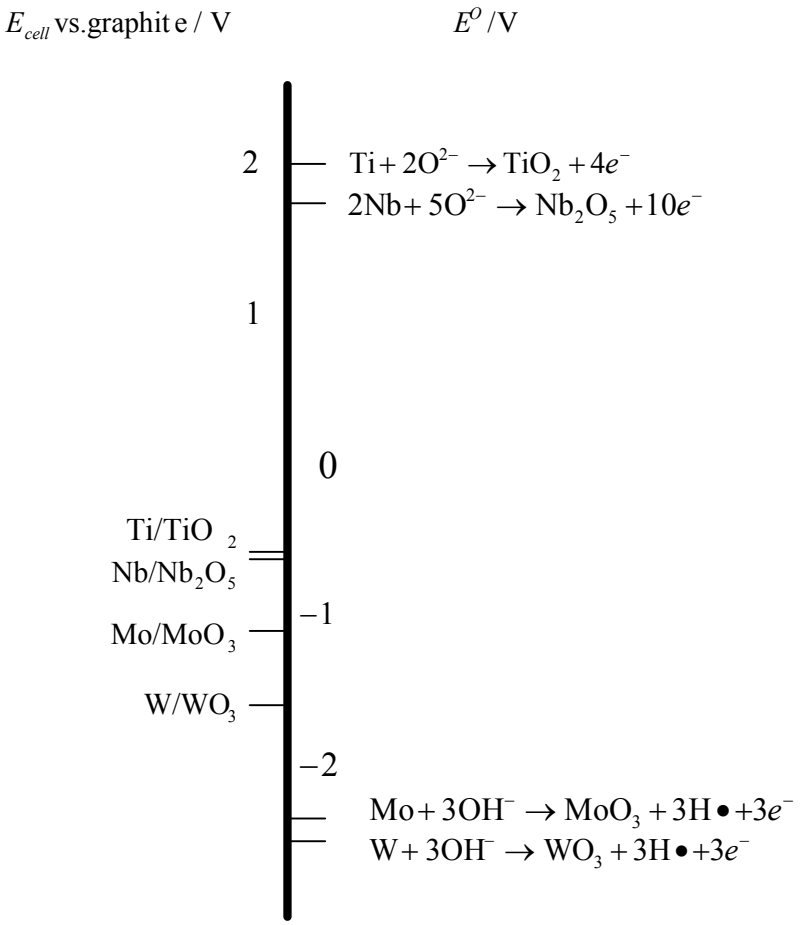

Figure 3-6: Potential difference of metal wires and subsequent standard electrode potential of proposed oxidation reaction of the metal shown on a potential scale (not drawn to scale.)

Surface processes that may have contributed towards the E_{cell} include thermionic emission and the reverse process, electron attachment to the solid electrode. The relationship between these two processes is shown in Reaction 3-10

$$e^{-}_{(el)} = e^{-}_{(g)}$$

Reaction 3-10

Thermionic emission describes the energy obtained (thermal) by a metal to overcome its work function to promote an electron from the metal to the gas phase. The current density due to the thermal emission of electrons from the electrodes can be obtained from the Richardson-Dushman equation which describes the current density to both the surface electrode temperature and work function of the metal. The work function of the metals (presented in Table 3-1) are comparable; however, it has already been discussed that a solid oxide layer exists around the Ti and Nb wires and for this reason their oxide work function must be taken into consideration. The work function of both TiO_2 (rutile) and Nb_2O_5 (6.79 and 5.65 respectively)[91;92] are higher than W and Mo. The difference in work functions coupled with different electrode surface temperatures would suggest that the degree of thermionic emission occurring would be different at each solid-gas interface. All these measurements were taken at zero current and therefore the reverse process of thermionic emission (electron attachment) must have occurred to preserve charge neutrality.

Other effects that may contribute to the overall potential difference include Soret thermal diffusion and Seebeck potentials. However, because the magnitude of the potentials that were measured were large, it is unlikely that the magnitude of these contributions would be significant.

3.4 Summary

It has systematically been shown that the optimum height of the electrodes to conduct zero current potentiometry experiments should be 10 mm above the

burner top. This height will enable the primary reaction zone to be explored in conjunction with good voltage stability and metal wire electrode time life.

The potential difference of five electrochemical cells (each containing a different single metal wire) has been measured, and to which the values have been shown to be unique towards the individual metal wires.
Two types of metal/metal oxide electrodes were identified to exist once the metal wires were placed into the flame, namely metal wires with a solid oxide layer or metal wires surrounded by a gaseous oxide sheath (termed 'sacrificial' type electrodes).

The potential determining step is likely to have been a mixed potential dominated by oxidation reactions in conjunction with other surface reactions.

The next chapter shall continue investigating metal wires that form sacrificial type electrodes in the flame. A method will be proposed to reduce the noise and increase the voltage stability during measurements without interfering with the gaseous sheath formation.

4 The Dynamic reference electrode

4.1 Introduction

The previous chapter demonstrated a potential difference can be measured using bare metal wires as electrodes in a conducting flame medium. However, the issue of voltage stability during open circuit potential experiments was highlighted. The experiments conducted using molybdenum (Mo) and tungsten (W) wires as electrodes are examples whereby the initial stability and stability over the course of the experiments have been brought to the forefront (Figure 4-1).

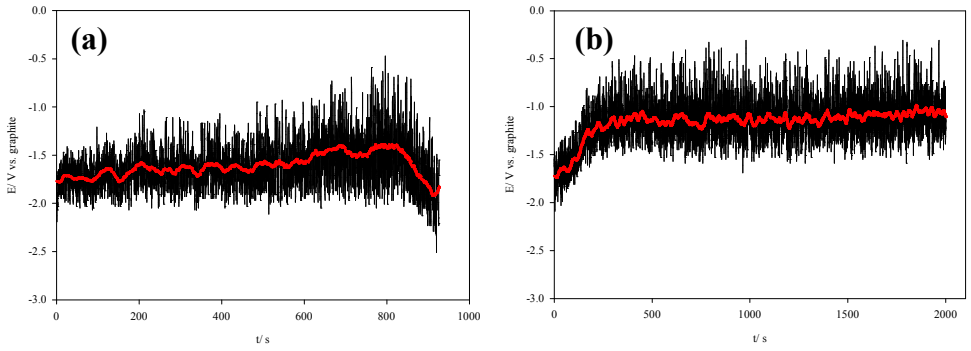

Figure 4-1: Time-based potentiometry experiment for (a) W wire vs. graphite rod and (b) Mo wire vs. graphite rod in a bare flame (H_2 / O_2: 1.2 / 0.4 $Lmin^{-1}$). Raw data is shown in black. Running average with 200 points shown in red (200 points = 20 s).

A dynamic reference electrode, similar to the dynamic hydrogen electrode (DHE) used in the liquid phase,[93;94] was designed and created for use in the gas phase. The DHE simulates a reversible hydrogen electrode by containing two internal electrodes, at least one of which is a platinum (Pt) electrode. A small constant current is enforced between the two electrodes, with Pt being biased negative resulting in a small amount of hydrogen evolution. The potential of the

DHE contains a slight overvoltage caused by the reaction; however it is hardly affected by the environment. The aim of the dynamic electrode was to suppress the sublimation process of the oxide from the surface of the reference wire electrode. The potential difference for both Mo and W wires (shown above) was measured at -1.11 ± 0.20 V and -1.61 ± 0.24 V, respectively. The noise level for these two materials will be used as a baseline to indicate whether the dynamic electrode can be used to reduce the noise.

4.2 Experimental

4.2.1 Materials

Both reference wires, W and Mo (0.5 mm diameter), were purchased from Advent Research Materials Ltd., whereas the Pt wire (0.5 mm diameter) was supplied by Johnson Matthey Ltd. The graphite rods (3 mm diameter) and a twin bore ceramic tube (1.2 mm inner diameter per bore, 4 mm outer diameter) were purchased from Agar Scientific Ltd and Analytical Technology International Ltd., respectively. For each material, the highest purity available was obtained.

4.2.2 Electrode design

The dynamic electrode constituted of two parts – 'front' and 'back'. The 'front', which was placed in the flame, consisted of a 3 mm diameter coil made with a Pt wire which was placed in a single bore hole and extended through the entire length of the ceramic tube. The reference wire was positioned through the second bore hole allowing the tip of the wire to be positioned inside the Pt coil as shown in Figure 4-2. A coil was chosen to apply an electric field around the metal wire

and to reduce the surface temperature of the reference wire in the flame (reduce the rate of material evaporation).

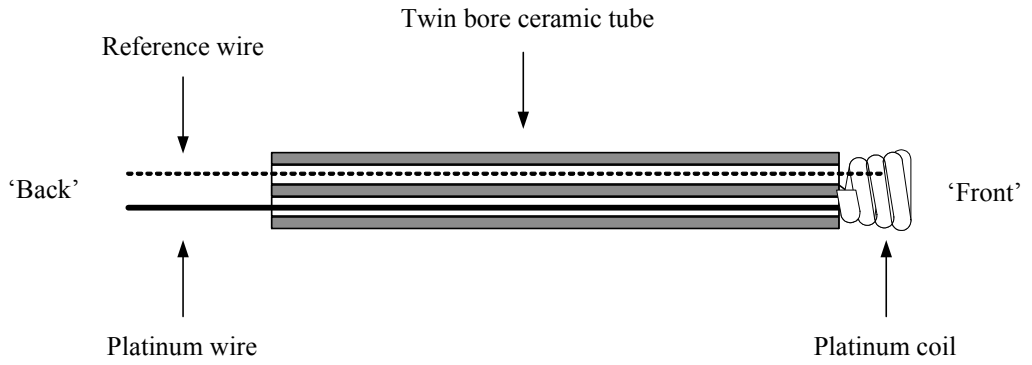

Figure 4-2: A 600 mm length twin bore ceramic tube that allowed the reference wire tip (1.5 - 2 mm length) to be placed within the 3 mm length Pt coil. The potentiometer was connected to the wires at the 'back' of the tube.

All electrical connections were made at the 'back' of the electrode. The potentiometer together with a 9 V battery (power source) was connected to both the reference and Pt wires to complete the internal circuit. A potentiometer can be described as a three terminal variable resistor. When two terminals are used (one side and the wiper), the potentiometer behaves as a variable resistor, whereas, when all three terminals are used, it behaves as an adjustable voltage reducer.

Depending on whether a variable resistor or a voltage reducer was required, the terminals were manipulated to achieve the desired effect as shown in Figure 4-3. Both settings of the potentiometer (voltage reducer or variable resistor) will be used to investigate whether the stability of the reference electrode voltage can be enhanced.

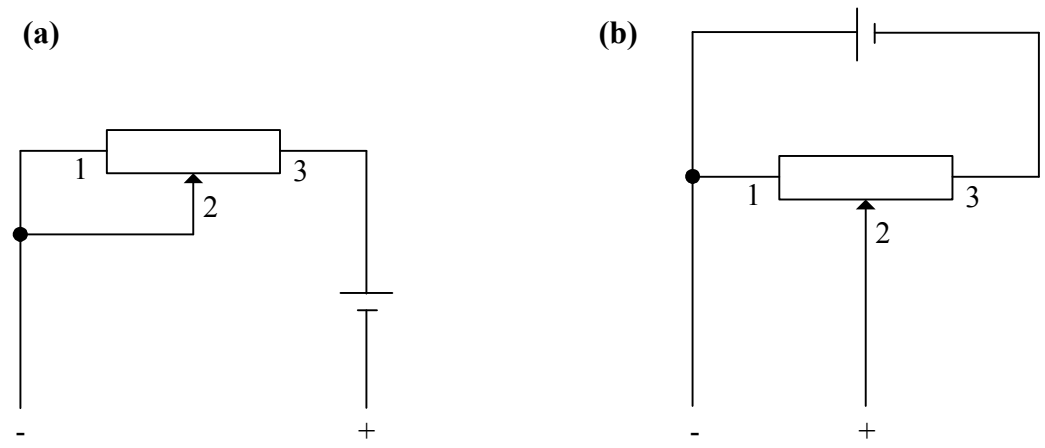

Figure 4-3: Electrical circuit of a potentiometer connected to a 9 V battery used to complete the internal circuit between the reference and Pt wires (a) Variable resistor (b) Voltage reducer.

To measure the potential difference, an external circuit was made by connecting both the reference wire (negative terminal) and graphite rod (positive terminal) to a digital storage oscilloscope (Tektronix, DPO 7054) in conjunction with an in house built buffer amplifier (> 100 MΩ).

Refer to Chapter 2 for further details regarding experimental procedures.

4.3 Results and Discussion

In this text, a 'potential difference' will refer to the voltage measured between a reference wire electrode and a graphite rod electrode, whereas the term 'applied voltage' indicates the voltage that is applied between the reference and Pt wires. Refer to Section 3.3 for the definition of 'OCP' and 'noise'.

4.3.1 Constant voltage and variable current potentiometry

With a constant voltage supplied (9 V), the W wire was biased both positive and negative with respect to the Pt coil. When the wire was biased negative and negligible amounts of current passed through the circuit (0 - 300 s), the average potential difference was -10.81 ± 0.67 V (Figure 4-4). The potential difference is a contribution of the -9 V applied voltage and the OCP. The noise significantly increased compared to the open circuit potential of an exposed W wire electrode as shown in Figure 4-1b, suggesting that the applied 9 V was significantly contributing towards the noise observed. The effect of applied voltage on the external circuit will be discussed in Section 4.3.2. Between 350 and 650 s, the current passed through the circuit was increased to the maximum and the average potential difference was -11.07 ± 0.87 V. The increase in the current did not affect the voltage but did cause the noise to rise by 20 mV. It was thought the current passed through the electrode caused an excess of charge to build upon the electrode. The evaporation of oxide particles from the surface of the electrode may have helped to relieve the excess charge on the electrode. Similar results were obtained when the terminal of the electrodes were reversed, whereby the W wire was biased positive with respect to the Pt coil. The same trend was observed when W wire was replaced with a Mo wire.

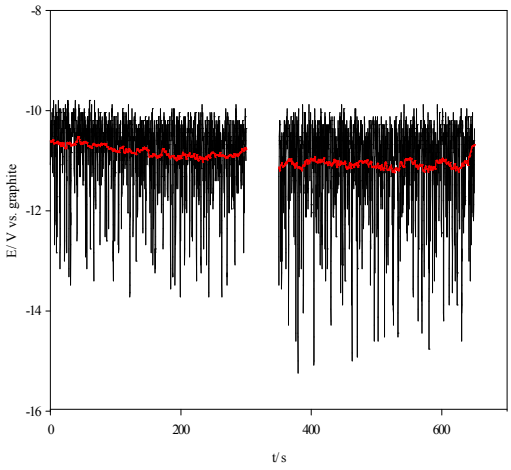

Figure 4-4: Time-based potentiometry experiment for the dynamic electrode vs. graphite rod in a bare flame (H_2 / O_2: 1.2 / 0.4 $Lmin^{-1}$). The W wire was polarised negative (constant 9 V) with respect to Pt coil. Refer to Figure 4-1 caption for details regarding data representation.

It has previously been shown in Section 3.3.1 that the voltage from using an exposed W wire electrode was only stable for 800 s before a drastic voltage shift occurred. Through the use of the Pt coil acting as a shield, the life time and stability of the reference wire was increased to a minimum time of 2000 s. The use of the variable resistor did not serve to reduce the noise associated with the voltage response. It was therefore decided to concentrate on using the voltage reducer.

4.3.2 Constant current and variable voltage potentiometry measurements

Both W and Mo wires were individually biased negative and positive with respect to the Pt coil. The results of the W wire biased negative and positive with respect to the Pt coil are shown in Figure 4-5.

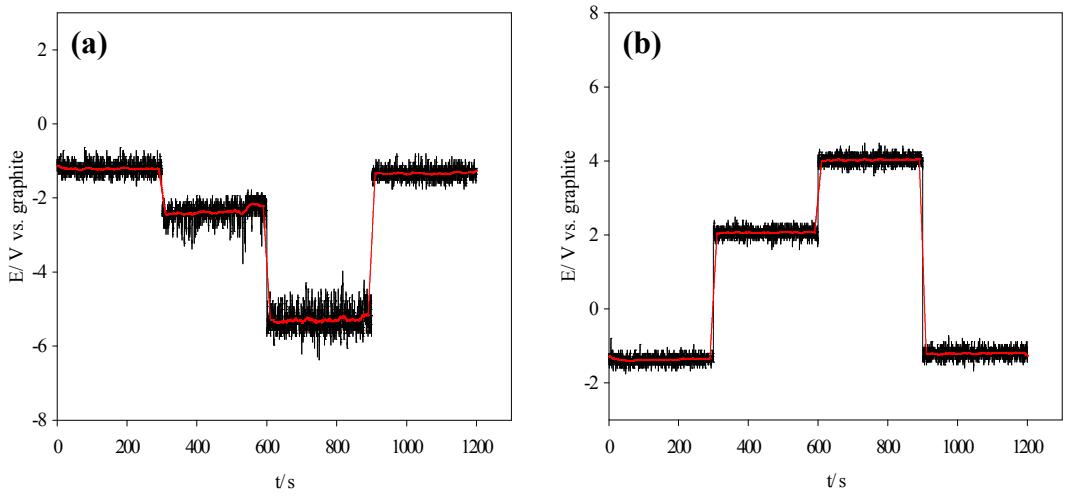

Figure 4-5: Time-based potentiometry experiment using the dynamic electrode vs. graphite rod in a bare flame (H_2 / O_2: 1.2 / 0.4 $Lmin^{-1}$). (a) W wire polarised negative with respect to the Pt coil. (b) W wire polarised positive with respect to the Pt coil. Refer to Figure 4-1 caption for details regarding data representation.

Between 0 and 300 s, 0 V was applied and the average potential difference for the W wire biased negative and positive with respect to the Pt coil was -1.21 ± 0.14 V (Figure 4-5a) and -1.34 ± 0.11 V (Figure 4-5b), respectively. The voltages are very much comparable to those observed for the OCP for an exposed W wire as shown in Figure 4-1a. However, using the dynamic electrode arrangement with 0 V applied, the noise was reduced by ± 0.10 V and ± 0.13 V respectively. The measured temperature of the W wire surrounded by the coil was 300 ± 50 °C, significantly lower than that observed by the exposed wire (measured as 1350 ± 100 °C in Chapter 3). The lower surface temperature resulted in slower evaporation rate of WO_x, thus a reduction in the noise.

During 300 – 600s, 1 V was applied to the W wire being biased negative with respect to the Pt coil (Figure 4-5a). The average potential difference became more negative to -2.12 V; however, the noise increased to ± 0.25 V. The voltage applied was further increased by an additional 3.5 V during 600 and 900 s. This resulted in the potential difference becoming more negative and the noise increasing (-5.48 ± 0.28 V). It was also shown that by decreasing the applied

voltage, the noise could also be reduced. The voltage applied was decreased to 0 V between 900 and 1200 s which resulted potential difference becoming more positive and a reduction in the noise (-1.33 ± 0.14 V).

When the W wire was biased positive, the applied 3.5 V caused the potential difference to become 2.06 ± 0.11 V. When the applied voltage was further increased by an additional 2 V, the potential difference rose to 4.02 ± 0.12 V. The increase in the applied voltage did not serve to increase or decrease the noise. The voltage applied was reduced back to 0 V which resulted in the average potential difference going to -1.25 ± 0.11 V. No change with the noise was observed, confirming that the noise reduction using the dynamic set-up was mainly due to the shielding effect of the Pt coil which reduced the temperature of the reference wire.

Tungsten wire was replaced with a Mo wire and similar experiments were conducted. In Figure 4-6, the Mo wire was biased positive with respect to the Pt coil.

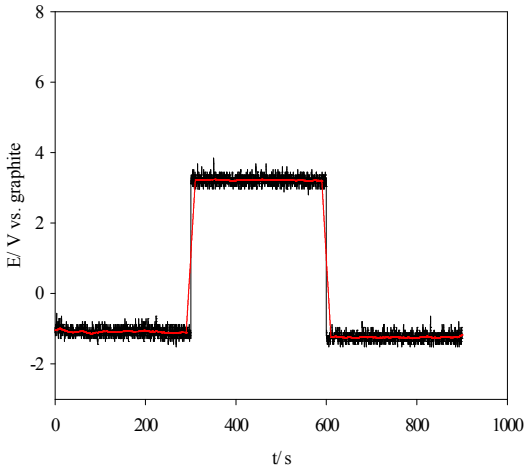

Figure 4-6: Time-based potentiometry experiment for the dynamic electrode vs. graphite rod in a bare flame (H_2 / O_2: 1.2 / 0.4 $Lmin^{-1}$). The Mo wire polarised positive with respect to Pt coil. Refer to Figure 4-1 caption for details regarding data representation.

When 0 V was applied between 0 and 300 s, the average potential difference was -1.13 ± 0.12 V. The voltage was comparable to that observed for the OCP of an exposed Mo wire shown in Figure 4-1b. However, the dynamic electrode arrangement with 0 V applied reduced the noise from ± 0.17 to ± 0.12 V. The reason for the noise reduction is similar to that explained for W wire. The Pt coil aided in the reduction of the Mo wire surface temperature, which in turn reduced the evaporation process of MoO_x from the surface of the wire. During 300 – 600 s, the applied voltage was increased to 4.5 V which caused a rise in the potential difference - 3.21 ± 0.11 V. As expected, the increase in the applied voltage did not serve to increase or decrease the noise. The voltage applied was reduced back to 0 V which resulted in the average potential difference reducing to -1.25 ± 0.11 V. When the applied voltage was negative for the Mo wire with respect to the Pt coil, the response was similar to that observed with the W wire biased negative.

When the reference wires were biased negative with respect to the Pt coil, the applied voltage caused the noise to increase. It was likely that the negative voltage applied to the reference wire served to move the equilibrium potential more negative which caused the metal oxide formed to be reduced to the metal. For example, the proposed reaction that took place on the surface of the W wire is the following (Reaction 4-1):

$$WO_3 + 6H_3O^+ + 6e^- \rightarrow W + 9H_2O$$

Reaction 4-1

The loosely bound W metal particles formed on the surface of the wire instantaneously become re-oxidised (due to the high temperature and oxygen-containing flame) to form loosely bound WO_3 particles. The oxide particles can easily be agitated by the flame causing particles to leave the surface, hence an increase in the noise (Figure 4-7).

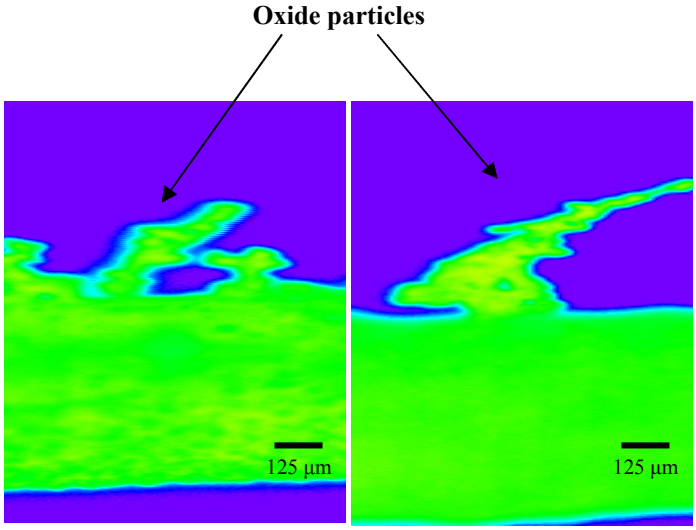

Figure 4-7: Thermal images taken of W wire placed in the Pt coil (biased negative with respect to the Pt coil).

The increase in applied voltage may have served to increase the production of oxide particles, which was reflected in the noise levels which rose (Figure 4-5a). When the voltage applied to the W wire biased negative with respect to the Pt coil was increased, the noise level became similar to that of an exposed W wire electrode nearing rapid evaporation as shown in Figure 4-1a after 800 s.

In contrast, when the W wire was biased positive, the rate of metal oxidation could not be further increased by applying a voltage because the thermal oxidation process was more dominant. This may have caused the oxide particles to not have been loosely bound and therefore disintegrate and evaporate at a much slower rate. The subsequent result is no change in the noise when the positive voltage is increased. The same rationale can be applied to the Mo wire results.

To add support to this theory, a similar experiment should be devised in a hydrogen rich (reducing) flame. With the reference wire biased positive with respect to the Pt coil, the voltage applied would be expected to increase the noise, however no change in the noise should be seen when the reference wire is biased negative and voltage applied.

The effect of reducing the length of the Pt coil was investigated. The length was reduced from 3 mm to 1.5 mm. The W wire was biased positive with respect to the Pt coil. The resulting time based voltage trace is shown in Figure 4-8. The noise recorded was ± 0.18 V, which was an increase in noise compared to the 3 mm length Pt coil used in Figure 4-5b. This supports the idea of the Pt coil acting as a shield and preventing the W wire from the extreme heat of the flame and in turn, reducing the rate of evaporation. The use of a 1.5 mm length Pt coil decreases the shielding area and therefore causes a rise in the rate of evaporation. As expected, the application of voltage did not cause an increase or decrease in the noise.

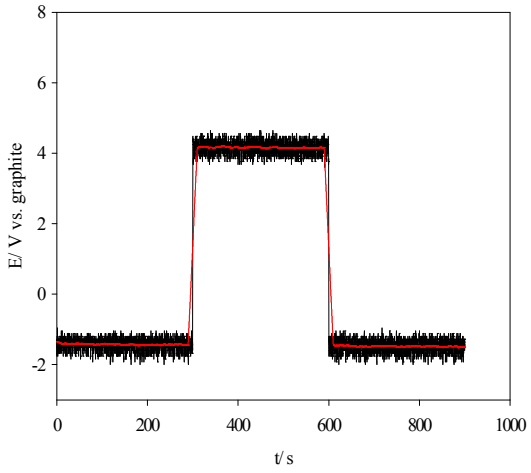

Figure 4-8: Time-based potentiometry experiment using the dynamic electrode vs. graphite rod in a bare flame (H_2 / O_2: 1.2 / 0.4 $Lmin^{-1}$). The W electrode was polarised positive with respect to the 1.5 mm length Pt coil. Refer to Figure 4-1 caption for details regarding data representation.

4.3.3 Hydrogen rich and oxygen rich flame environment

The gas composition of the LHS flame where the dynamic electrode was positioned was varied. The gas composition was varied from H_2 / O_2: 1.5 / 0.1 L min^{-1} to 0.9 / 0.7 1 L min^{-1} to allow the flame to move from a hydrogen rich to

an oxygen rich environment. The graphite rod was kept in the RHS flame with a constant gas composition - H_2 / O_2: 1.2 / 0.4 $Lmin^{-1}$.

An example of the measurement taken with the dynamic electrode placed in a hydrogen rich flame is shown in Figure 4-9a. The OCP was measured between 0 and 200 s before the potentiometer was connected. With the voltage divider setting, voltage was applied. Throughout the experiment asymmetric downward peaks were observed.

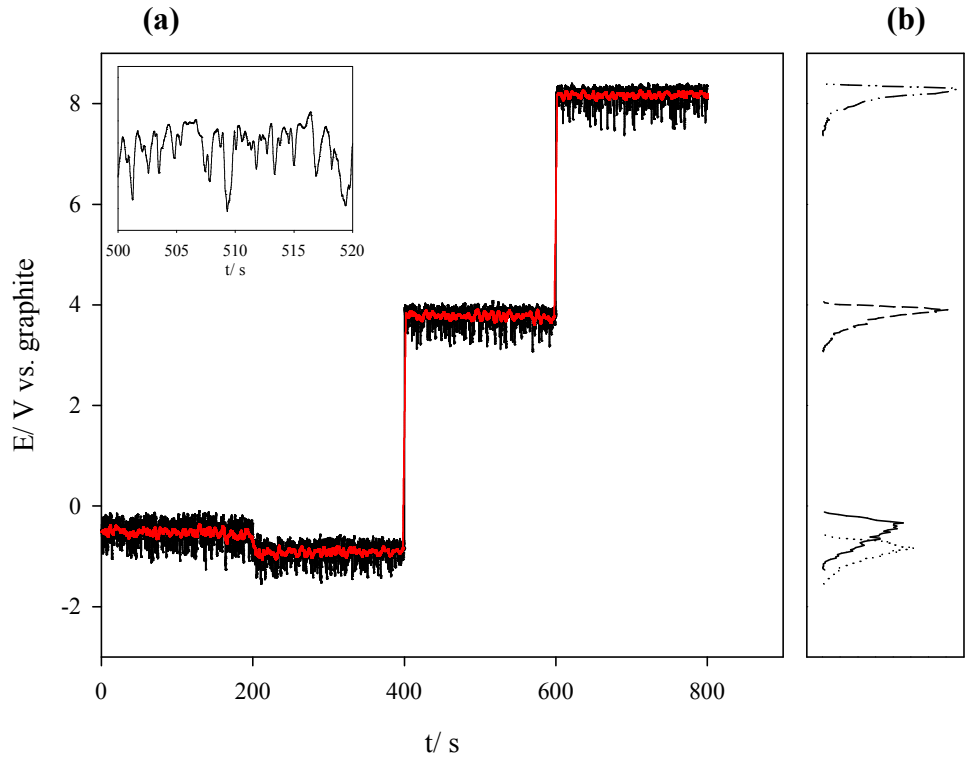

Figure 4-9: (a) Time-based potentiometry experiment using the dynamic electrode vs. graphite rod in hydrogen rich flame (H_2/O_2: 1.3/0.3 L min^{-1}). The W electrode was polarised positive with respect to the Pt coil. Raw data is shown in black. Running average with 400 points shown in red (400 points = 4 s) Inset: negative asymmetry peaks. (b) Histogram showing the negative asymmetric peaks. Data points from the maximum to minimum voltage were divided into 50 bins. The same number of points were analysed for each histogram.

Analysis of these peaks (Figure 4-9b) suggests that the asymmetry is not a direct consequence of the dynamic set-up since the OCP also has negative asymmetric peaks. The connection of the potentiometer alone does not affect the asymmetry; however the application of voltage does significantly increase the asymmetry of the peaks. The application of 4.5 V increased the asymmetry, which further increased as the voltage was increased to 9 V.

When the LHS flame was changed to an oxygen rich environment, asymmetric positive voltage peaks were observed. An example of this is shown in Figure 4-10a.

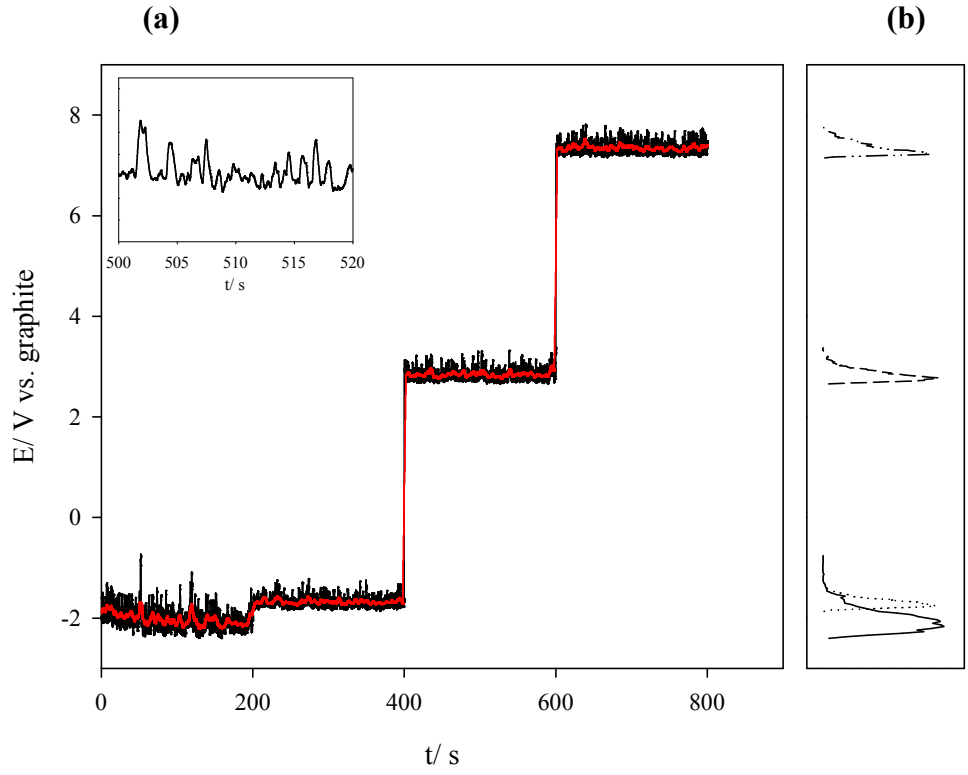

Figure 4-10: Time-based potentiometry experiment using the dynamic electrode vs. graphite rod in oxygen rich flame (H_2/O_2: 1.0/0.6 L min^{-1}). The W electrode was polarised positive with respect to the Pt coil. Raw data is shown in black. Running average with 400 points shown in red (400 points = 4 s) Inset: positive asymmetric peaks. (b) Histogram showing the positive asymmetric peaks. Data points from the maximum to minimum voltage were divided into 50 bins. The same number of points were analysed for each histogram.

The OCP was again recorded between 0 and 200 s before the potentiometer was attached. Between 200 and 800 s, the same voltage was applied as those used in the hydrogen rich flame. The positive asymmetric peaks were observed both with the OCP and with the applied voltage. The voltage applied did not serve to increase or reduce the asymmetry.

A control experiment was conducted with two graphite rods under the same experimental conditions (Figure 4-11).

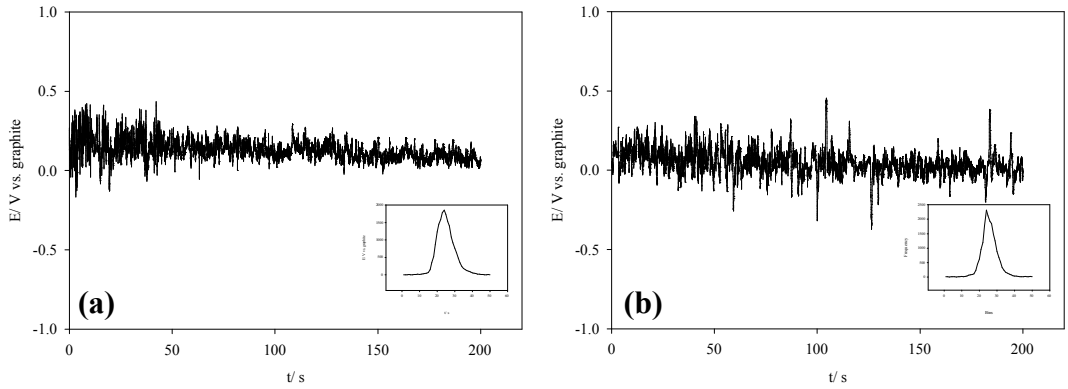

Figure 4-11: Time-based control potentiometry experiment using two graphite rods in (a) hydrogen rich (H_2/O_2: 1.3/0.3 L min^{-1}) and (b) oxygen rich flame environment (H_2/O_2: 1.1/0.5 L min^{-1}). Inset: Histograms of symmetrical peaks

It is seen from the control experiment that for a graphite electrode, there was no preference for asymmetric peaks to form in either flame environments. The results presented here suggest that the flame environment has a direct influence on the symmetry of the peaks observed when using a W wire or dynamic W electrode. It cannot be argued that the temperature of the flame influences the asymmetry of the peaks because the surface temperature of both electrodes in hydrogen rich and oxygen rich flames reduce to approximately 800 °C as the gas ratio is moved away from stoichiometry (1300 ± 75°C).

In addition, it has been shown that the applied positive voltage can increase the degree of asymmetry in a hydrogen rich flame but not in an oxygen rich flame.

The rationale is thought to be linked to the positive voltage not able to increase the dominant thermal oxidation process that occurs in an oxygen rich flame, however, electrochemically, the positive voltage can have a direct effect in a hydrogen rich (reducing) flame.

In situ Raman analysis was used to confirm that the different flame environments were inducing contrasting chemical reactions to occur at the surface of the W wire electrode.

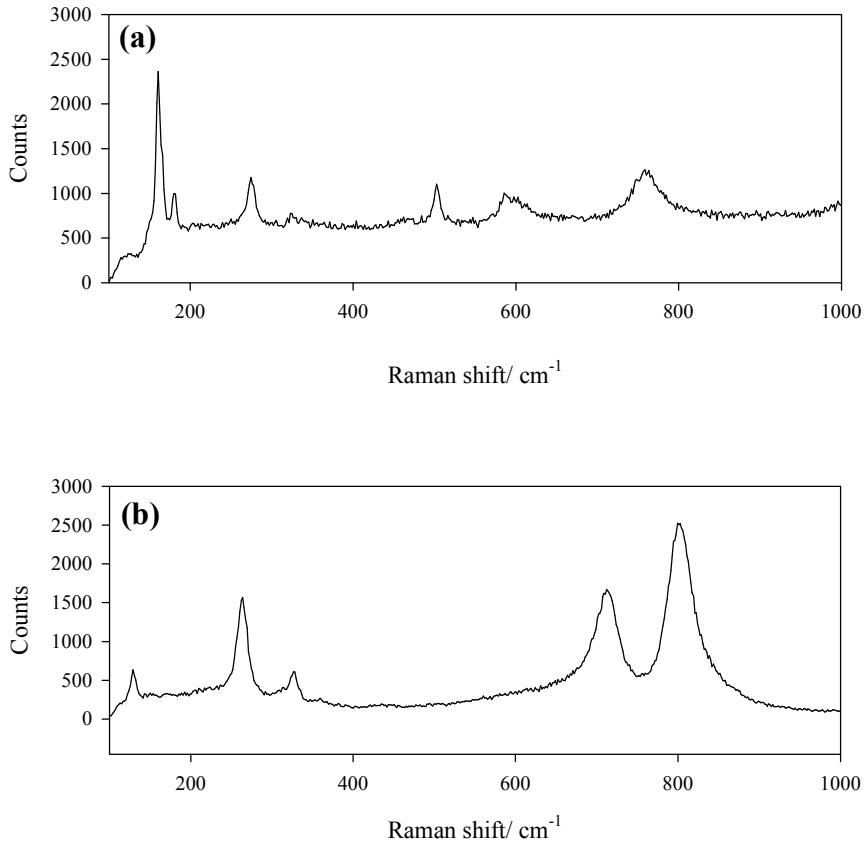

Figure 4-12: *In situ* Raman analysis (a) formation of an unknown material on the dynamic W electrode surface in a hydrogen rich, (b) formation of WO_3 on the dynamic W electrode surface in an oxygen rich flame.

A non-stoichiometry or lower oxide was formed on the surface of the electrode in a hydrogen rich flame (Figure 4-12). The hydrogen rich environment behaves

as a reducing agent which possibly inhibited the formation of the thermodynamically favorable / fully oxidised WO_3. Another viable possibility was that WO_3 does form on the surface of the electrode due to entrainment of air from the surrounding environment but after the formation of WO_3 on the surface, it is instantaneously reduced by hydrogen to a lower oxide. The applied positive voltage can be seen as a resistive action to the reduction process by inducing the oxidation process; however, because the thermal reduction process is more dominant and/or the voltage applied is not large enough to create a more significant change. In comparison, oxygen rich flame environments caused direct thermal oxidation to occur on the surface of the electrode. The thermal oxidation is dominant and the applied voltage could further increase the rate of oxidation.

4.3.4 Changing gas composition

The concentration of ions present in a flame is predominantly determined by the gas composition used. The voltage and noise response was investigated by varying the gas ratio of two flames, a bare flame and a flame containing 0.5 mM CsOH. Table 4-1 summarises the results of varying the gas ratio in a bare flame and doped flame.

Gas Ratio H_2 / O_2 (L min^{-1})	**Average p.d. in bare flame (V)**	**Average p.d. in doped flame (V)**
1.2 / 0.4	-1.11 ± 0.11	-0.56 ± 0.06
1.3/ 0.3	-0.79 ± 0.09	-0.21 ± 0.05
1.4/ 0.2	-0.34 ± 0.09	0.06 ± 0.04
1.5/ 0.1	-0.36 ± 0.06	0.58 ± 0.03

Table 4-1: Mean potential difference of using the dynamic electrode (W electrode polarised positive with respect to Pt coil – 0 V applied) vs. graphite rod in a bare and doped flame (0.5 mM CsOH) with varying gas ratios. Experiment conducted over 300 s.

The potential differences measured in the bare and doped flames follow the same trend, albeit the potential differences in the doped flames were less negative than those measured in the bare flame. By doping the flame, it was shown that the voltage is characteristic of the identity of the specie(s) in the flame.

The potential difference became less negative in both flames as the hydrogen concentration was increased and the oxygen concentration was decreased. By changing the gas concentrations in this manner, incomplete combustion occurred, which caused a reduction in concentration of ionised species present in the flame. In addition, by moving away from stoichiometry, the flame temperature reduced, which resulted in lower electrode surface temperature. The reduced surface temperature of the electrodes is reflected in the reduction of the noise as the gas ratio is varied. The noise can therefore be reduced from 110 mV to 30 mV by the manipulation of the hydrogen and oxygen concentrations and by the inclusion of doped flame species. The noise deviation could not be reduced further by increasing the concentration of CsOH as shown in Figure 4-13 where the concentration was increased from 0.5 mM to 2 mM.

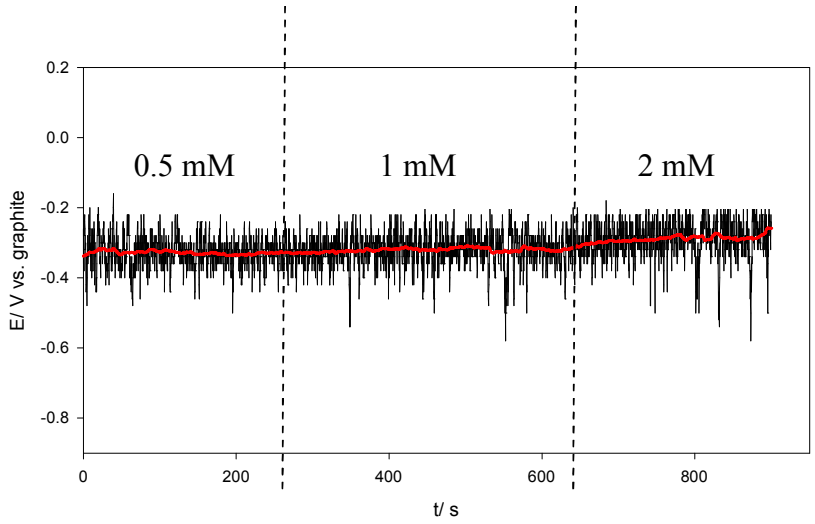

Figure 4-13: Time-based potentiometry experiment using the dynamic electrode vs. graphite rod in a flame (H_2 / O_2: 1.2 / 0.4 $Lmin^{-1}$) doped with increasing concentration of CsOH. The W electrode was polarised positive with respect to Pt coil (0 V applied). Refer to Figure 4-1 caption for details regarding data representation.

With the flame split, the dynamic electrode was placed in a flame doped with 0.5 mM CsOH and a graphite rod was placed in a bare flame. The gas ratio of the doped flame was varied while the bare flame gas composition was kept constant (Table 4-2).

Gas Ratio H_2 / O_2 (L min^{-1})	Average p.d. in bare flame (V)
1.2 / 0.4	-0.88 ± 0.09
1.3/ 0.3	-0.77 ± 0.05
1.4/ 0.2	-0.49 ± 0.04
1.5/ 0.1	-0.18 ± 0.04

Table 4-2: Mean potential difference and noise deviation of time-based potentiometry experiments using the dynamic electrode vs. graphite rod. The W electrode was polarised positive with respect to the Pt coil in a flame (0 V applied). The LHS flame was doped with 0.5 mM CsOH and the RHS flame remained untreated. The gas ratio of the LHS was varied and the RHS was kept constant at H_2 / O_2: 1.2 / 0.4 $Lmin^{-1}$. Experiment conducted over 300 s.

The results presented in Table 4-2 are a direct compliment of the results presented in Table 4-1. The average potential differences became less negative and the noise lowered as the flame was made more hydrogen rich and oxygen rich.

4.4 Summary

The noise associated with an exposed reference wire has been significantly reduced by using a Pt coil to shield the wire from the extreme heat of the flame, and in turn reducing the amount of evaporation that occurs on the electrode surface. The electrode lifetime was also increased by using the Pt coil shield.

The connection of the potentiometer to both the reference wire and Pt wire caused the voltage to become instantly stable. The negative voltage applied to the

reference wire served to increase the rate of evaporation by possibly causing the reduction of the reference metal oxide, which in turn causes the reduced metal particles (loosely bound on the electrode surface) to be rapidly thermally oxidised. The positive voltage applied to the reference wire does not increase or decrease the noise.

It has been shown that the flame environment has a direct influence on the symmetry of the voltage peaks. When the flame was made hydrogen rich, negative asymmetric peaks were observed. In contrast, positive asymmetric peaks were observed when the flame was made oxygen rich. *In situ* analysis suggests that the peak asymmetry is linked to different oxides being made on the electrode surface. When the gas composition was moved away from stoichiometry, the noise was reduced and further reduced by the addition of $CsOH$ into the flame.

Although the evaporation process occurring on the surface of the reference wire has been reduced by the Pt shielding, the lack of control of the evaporation process has been a concern throughout this chapter. In the next chapter, the design of an electrode with greater control of the evaporation process will be described. The use of these electrodes and metal wires will then be subjected to chronopotentiometry experiments to measure their ability to be used as reference electrodes.

5 Titanium/titanium dioxide pastes as reference electrodes

5.1 Introduction

The two previous chapters have highlighted the need for greater control over the reference electrode materials. This chapter shall describe the development of reference material pastes containing metal and their respective metal oxides. The control of reference materials were enhanced by placing the pastes into two types of supports (conducting graphite and non-conducting ceramic).

Potentiometry measurements were taken to assess the voltage stability of all metal/metal oxide reference pastes. In addition, candidates that showed good voltage stability were further analysed using chronopotentiometry to assess their polarisability. Characterisation techniques including Raman spectroscopy and X-ray diffraction were used to develop an understanding of voltage dependence upon the material composition.

5.2 Experimental

5.2.1 Materials

All metal and metal oxide powders were purchased from Sigma Aldrich Ltd. The metal wires were supplied by Advent Research Materials Ltd and Goodfellow Cambridge Ltd, whereas the platinum (Pt) wire was supplied by Johnson Matthey Ltd. The graphite rods (3 mm diameter) and alumina ceramic tubes

(inner diameter: 1.6 mm and outer diameter: 2.8 mm) were purchased from Agar Scientific Ltd and Dynamic Ceramic Ltd., respectively. Ethanol, supplied by VWR Ltd was used to mix the powders to form reference material pastes in all experiments. For each material, the highest purity available was selected. During chronopotentiometry experiments, the CE used was a 0.5 mm thick, square-shaped Pt flag (20 x 20 mm).

5.2.2 Electrode design and fabrication

Pellets containing reference materials were initially made but due to their size (2 mm diameter) and fragility, they could not be used as electrode material. The reference materials were made using pastes, and prepared by mixing appropriate amounts of metal (M) and their respective oxide (MO_x) powders together with a few drops of ethanol using a mortar and pestle to form homogenous reference materials. The ratio of M and MO_x were made using weight (w/w), e.g. 20/80 M/MO_x refers to 20 % M and 80 % MO_x.

Two contrasting reference material supports were used in this study, namely conducting graphite rod and non-conducting alumina ceramic tube.

Graphite rod support: The support consisted of a cavity that was made at the 'front' end (flame side) of the graphite rod using a drill, into which, the reference material (30-40 mg) was packed using a spatula, as shown in Figure 5-1.

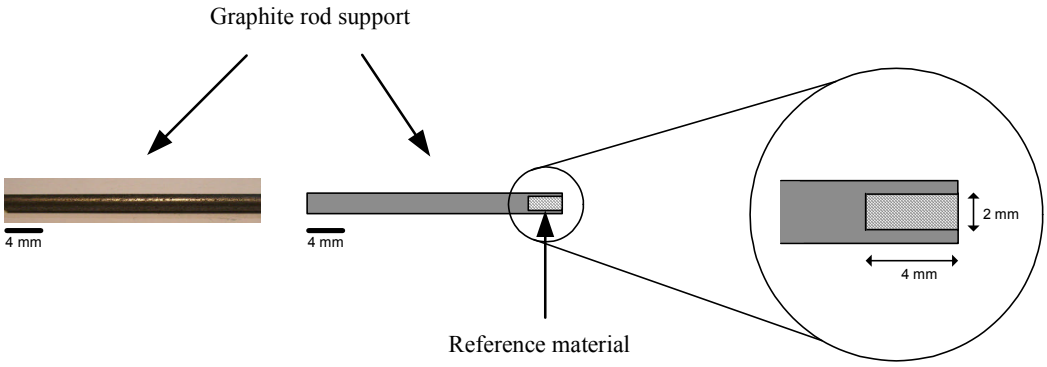

Figure 5-1: Electrode design of the 30 mm length graphite rod. A 4 mm deep cavity was made at the 'front' end with a 2 mm diameter drill allowing the reference material paste to be incorporated. The electrical connection was made directly onto the graphite rod.

Ceramic tube support: As a routine exercise, the commercial ceramic tubes were pre-conditioned by being placed in a clean flame for 60 s. The thermal analysis (TA) performed on both the pre-conditioned and non-conditioned commercial ceramic tubes (Figure 5-2) justify the use of pre-conditioning. The analysis was carried out under controlled thermal treatment.

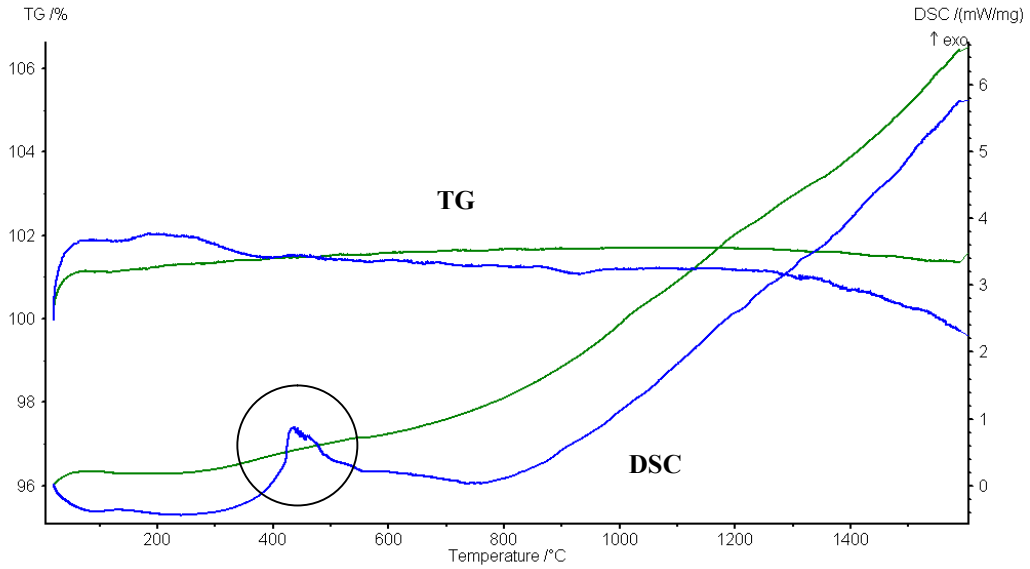

Figure 5-2: TA of non-conditioned (blue) and conditioned (green) ceramic tubes in a clean flame. The temperature was ramped from room temperature up to 1590 °C in air with a heating rate of 10 °C / min. The sample was held at this maximum temperature for 120 s and left to cool to room temperature spontaneously.

The non-conditioned ceramic tube showed an exothermic peak (circled) seen on the DSC trace (blue line) occurring with an onset temperature of 350 °C. The broad peak coupled with a small decrease in mass, shown in the TG trace (blue line), is likely to be the consequence of a combustion process of impurities and/or additives within the chemical composition of the ceramic tubes. The response from the conditioned electrode (green DSC line) shows that the broad peak has been eliminated. As a direct consequence from conditioning the ceramic tube supports, the reproducibility and stability of the electrochemical measurements presented further in the discussion was greatly increased.

An electrical connection was made by placing a nichrome wire inside the tube ensuring it was 3 mm away from the 'front' end of the tube as shown in Figure 5-3. The distance away from the 'front' end was to ensure that the wire was not in contact with the flame. With the nichrome wire in a fixed position, the reference material was packed 3-4 mm deep inside the 'front' end of the ceramic tube ensuring that a secure contact was made with the wire.

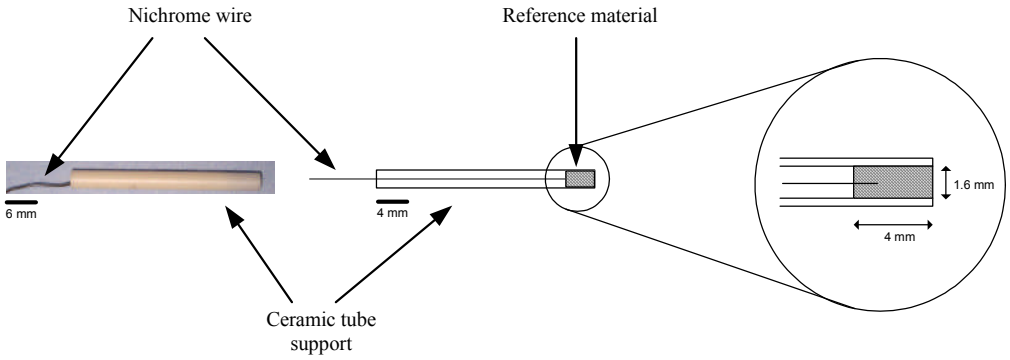

Figure 5-3: Electrode design of the 40 mm length ceramic rod. The 0.5 mm diameter nichrome wire was positioned 3 mm away from the 'front' end of the ceramic tube. The reference material was then packed inside the 'front' end. Electrical connection was made to the 100 mm length nichrome wire which was in firm contact with the paste.

Before the electrodes could be used, both supports packed with reference material pastes were placed into an oven at 65 °C for 10 minutes to allow residual solvent to evaporate from the paste.

Refer to Chapter 2 for further details regarding experimental procedures.

5.3 Results and Discussion

5.3.1 Potentiometry measurements of reference materials using conducting graphite support

Graphite rods packed with different reference material pastes were used as individual electrodes. The pastes consisted of 50/50 (w/w) of M/MO_x powders. Zero current potentiometric measurements were carried out with these electrodes against pure graphite rods. The potential difference for five different reference electrode materials are summarised in Table 5-1. Within 10 s of all the measurements, an initial dramatic voltage shift was observed due to the heating process of the electrodes. The average potential difference was taken from when the voltage became stable.

Metal / metal oxide	Mo / MoO_3	Fe / Fe_2O_3	Nb / NbO_2	Ti / TiO_2	Zn/ZnO
Average potential (V)	-0.58 ± 0.38	-0.47 ± 0.09	-0.32 ± 0.10	-0.25 ± 0.10	-0.10 ± 0.10

Table 5-1: Average potential difference of 50/50 M/MO_x reference material packed into graphite rod supports vs. pure graphite rod. Each time based experiment voltage was recorded for 2000 s.

Molybdenum/molybdenum trioxide (Mo/MoO_3) gave the most negative potential (-0.58 V) compared to zinc/zinc oxide (Zn/ZnO) which gave the least negative potential (-0.10 V). The potential arising from the five electrodes was likely to be due to contributions from the conducting graphite support as well as from the reference material. Molybdenum/molybdenum trioxide behaved different to the other materials, with its respective noise being significantly

higher. This is likely to be associated with the sublimation and evaporation of MoO_3 which occurs at 1155 °C.

5.3.2 Potentiometry measurements of reference materials using non-conducting ceramic support

The purpose of using the ceramic support was to eliminate the contribution of the conducting graphite supports towards the overall potential difference observed. The findings have been summarised in Table 5-2. Due to the low melting point of Zn (420 °C) and the high surface temperature of the ceramic tube support (1380 ± 100 °C), Zn/ZnO could not be used as a reference material within the support. The potential differences were again measured from when the voltage became stable.

Metal / metal oxide	Mo / MoO_3	Fe / Fe_2O_3	Nb / NbO_2	Ti / TiO_2
Average potential difference (V)	-1.55 ± 0.15	-1.14 ± 0.07	-0.90 ± 0.06	-0.56 ± 0.07

Table 5-2: Average potential difference of 50/50 M/MO_x reference material packed into ceramic tube supports vs. graphite rod. Each time based experiment voltage was recorded for 2000 s.

The difference in the spread of the voltage between the two supports is primarily due to the different supporting material used. The surface area of the graphite rod support in relation to the reference material in the flame was much larger; hence the voltage was dominated by the graphite rod. As a direct consequence, the potential difference was close to 0 V, since the other electrode used was also a graphite rod having a similar surface area. The spread of the potential differences using the ceramic holder is much larger owing to the elimination of the conducting graphite support, demonstrating that the potential difference arose solely from the identity of the reference material.

It is clear that the voltage trend of the reference materials are consistent with both supports, i.e. most negative: **Mo / MoO_3 < Fe / Fe_2O_3 < Nb / NbO_2 < Ti / TiO_2**: least negative. The agreement in the trend suggests that the voltages using the ceramic supports are due only to the reference materials.

An important observation from the time-based experiments was the voltage stability over time. Apart from titanium/titanium dioxide (Ti/TiO_2), all reference materials showed a slow gradual voltage drift throughout the experiments possibly linked to a change or a transformation of the pastes over time within the supports. Titanium/titanium dioxide showed the lowest voltage drift as shown in Figure 5-4 and became and remained stable after 500 s. In contrast, the niobium/niobium dioxide (Nb/NbO_2) response showed a continuous voltage drift up until 800 s.

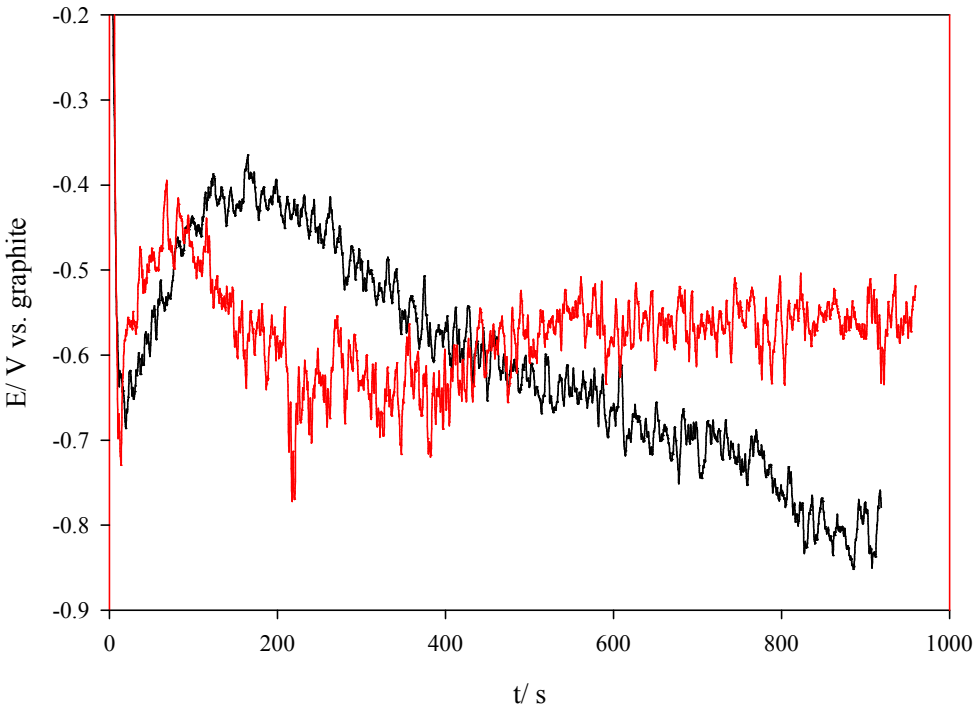

Figure 5-4: Time based potentiometry measurements of Ti/TiO_2 (red line) and Nb/NbO_2 (black line) reference materials packed into ceramic tube supports. Running average with 50 points (50 points = 5 s).

Taking into consideration the low voltage noise and good voltage stability of Ti/TiO_2 in comparison with the other materials, it was the ideal material to further explore the effect of varying the ratio of M and MO_x.

When the ratio of M and MO_x was varied, as shown with Ti and TiO_2 in Table 5-3, the voltages, excluding 100% TiO_2, were similar. This is likely due to the electrodes all containing both metal and metal oxide within them. The electrode containing 100% Ti formed an oxide surface layer once it was placed in the flame, as will be discussed further in the text.

Ti / TiO_2	100 / 0	80 / 20	60 / 40	40 / 60	20 / 80	0 / 100
Average potential difference (V)	-0.70 ± 0.06	-0.68 ± 0.05	-0.65 ± 0.07	-0.74 ± 0.06	-0.70 ± 0.06	-0.78 ± 0.08

Table 5-3: Average potential difference of varying Ti/TiO_2 ratios packed into ceramic tubes vs. graphite rod

The different reference electrode material investigated above, especially with Ti/TiO_2, has shown promising behaviour. However for a reliable reference electrode, in addition to voltage stability, it should be resistant to voltage changes when small amounts of currents are passed through it. This non- polarisable feature of Ti/TiO_2 was investigated and explored through chronopotentiometry, with the results and discussion being given in the following section.

5.3.3 Chronopotentiometry measurements of metal wires

Chronopotentiometry was used to investigate four metal wires to assess their ability to behave as non-polarisable electrodes. Platinum, known as being a good polarisable material, was used as a 'baseline' to compare the non polarisable features of three other materials. The current passed through the electrode ranged from 10×10^{-9} A to -10×10^{-9} A and the voltage recorded is shown in Figure 5-5.

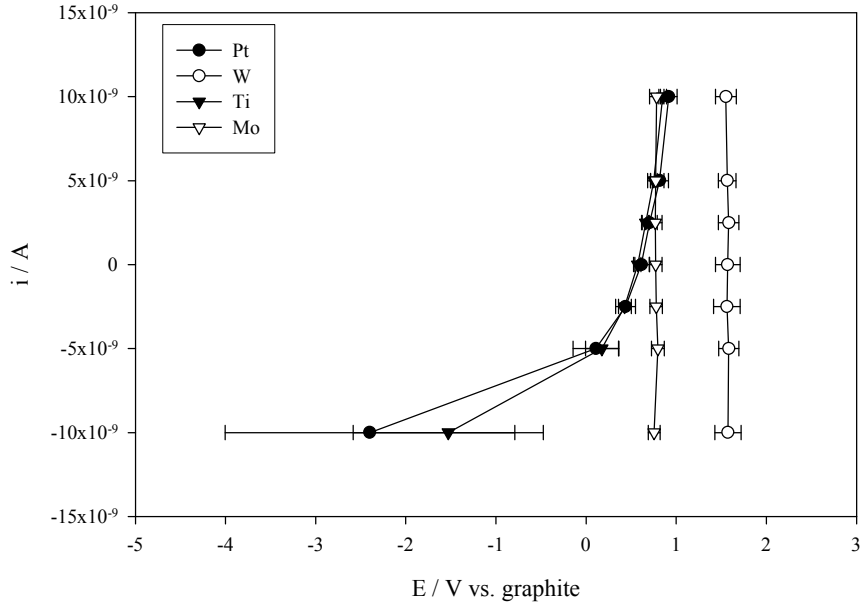

Figure 5-5: I-V polarisability curve for exposed Pt, W, Ti and Mo (50 mm length) wire electrodes. Step currents (10 s each) from 10 x 10^{-9} A to -10 x 10^{-9} A were passed through the electrode and voltage recorded.

It is shown through Figure 5-5 that Pt does behave as a polarisable material. This is shown by the large change in the voltage when small negative currents were passed through the wire. Both tungsten (W) and Mo showed good responses, i.e. only small changes in the voltage were recorded when small positive and negative currents were passed through the electrodes. The sacrificial nature of these materials (discussed in Chapter 3) is likely to be the underlying factor in ensuring that these electrodes are non-polarisable. Although these two materials possess a desirable feature needed for a reference electrode, both materials lack another important feature, namely voltage stability. When repeated current measurements (10 successive scans) were taken, a voltage drift of 240 mV was observed with W (Figure 5-6a). A similar response was seen with Mo; however a larger voltage drift of 469 mV was recorded (Figure 5-6b).

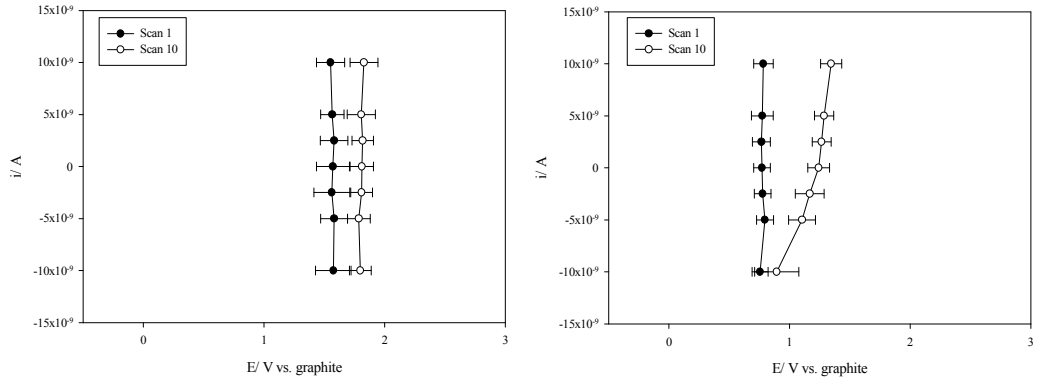

Figure 5-6: I-V polarisability curve for exposed (a) W wire electrode (b) Mo wire electrode. Step currents (10 s each) from 10 x 10^{-9} A to -10 x 10^{-9} A were passed through the electrode and voltage recorded. Only Scan 1 and Scan 10 are shown in the Figures.

In contrast to both W and Mo, the Ti wire appeared to be a polarisable material with its response more closely resembling that of Pt (Figure 5-5). However, unlike W and Mo, its voltage drift, 23 mV was significantly lower over ten scans (Figure 5-7).

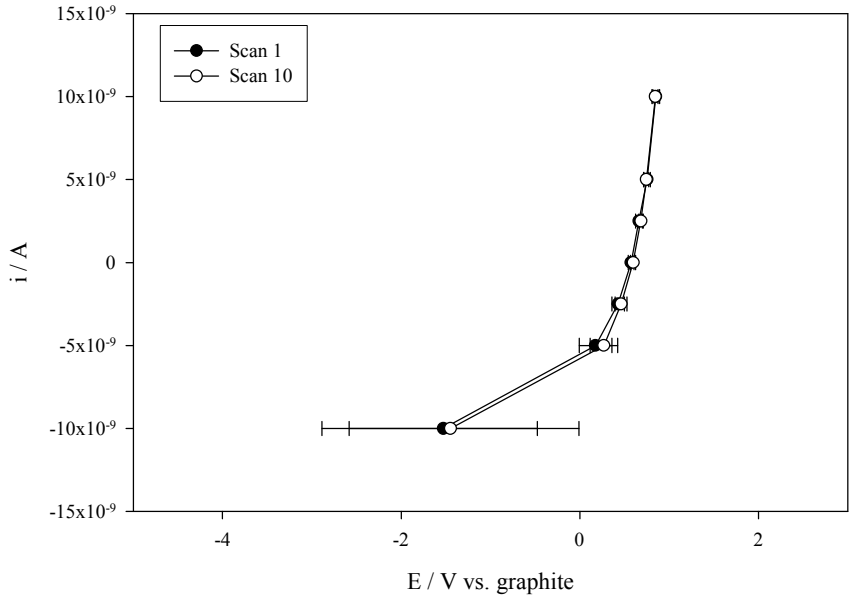

Figure 5-7: I-V polarisability curve for exposed Ti wire electrode. Step currents (10 s each) from 10 x 10^{-9} A to -10 x 10^{-9} A were passed through the electrode and voltage recorded. Only Scan 1 and Scan 10 are shown in the Figure.

The flame is considered to be an open system where air from the surroundings contributes to the overall combustion process. This process provides a suitable medium in which oxidation of these materials can occur. The unique physical characteristics of these three materials contribute to the different responses observed. Critically, the melting point of TiO_2 (most thermodynamically stable oxide) is 1825 °C, which is slightly lower than the calculated adiabatic temperature (2200 °C) of the flame. In contrast, both the melting points of MoO_3 (795 °C) and WO_3 (1473 °C) are significantly below the adiabatic flame temperature. The consequence of the differences in temperature resulted in the evaporation of MoO_3 and WO_3 from the surface of the wire exposing a fresh layer of metal (Figure 5-8a and b), whereas TiO_2 (Figure 5-8c) did not form (or formed at a very slow rate) which resulted in a response similar to Pt.

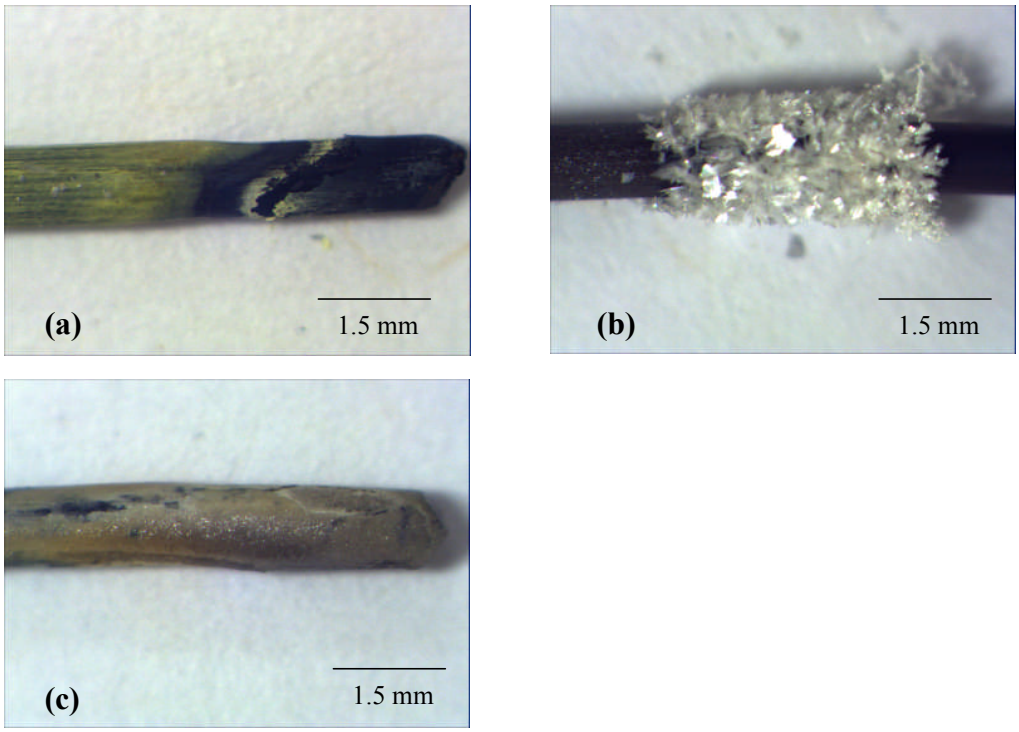

Figure 5-8: *Ex situ* images of sacrificial reference electrodes: (a) tip of W wire showing the oxide formed, note the tip is thinner due to evaporative loss of material, (b) tip of Mo wire showing the oxide formed. Oxide formation, sublimation and evaporation processes are thought to be linked to the continuous voltage shift, (c) tip of Ti wire showing the layer of oxide formation but critically no or very little evaporation.

The formation of MoO_3 and WO_3, and the subsequent evaporation of the surfaces are believed to be of central importance to achieving the non-polarisable features observed in Figure 5-5.

Although the evaporation of the oxide is seen to be a critical feature in ensuring a non-polarisable response is observed, it is also highly likely to be the significant factor for the voltage drifting. The continuous evaporation, resulting in the reduction of surface area and the position of the electrode in flame is likely to be the sole contributor to why the voltage drift occurs. The same reasoning can be applied to the slow voltage drift seen with the exposed Ti wire electrode, because evaporation of the oxide did not occur or if it did, it happened at a very slow rate.

To combine the desirable features of a non-polarisable interface and a constant voltage electrode, paste containing Ti and TiO_2 were used. It has already been shown that TiO_2 does not melt at the flame temperature and so, by packing pastes into ceramic tubes, it was hoped that the non-polarisable feature of Ti/TiO_2 could be enhanced.

5.3.4 Chronopotentiometry measurements of titanium/titanium dioxide in ceramic support

5.3.4.1 Varying ratio of titanium/titanium dioxide reference material

Five ratios of Ti/TiO_2 ranging from 100/0 to 0/100 w/w were chosen and measured to determine the ratio(s) that give the optimum non polarisable response. The five responses were compared to a Pt pellet electrode which exposed a similar surface area to the flame (Figure 5-9).

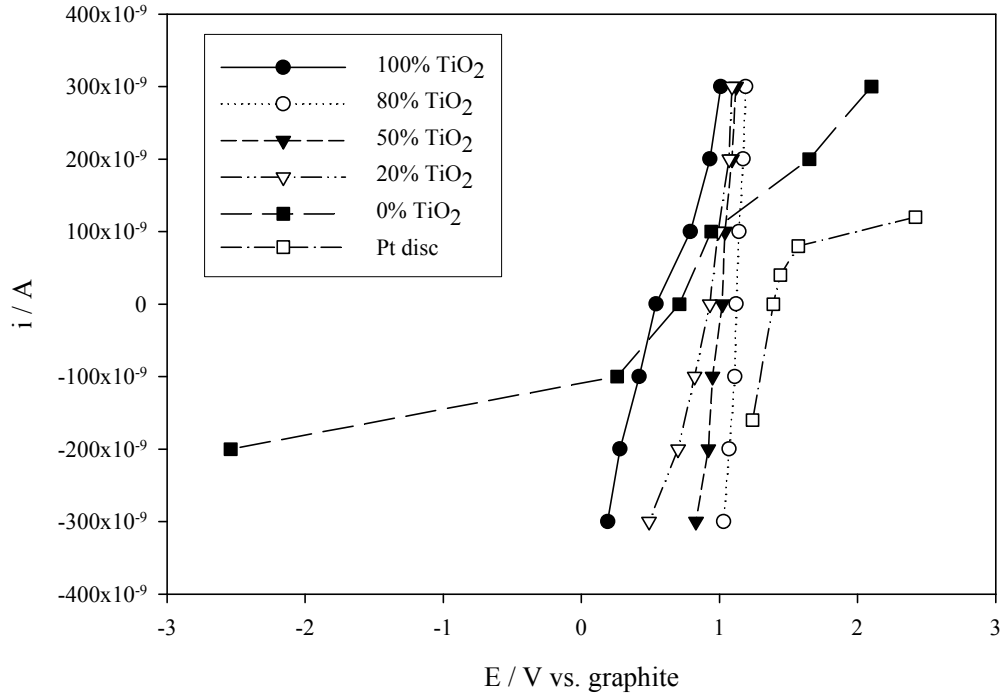

Figure 5-9: I-V polarisability curve for different ratios of Ti/TiO_2 packed into ceramic tubes. A Pt disc of similar surface area as the paste exposed to the flame was used as a marker. Step currents (10 s each) from 300 x 10^{-9} A to -300 x 10^{-9} A were passed through the electrode and voltage recorded.

Similar to the responses observed with the exposed metal wires, both the Pt disc and 100/0 Ti/TiO_2 reference material exhibit similar features. They both have a limited current range between 100 x 10^{-9} A to -100 x 10^{-9} A whereby the voltage does not change dramatically. However when ratios of metal and metal oxide reference materials were investigated, in this case, 20/80, 50/50 and 80/20 Ti/TiO_2, the responses were very similar to each other. This suggests that the non-polarisable feature becomes more enhanced when M and its MO_x are incorporated together, also seen with W and Mo exposed wires. An advantage of using pastes is that the relative concentrations of M and MO_x can be controlled and optimised whereas the same cannot be applied to the sacrificial metal wires.

When 0/100 Ti/TiO_2 reference electrode was used, the response was similar to that of the metal-metal oxide mixtures; however it was more polarisable due possibly to no metal being present. In general, Figure 5-9 suggests that the best responses can be achieved from electrodes which have pastes containing M and its MO_x.

5.3.4.2 Comparison of 20/80 Ti/TiO_2 vs. 80/20 Ti/TiO_2 reference material.

Two reference materials (20/80 and 80/20 Ti/TiO_2) were investigated to understand the behaviour of the Ti/TiO_2 reference electrode. Although the w/w percentages of the two compositions were contrasting, this was not the case for their mole fractions. The mole fraction of Ti and O_2 in a 20/80 Ti/TiO_2 composition was similar, 0.586 and 0.414 respectively. In comparison, the mole fraction of Ti and O_2 in a 80/20 Ti/TiO_2 composition was calculated as 0.987 and 0.013 respectively. The investigation was critical to understand how the electrodes established and maintained its potential. The role of the material composition towards the electrode potential will be examined in Section 5.3.5.

A series of six successive scans were conducted using a 20/80 Ti/TiO_2 reference electrode and the results shown in Figure 5-10. The potential stated in these measurements refer to the potential at zero current.

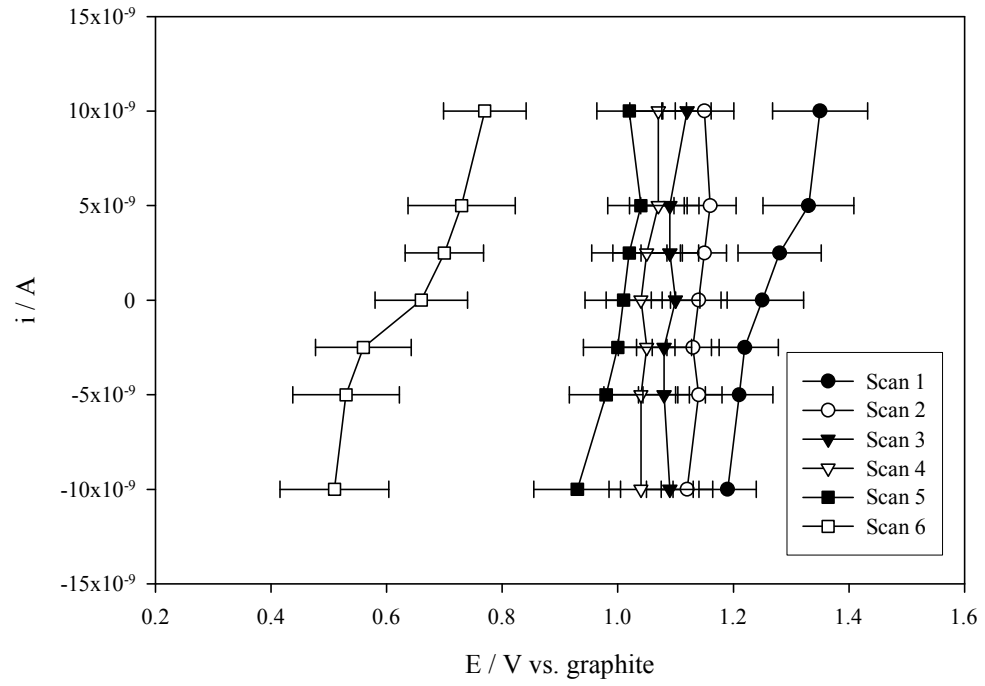

Figure 5-10: I-V polarisability curve of 20/80 Ti/TiO_2 reference material electrode. Step currents (10 s each) from 10 x 10^{-9} A to -10 x 10^{-9} A were passed through the electrode and voltage recorded. Error bars represent standard deviation.

The initial potential of scan 1 was 1.25 V which drifted in the negative direction and ended at 0.66 V (scan 6). The 0.59 V difference between scan 1 and scan 6 was larger than the 0.02 V shift recorded using the exposed Ti wire over a ten scan period. An explanation for this difference shall be proposed further in the work (Section 5.3.5.2). The voltage shift between scan 1 and scan 2 was 0.11 V. The first scan in an electrochemistry experiment is often anomalous. Once a new electrode is placed in the flame, the complete evaporation of ethanol in combination with the physical change of the compound from a paste into a pellet may explain the large shift between scan 1 and scan 2. The response from scan 2 to scan 5 are all consistent, with only a 0.13 V shift between them. A more important and significant observation from the 20/80 Ti/TiO_2 electrode response is the large voltage shift (0.35 V) between scan 5 and scan 6 which was not consistent with the previous scans. This uncharacteristic potential shift was thought to be linked to a change in the chemical composition of the electrode.

The response from subjecting an 80/20 Ti/TiO_2 electrode to the same electrochemical treatment is shown in Figure 5-11.

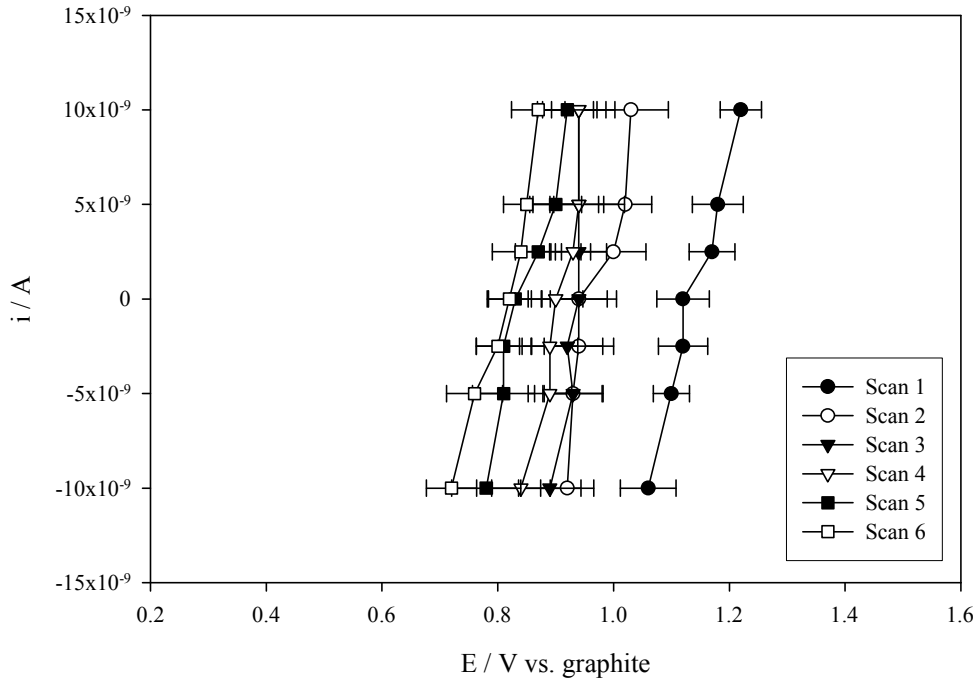

Figure 5-11: I-V polarisability curve of 80/20 Ti/TiO_2 electrode. Step currents (10 s each) from 10 x 10^{-9} A to -10 x 10^{-9} A were passed through the electrode and voltage recorded.

From scan 1 (1.12 V), the voltage drifts in the same direction as observed with the 20/80 Ti/TiO_2 electrode. However, the total drift from scan 1 to scan 6 (0.30 V) is smaller compared to that seen with the 20/80 Ti/TiO_2 electrode. In addition, similar to that seen with 20/80 Ti/TiO_2 electrode, an inconsistent 0.18 V shift occurred at the beginning of the measurement between scan 1 and scan 2. The reason for this is likely to be the same as that previously explained.

In contrast to the 20/80 Ti/TiO_2 electrode, the voltage shift (0.12 V) from scan 2 to scan 6 is consistent, with no large shifts seen between scan 5 and scan 6. It is believed that the difference in the electrode composition is directly linked to the different responses seen between the two compositions.

A series of experiments were devised to establish the role of the material composition of the electrodes in relation to the electrochemical results obtained. Three 20/80 Ti/TiO_2 electrodes (Electrode 1, 2, and 3) were prepared and subjected to a number of different scans, 1, 3, and 10 respectively. The electrochemical response for Electrode 3 (10 consecutive scans) is shown below in Figure 5-12.

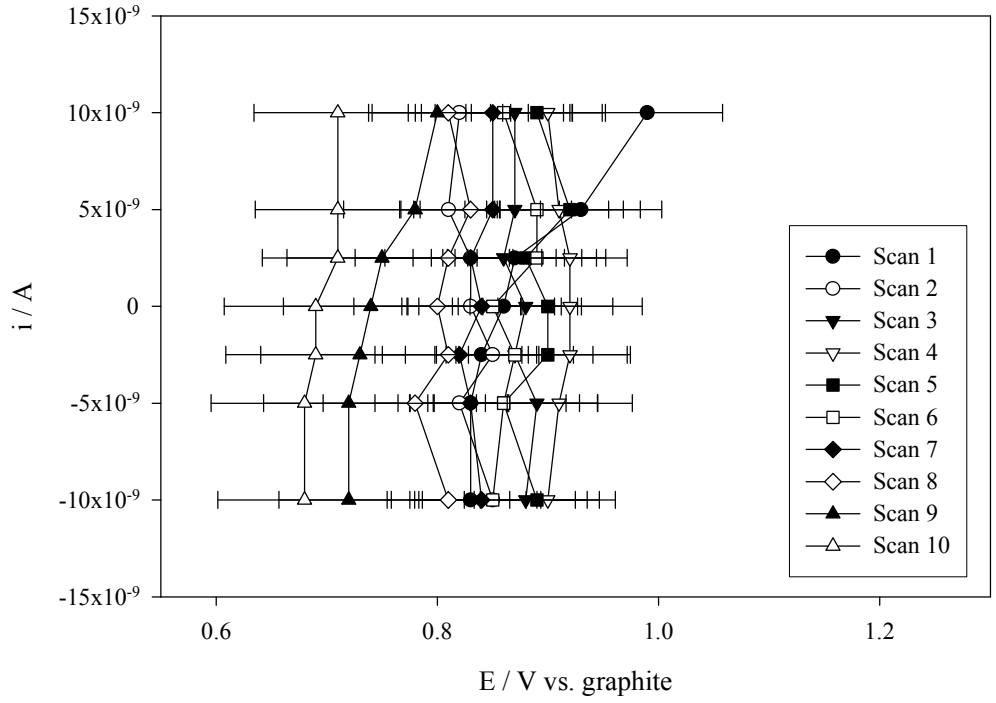

Figure 5-12: I-V polarisability curve of 20/80 Ti/TiO_2 Electrode 3. Step currents (10 s each) from 10 x 10^{-9} A to -10 x 10^{-9} A were passed through the electrode and voltage recorded.

The response shown in Figure 5-12 is similar to that seen in Figure 5-10, however, the onset of the large voltage shift occurred later between scan 8 and scan 9. The reason for this variation is likely to be due to small differences in the amount of reference material packed and the positioning of the nichrome wire inside the ceramic tubes.

A series of identical experiments were conducted using 80/20 Ti/TiO_2 as reference electrode material. The electrochemical response from using Electrode 3 is shown in Figure 5-13. As expected, the trend was similar to that previously seen in Figure 5-11 with no characteristic large voltage shift observed during the electrochemical response.

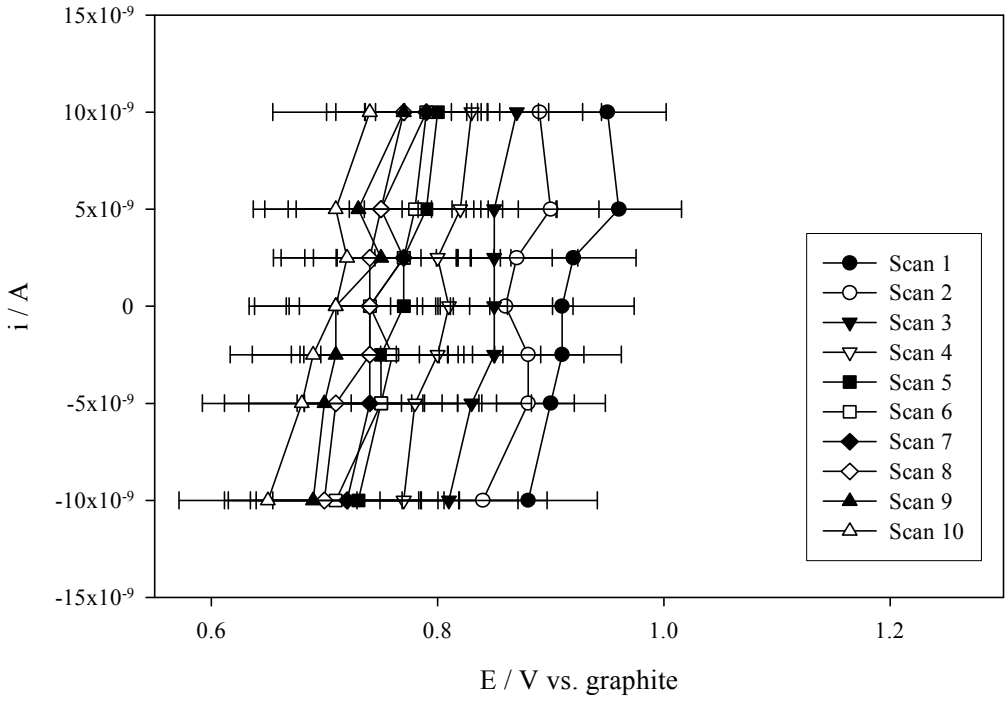

Figure 5-13: I-V polarisability curve of 80/20 Ti/TiO_2 Electrode 3. Step currents (10 s each) from 10 x 10^{-9} A to -10 x 10^{-9} A were passed through the electrode and voltage recorded.

The zero current voltage of each scan has been presented in Figure 5-14 for both 20/80 and 80/20 Ti/TiO_2 Electrode 3 to compare the voltage change over time. The voltage at scan 1 is similar for both 20/80 and 80/20 Ti/TiO_2 reference materials, 0.86 V and 0.91 V respectively. The voltage of the 20/80 Ti/TiO_2 began to decrease before increasing and reached a maximum potential (0.92 V) at scan 4. The voltage then begins to drift in the negative direction until scan 10 (0.69 V). In contrast, the 80/20 Ti/TiO_2 reference material has a negative voltage

drift from scan 1 to scan 10 (0.71 V). Although both reference materials follow different voltage trends, they both acquire similar voltages at scan 10.

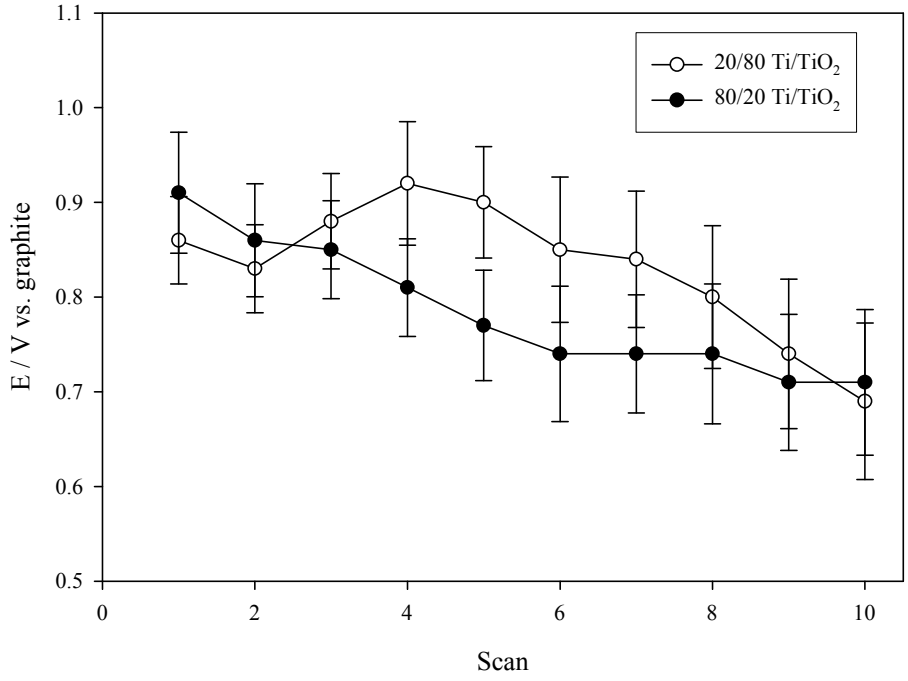

Figure 5-14: Zero current voltage of Electrode 3 for both 20/80 and 80/20 Ti/TiO_2 reference materials.

The gradient of each scan for both Electrode 3 (Figure 5-12 and Figure 5-13) was calculated to compare and assess their non-polarisable ability (Figure 5-15). The gradient of both electrodes decreased after scan 1, which may have been linked to the conditioning or sintering process that occurs within the material during the initial scan. From the second scan onwards, the gradients for both electrodes became larger over time indicating the increase in non-polarisability of the electrodes. An unexpected change in the gradient was noted during scan 9 of 20/80 Ti/TiO_2 but then settled to the regular pattern during scan 10. This sudden rise in the gradient coincidentally arose during the same scan where the sudden large voltage shift was seen in Figure 5-12.

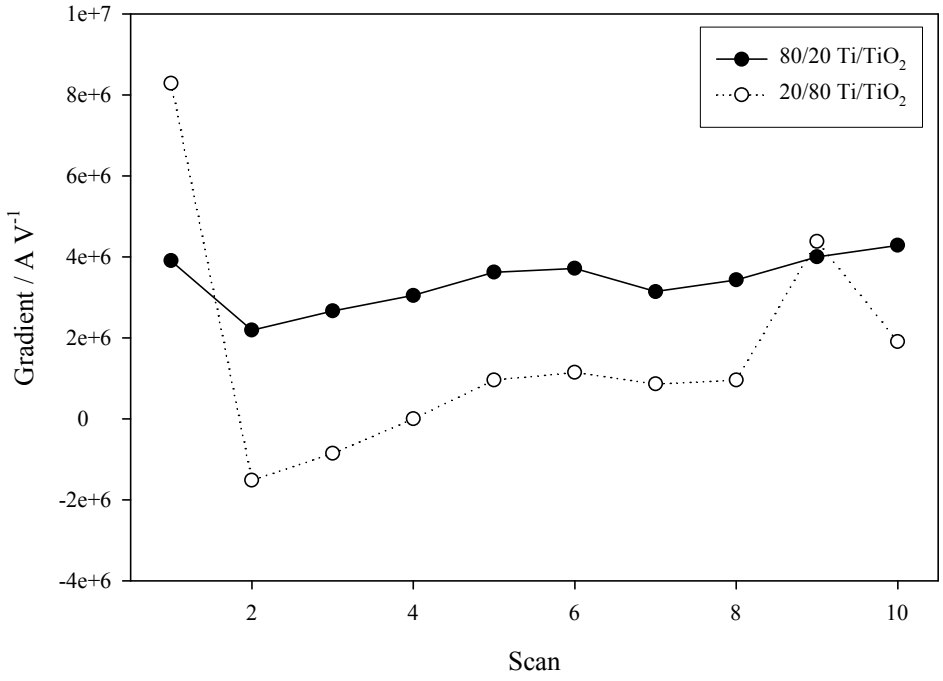

Figure 5-15: Gradient for each scan of both Electrode 3 reference materials to assess non-polarisability feature.

In the next section (5.3.5), the characterisation of the electrodes will provide an insight into the role of the reference material on the potential difference observed between the two materials.

5.3.5 Characterisation of electrodes

All three electrodes (Electrode 1, 2, and 3) of both compositions (20/80 and 80/20 Ti/TiO_2) were analysed by various techniques. The samples were cross-sectioned using a Dremel® mini rotary diamond saw and a Raman Spectroscopy line profile was collated. All samples were then ground to give homogenous powders before XRD and XPS analysis were conducted.

5.3.5.1 20/80 Ti/TiO_2

The initial pre-paste colour of 20/80 Ti/TiO_2 was light grey as shown in Figure 5-16a. However the colour changed once the electrodes were placed in the flame (Figure 5-16b, c, d) suggesting a material transformation may have occurred. A yellow coloured material was apparent in all three electrodes. The yellow coloured material at the front of the electrode progressively grew from Electrode 1 until it was consistently throughout Electrode 3. A darkish material was seen next to the yellow coloured material in Electrode 1 and Electrode 2; however this was not present in Electrode 3. In both Electrode 1 and Electrode 2, a small yellow coloured material was again present at the back of the electrode completing the electrode pellet.

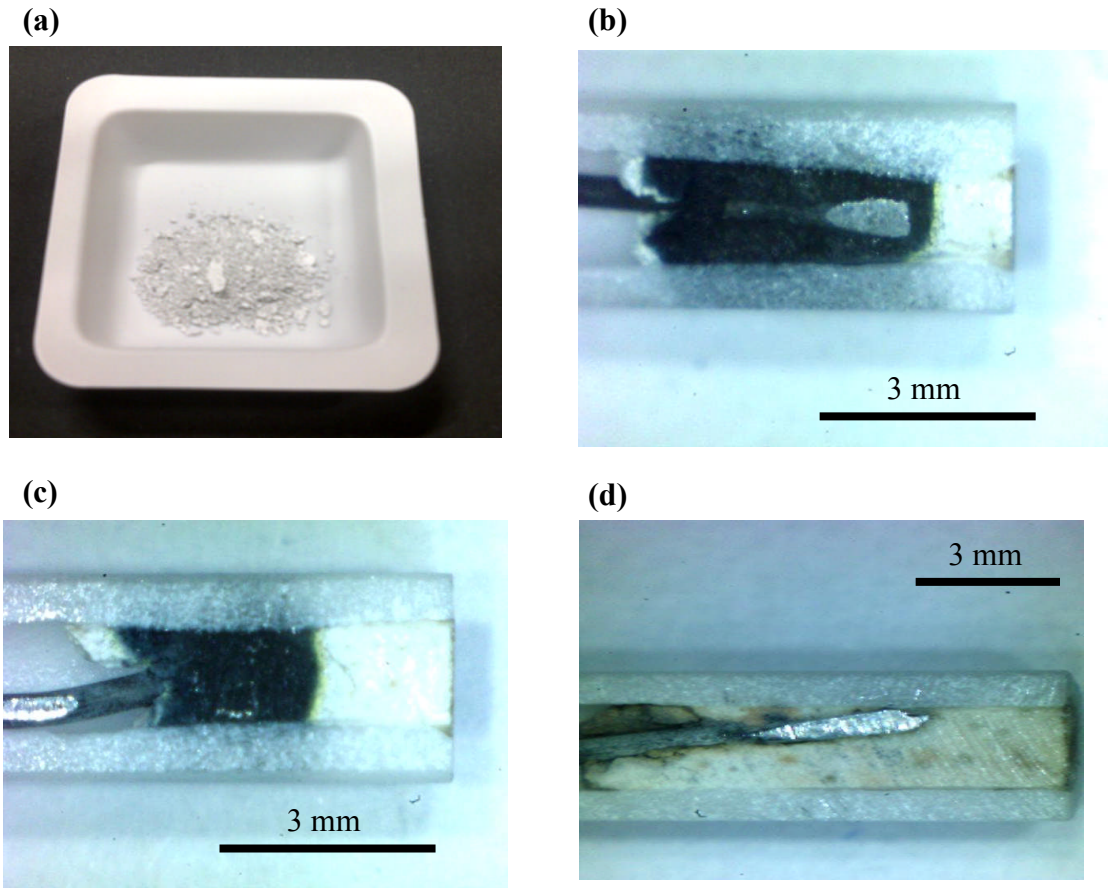

Figure 5-16: Images of 20/80 Ti/TiO_2: (a) reference material-pre paste, (b) Electrode 1 after a single scan (70 s), (c) Electrode 2 after three scans (210 s) and (d) Electrode 3 after ten scans (700 s).

A Raman spectroscopy line profile was collated along the length of each reference material. The resulting spectra for all three electrodes are shown in Figure 5-17.

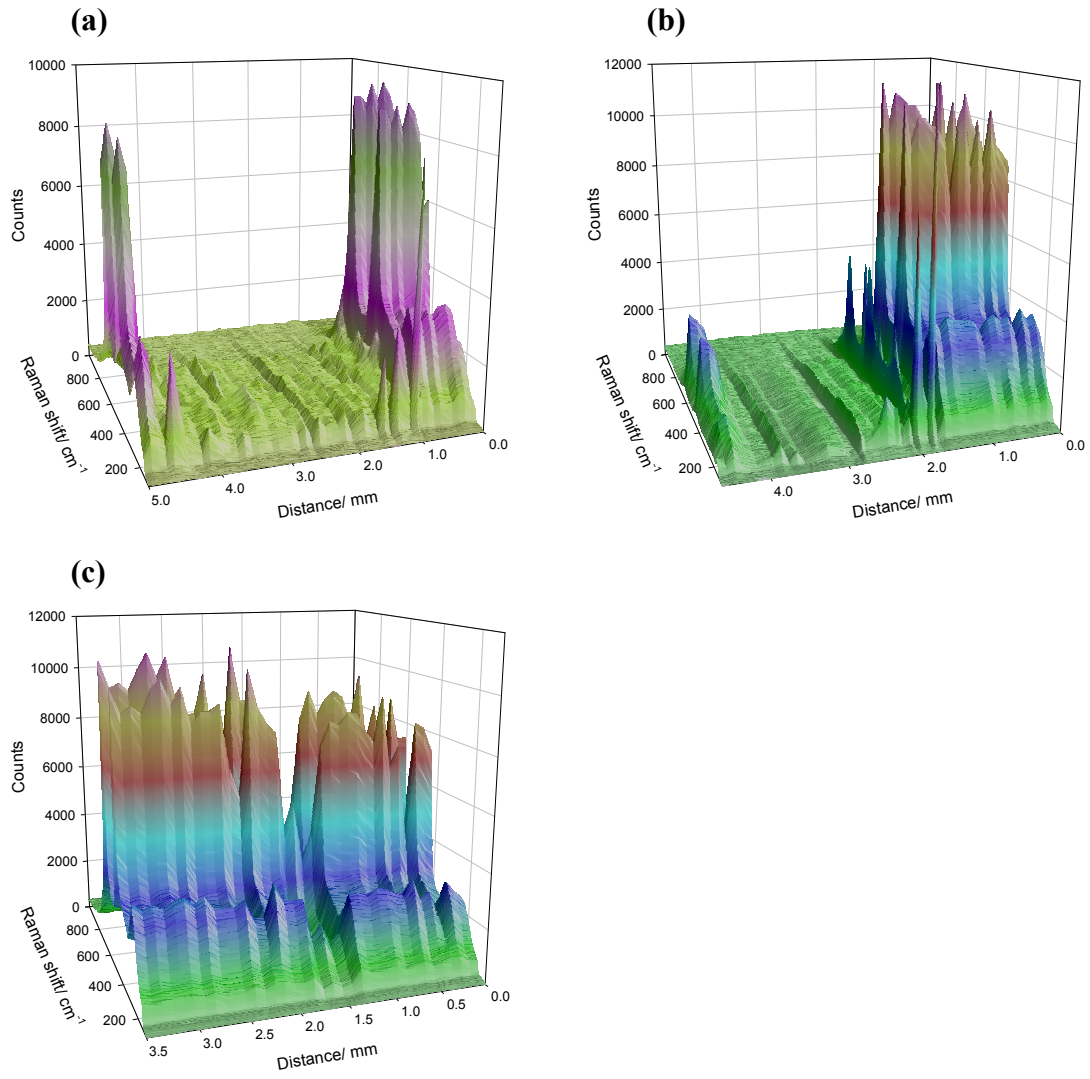

Figure 5-17: 3D Raman Spectroscopy line profile of 20/80 Ti/TiO_2 (a) Electrode 1, (b) Electrode 2, and (c) Electrode 3 taken from the front of the electrode through to the back of the pellet in 100 µm increments.

The yellow coloured material at the front (0.0 to 1.6 mm) of Electrode 1 (Figure 5-17a) was identified. The strong peaks positioned at 237, 448, and 611 cm^{-1} were confirmed to belong to TiO_2 – rutile phase.[95-98] The rutile phase progressively grew over time as seen in Electrode 2 (Figure 5-17b) and Electrode

3 (Figure 5-17c). The yellow coloured material formed at the back of the electrodes was also confirmed as rutile. However, Raman spectroscopy was not able to identify the darkish material in the middle of Electrode 1 and Electrode 2 due to the material having a weak Raman signal or being almost Raman insensitive.

Structural studies (phase identification) were performed by powder XRD techniques to identify the composition of all electrodes. The XRD patterns for all three electrodes are shown in Figure 5-18 and summarised in Table 5-4.

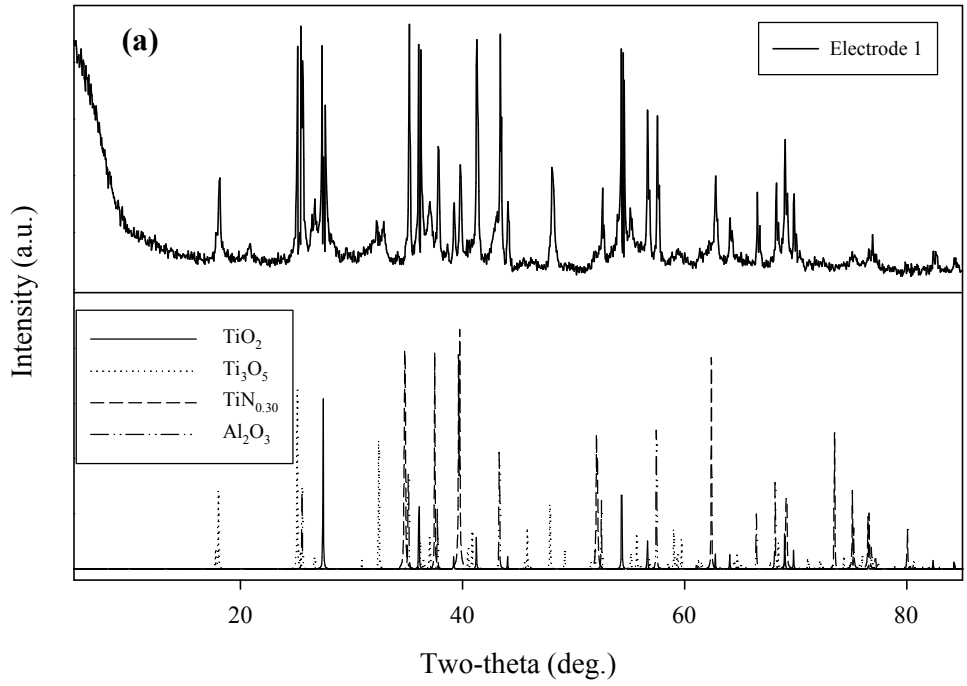

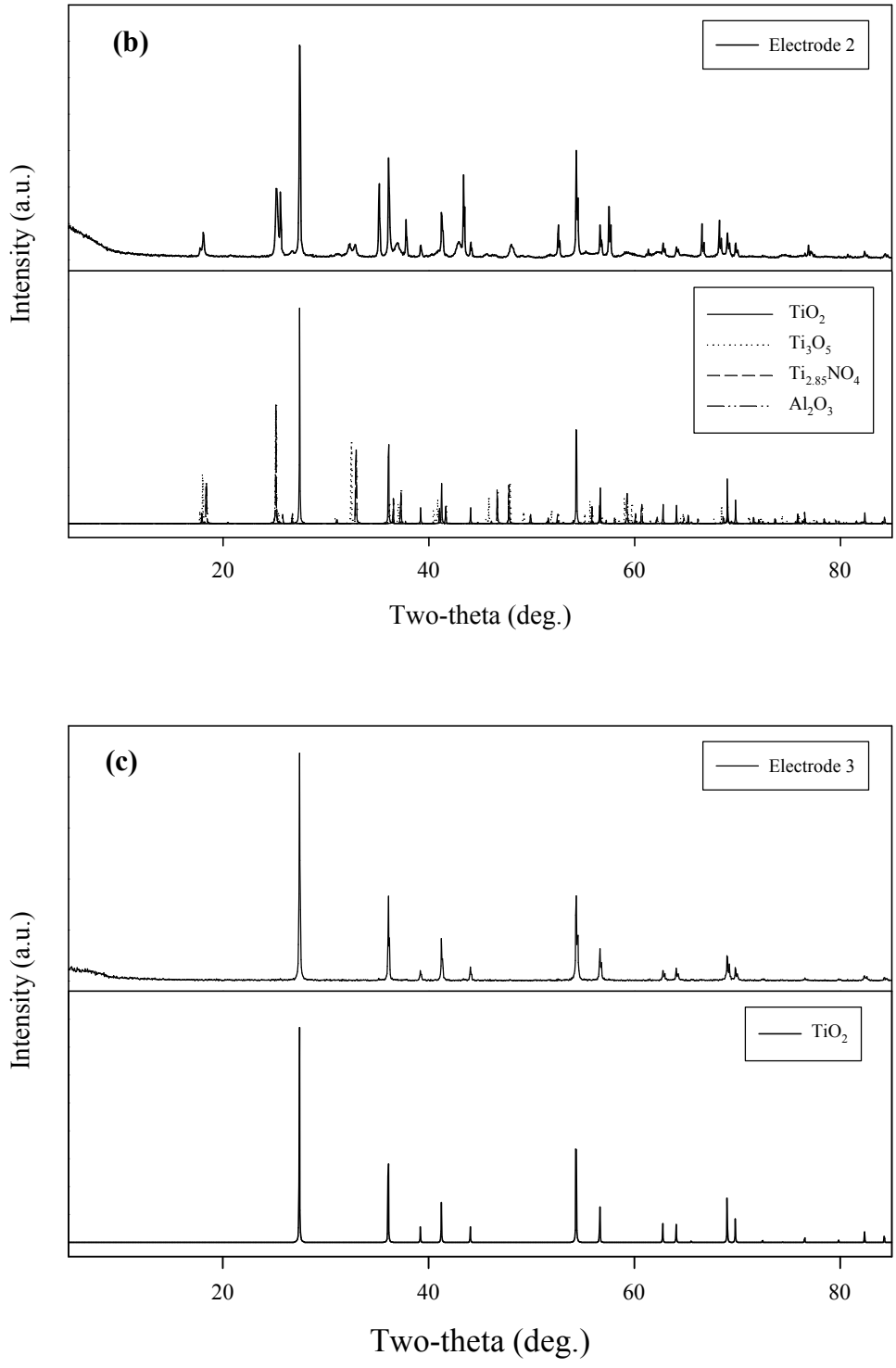

Figure 5-18: XRD pattern of 20/80 Ti/TiO_2 (a) Electrode 1, (b) Electrode 2, and (c) Electrode 3. The pattern for $TiN_{0.30}$ was compared to that from the PDF powder diffraction database (International Centre for Diffraction Data). All other peaks were compared to the standard patterns from the Inorganic Crystal Structure Database.

20/80 Ti/TiO_2					
Electrode	**TiO_2**	**Ti_3O_5**	**TiN**	**$TiN_{0.30}$**	**$Ti_{2.85}NO_4$**
1	✓	✓	–	✓	–
2	✓	✓	–	–	✓
3	✓	–	–	–	–

Table 5-4: Summary of the materials identified by XRD that were present in all 20/80 Ti/TiO_2 electrodes.

The XRD patterns for Electrode 1 and Electrode 2 suggest that both electrodes were made of several complex stoichiometric and non-stoichiometric phases. The pattern of Al_2O_3 (cc 160604)[99] arose due to small fragments of the ceramic tube holder being mixed with both electrode reference materials. Within Electrode 1, Ti_3O_5 (cc 50984)[100] and $TiN_{0.30}$ (cc 41-1352)[101] was found to be present. In addition to Ti_3O_5 being present in Electrode 2, $TiN_{0.34}O_{0.76}$ was found to have replaced $TiN_{0.30}$. (An XRD standard pattern for $TiN_{0.34}O_{0.76}$ was found using a DIFFRAC ^{Plus} EVA software program but could not be found in the Inorganic Crystal Structure Database). To ensure the peaks of the oxynitride were assigned, a $Ti_{2.85}NO_4$ standard (cc 173420)[102] was used because its XRD pattern closely resembled that of $TiN_{0.34}O_{0.76}$. As shown previously by Raman spectroscopy, XRD, and later confirmed by XPS, Electrode 3 contained 100% TiO_2 – rutile phase (cc 51935)[103].

The results obtained by XRD were further supported by XPS analysis. The Ti 2*p* spectra for both Electrode 1 and Electrode 3 are presented in Figure 5-19.

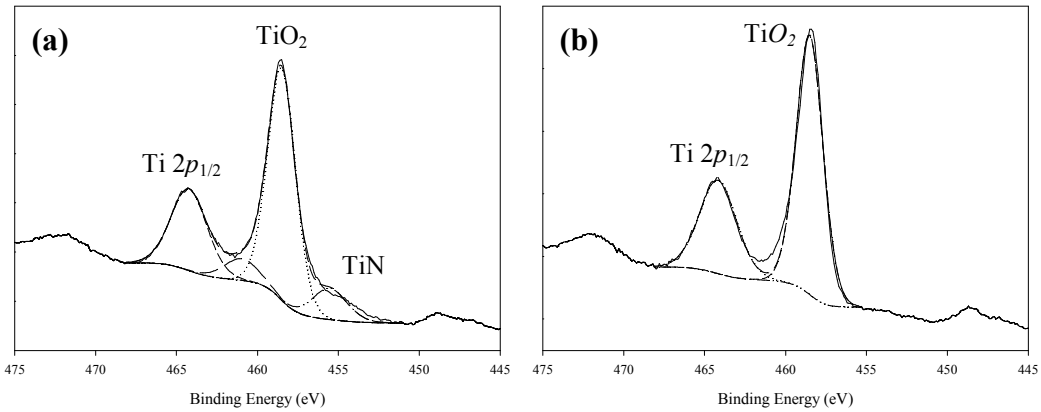

Figure 5-19: Fitted *Ti 2p* XPS spectra of 20/80 Ti/TiO_2 (a) Electrode 1 and (b) Electrode 3

The results shown in Figure 5-19a confirm that Electrode 1 contained only Ti bound to oxygen at peak position 458.5 eV and nitrogen at peak position 455.0 eV. The area of both peaks was calculated with 79.7% TiO_2 and 20.3% TiN found to be present in the electrode. In contrast, only Ti bound to oxygen was found in Electrode 3 (Figure 5-19b) observed at peak position 458 eV, confirming the sample was 100 % TiO_2.

The spectroscopic evidence presented above suggests that the dark coloured material in both Electrode 1 and Electrode 2 is predominantly Ti_3O_5 with the formation of a small amount of $TiN_{0.30}$. The formation of a nitride based material is highly likely since nitrogen gas was present in the combustion process. The location of the TiN may well be dispersed within the dark material or highly ordered specifically located at the interface between the rutile and Ti_3O_5 phase. The formation of Ti_3O_5 has been reported in the literature by several synthesis methods,[104-106] including the reduction of TiO_2 in hydrogen, in a carbothermal medium, and through the use of Ti in different oxygen partial pressure environments. The kinetically favourable Ti_3O_5 material that forms once (or soon after) the electrode enters the flame decreases over time and is accompanied by an increase in TiO_2, suggesting that Ti_3O_5 is oxidised to TiO_2 over time. With excess oxygen present within the environment, it is likely that the thermal oxidation of Ti_3O_5 may occur by diffusion and/or in-depth migration,[107] hence

the formation of rutile on both sides of the electrode pellet. The evidence collated from Electrode 2 suggests that $TiN_{0.30}$ was also oxidised to TiO_2 through an intermediate oxynitride ($TiN_{0.34}O_{0.76}$). The conversion or the formation of rutile over time is not surprising since rutile is the most thermodynamically stable of all Ti oxides.

Thermal analysis was performed on a freshly prepared 20/80 Ti/TiO_2 powder sample (not placed in the flame) under controlled thermal treatment (Figure 5-20).

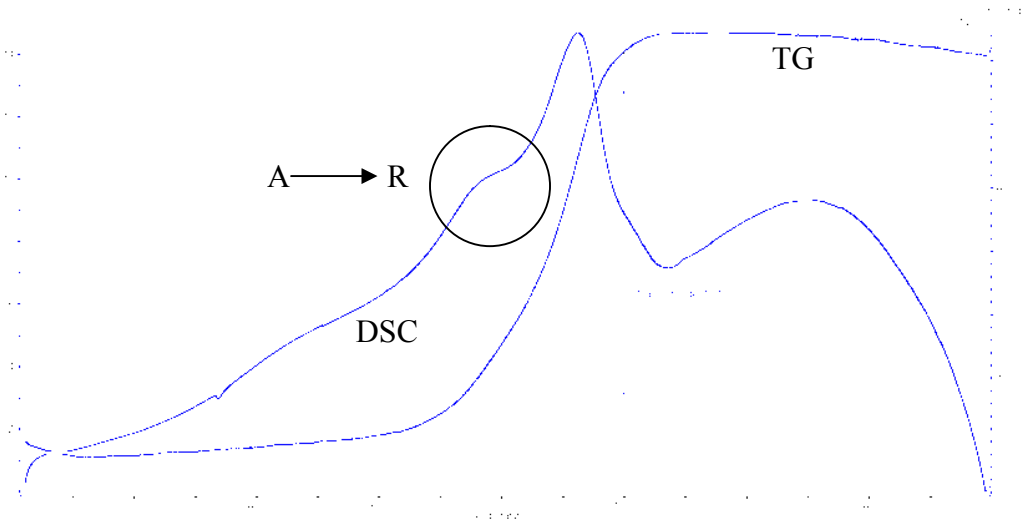

Figure 5-20: TA of a prepared 20/80 Ti/TiO_2 powder sample. The temperature was ramped from room temperature up to 1590 °C in air with a heating rate of 10 °C / min. The sample was held at this maximum temperature for 2 minutes and left to cool to room temperature spontaneously.

The DSC trace indicated multi phase processes occurred at a temperature onset ca. 700 °C. These processes are likely to include the transformation of anatase (raw form of TiO_2) to rutile shown by the small hump (circled) and also the oxidation of Ti to TiO_2, indicated by the 12.2 % mass increase shown in the TG trace. The mass change was in close agreement with the theoretical value, 13.4 %. The sample obtained after TA (light yellow in colour) was analysed by XRD

and identified as rutile, which is known to be thermodynamically favourable in air at high temperatures.

5.3.5.2 80/20 Ti/TiO_2

The initial pre-paste colour of 80/20 Ti/TiO_2 was dark grey as shown in Figure 5-21a. All three electrodes had the similar visual appearance after being placed in the flame (Figure 5-21b, c, d).

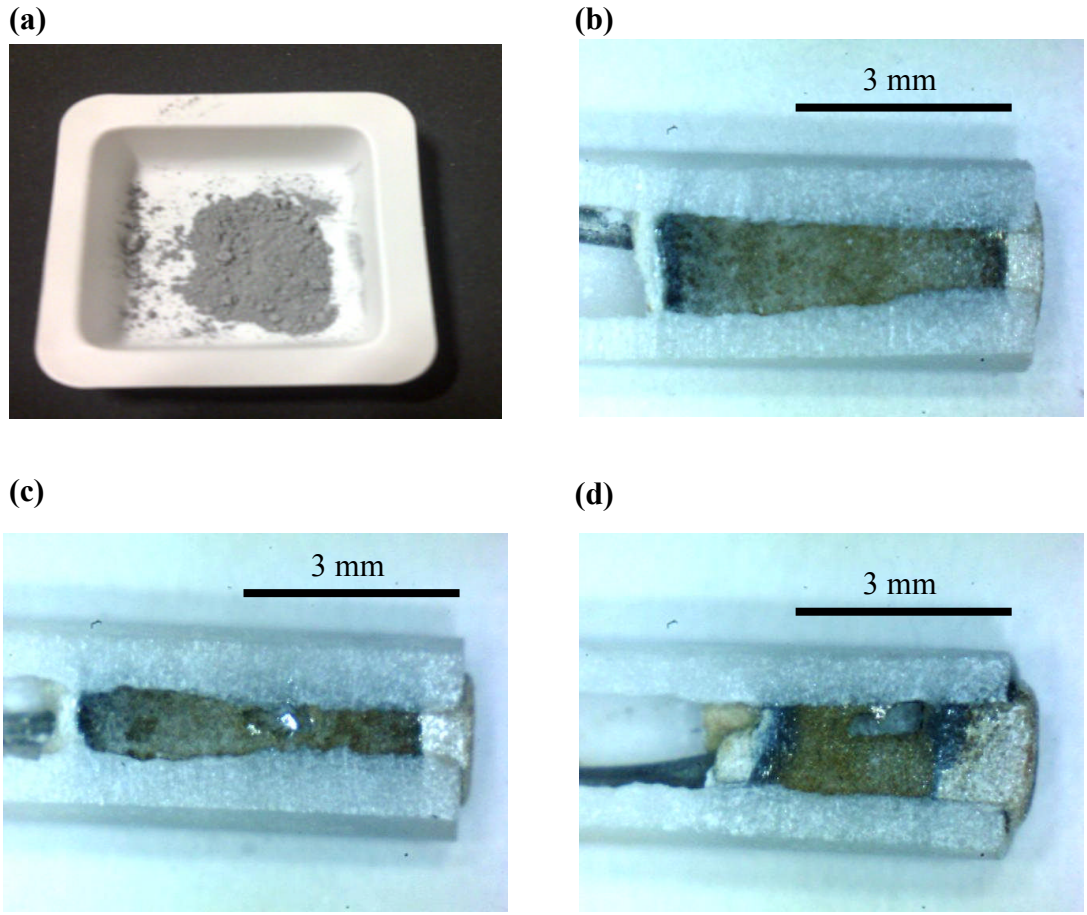

Figure 5-21: Images of 80/20 Ti/TiO_2: (a) reference material-pre paste, (b) Electrode 1 after a single scan (70 s), (c) Electrode 2 after three scans (210 s) and (d) Electrode 3 after ten scans (700 s).

As with the 20/80 Ti/TiO_2 electrodes, a yellow coloured material was observed at the front of the pellet which progressively grew over time. A yellow phase was also observed at the back of the electrodes. At either side of the yellow coloured material, a small dark area was observed which sandwiched a brown coloured material which was predominantly the bulk material of all three electrodes.

A Raman spectroscopy line profile was collated along the length of each reference material. The resulting spectra for all three electrodes are shown in Figure 5-22.

The Raman spectroscopy line profile revealed the formation of rutile at the front (0.0 to 0.9 mm) and 1 mm from the back of Electrode 1 (Figure 5-22a). A small amount of rutile was found in the middle part of Electrode 1. Rutile was also found to be present in Electrode 2 (Figure 5-22b) and Electrode 3 (Figure 5-22c); however the rutile layer at the front progressively grew over time. Raman spectroscopy was not able to identify the other materials present within the electrode.

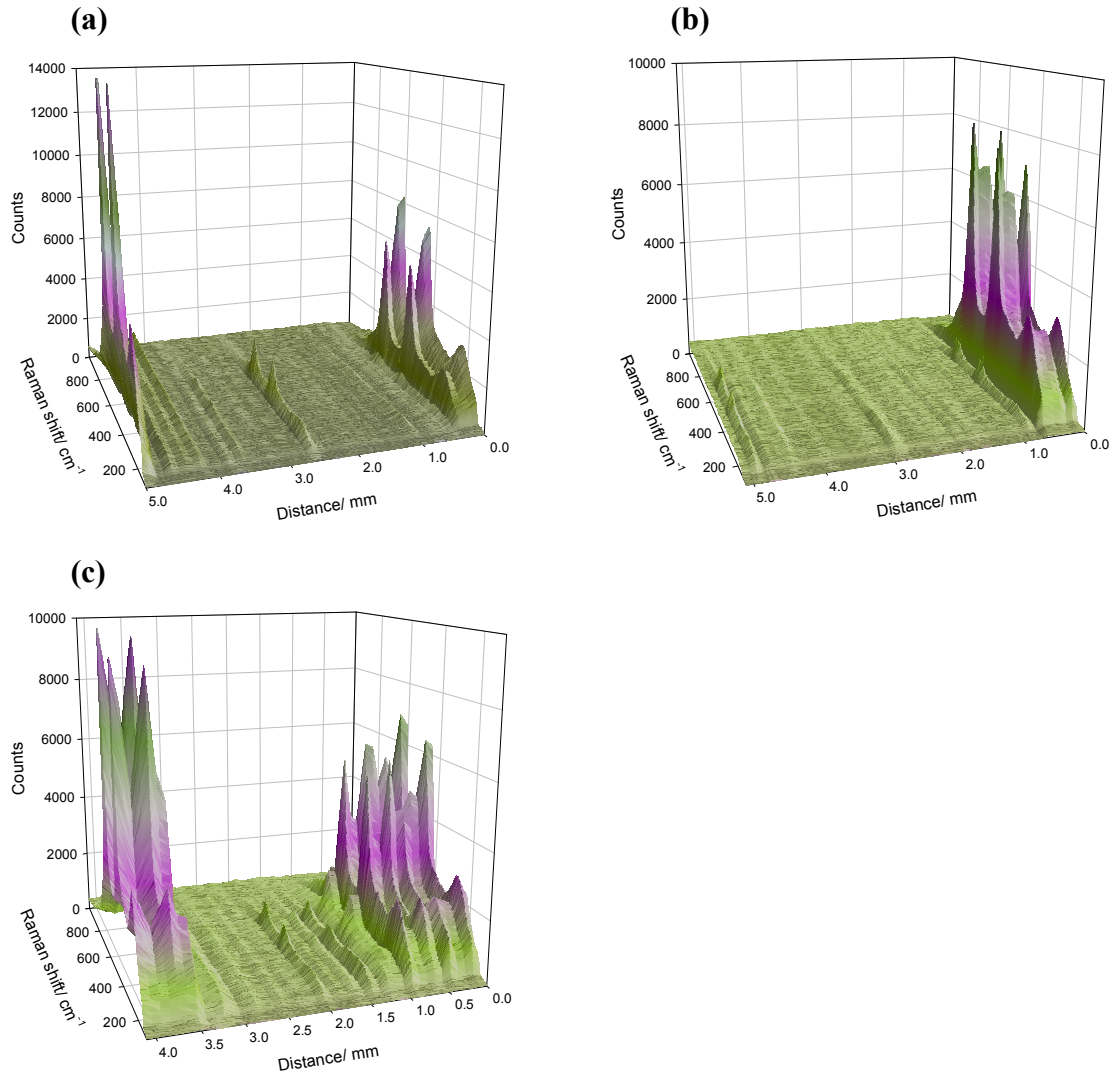

Figure 5-22: 3D Raman Spectroscopy line profile of 80/20 Ti/TiO_2 (a) Electrode 1, (b) Electrode 2, and (c) Electrode 3 taken from the front of the electrode through to the back of the pellet in 100 µm increments.

The XRD patterns of all three electrodes are shown in Figure 5-23 with the results summarised in Table 5-5. The pattern of Al_2O_3 (cc 160604)[99] arose due to small fragments of the ceramic tube holder being mixed with both electrode reference materials. XRD phase identification confirmed that all three electrodes contained TiO_2, rutile phase as shown by Raman spectroscopy. In addition, TiN (cc 604220)[108] and $TiN_{0.34}O_{0.76}$ was found to be present within Electrode 1 as

shown in Figure 5-23a. However, in Electrode 2 (Figure 5-23b) and Electrode 3 (Figure 5-23c), only TiN and $TiN_{0.30}$ was found to be present with rutile.

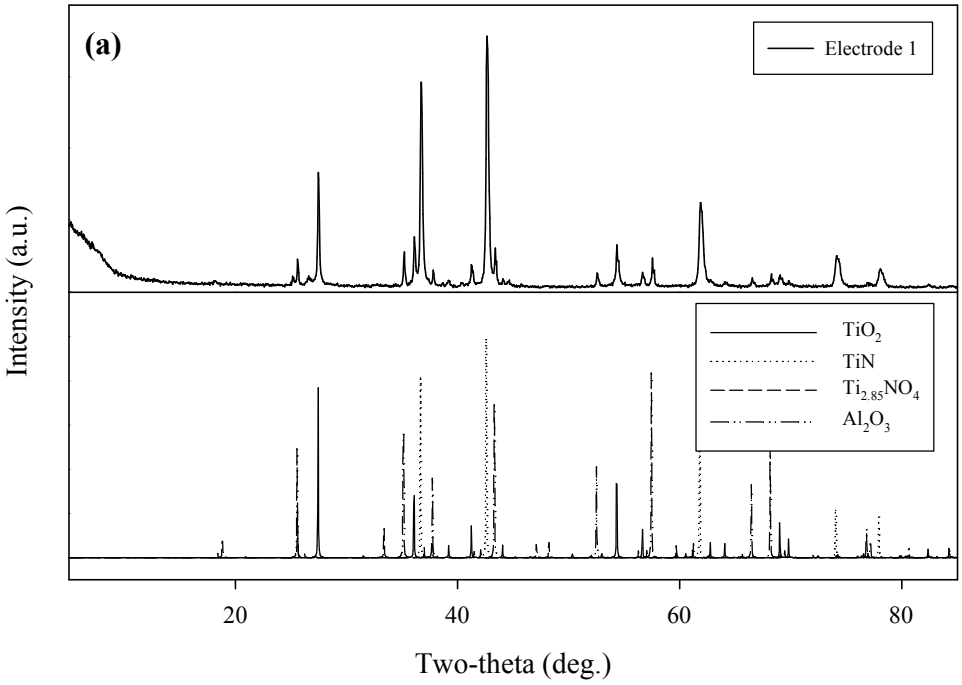

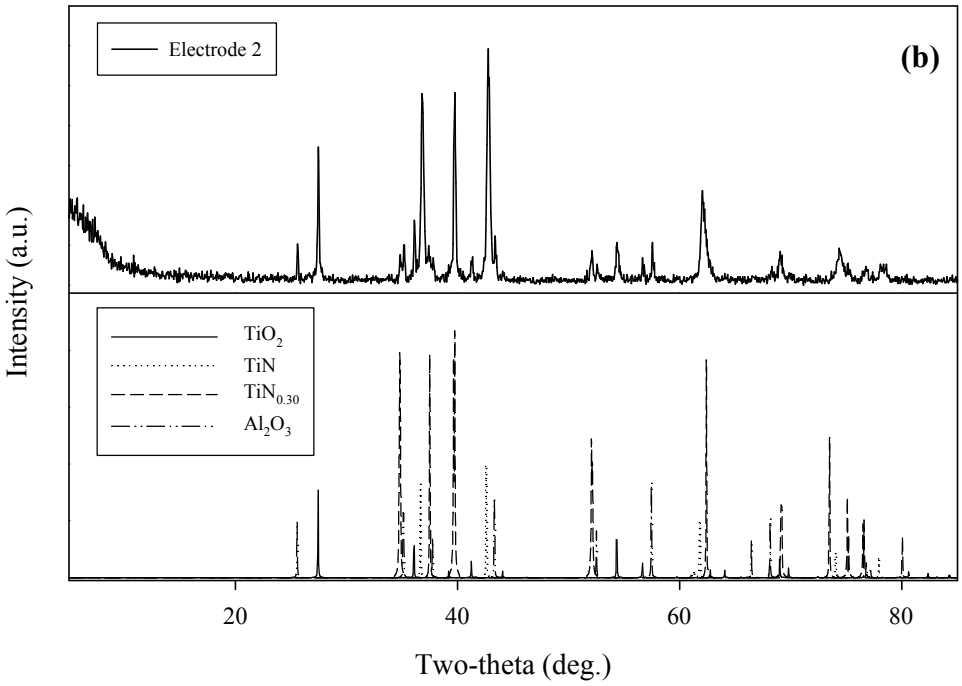

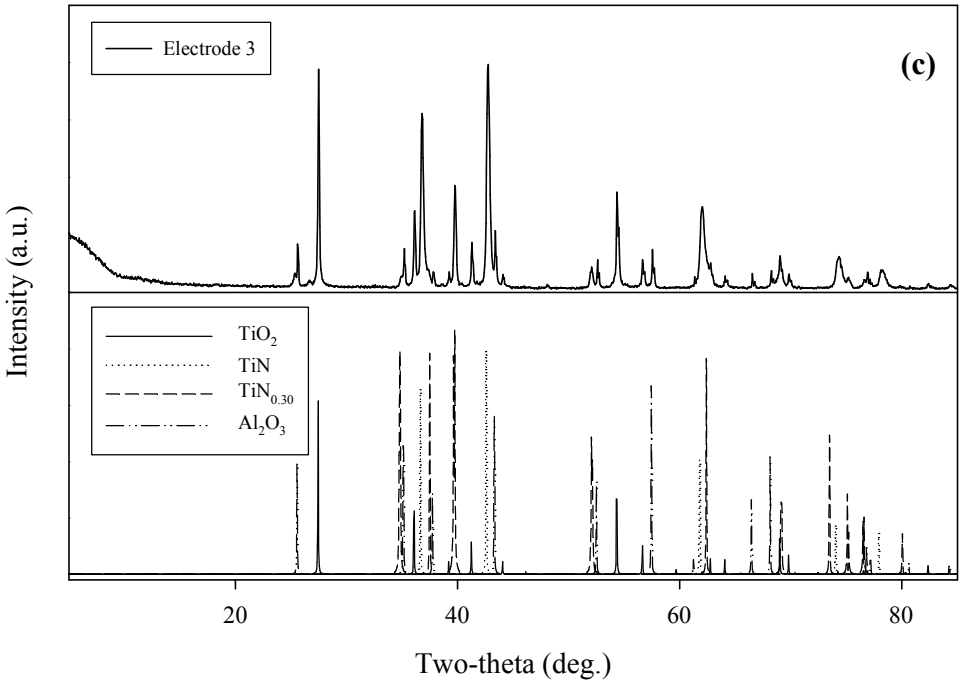

Figure 5-23: XRD pattern of 80/20 Ti/TiO_2 (a) Electrode 1, (b) Electrode 2, and (c) Electrode 3. The pattern for $TiN_{0.30}$ was compared to that from the PDF powder diffraction database (International Centre for Diffraction Data). All other peaks were compared to standards from the Inorganic Crystal Structure Database.

80/20 Ti/TiO_2					
Electrode	**TiO_2**	**Ti_3O_5**	**TiN**	**$TiN_{0.30}$**	**$Ti_{2.85}NO_4$**
1	✓	–	✓	–	✓
2	✓	–	✓	✓	–
3	✓	–	✓	✓	–

Table 5-5: Summary of the materials identified by XRD that were present in all 80/20 Ti/TiO_2 electrodes.

The results obtained by XRD were further supported by XPS analysis. The Ti 2*p* spectra for both Electrode 1 and Electrode 3 are presented in Figure 5-24.

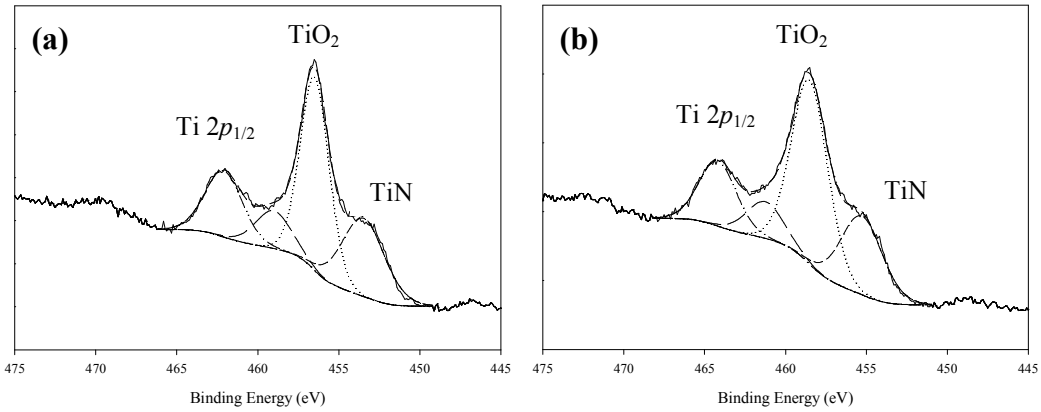

Figure 5-24: Fitted Ti 2*p* XPS spectra of 80/20 Ti/TiO_2 (a) Electrode 1 and (b) Electrode 3

The XPS analysis of Electrode 1 (Figure 5-24a) confirmed the presence of Ti bound to oxygen at peak position 456.5 eV and nitrogen at peak position 453.5 eV. The area of both peaks was calculated and 62.7 % TiO_2 and 37.3 % TiN was found to be present in the electrode. XPS also showed the presence of Ti bound to oxygen and nitrogen in Electrode 3 (Figure 5-24b) at the same peak positions. However, a smaller content of TiN (33.3 %) which resulted in a higher content of TiO_2 (66.7 %) was calculated.

The evidence presented here supports the formation of kinetically favourable TiN where a high concentration of Ti is present in nitrogen containing environment. Although Ti exhibits a large solubility for nitrogen at high temperatures, inward diffusion of nitrogen will occur from the flame towards the electrode to form a nitride layer at the surface as well as its dissolution in the bulk.[109;110] Lu has also reported results which show that although nitridation can occur alongside with oxidation, Ti nitridation occurs before oxidation, even in an oxygen-containing nitrogen atmosphere. The XRD results support evidence presented in the literature that suggests the formation of the meta-stable $TiN_{0.30}$ can co-exist in the bulk and on the surface;[101] however there are very few kinetic studies published on the oxidation of $TiN_{0.30}$.

Thermal analysis was performed on a freshly prepared 80/20 Ti/TiO_2 powder sample (not placed in the flame) under controlled thermal treatment (Figure 5-25).

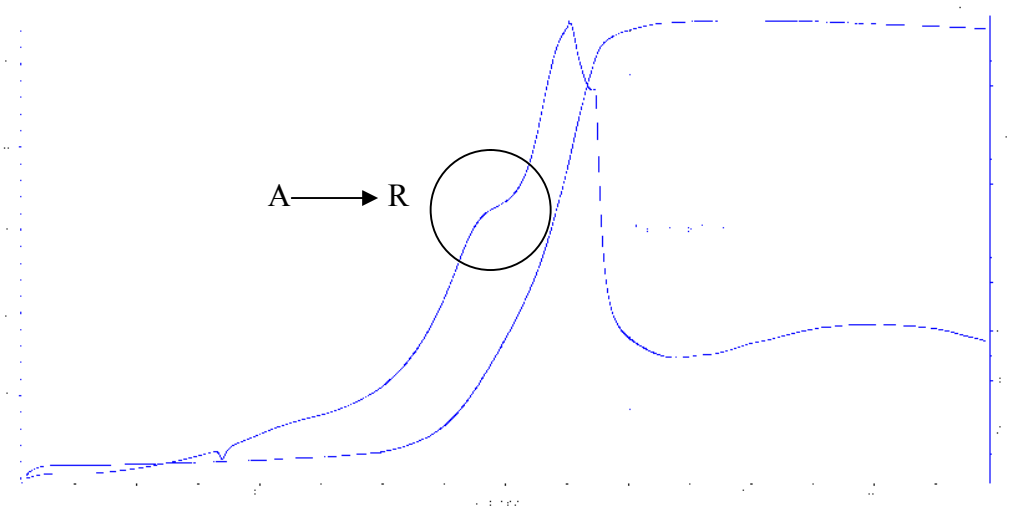

Figure 5-25: TA of a prepared 80/20 Ti/TiO_2 powder sample. The temperature was ramped from room temperature up to 1590 °C in air with a heating rate of 10 °C / min. The sample was held at this maximum temperature for 2 minutes and left to cool to room temperature spontaneously.

Although TiN is thermodynamically stable, thermodynamic data show that Ti oxides are much more stable than Ti nitrides concerning the Gibbs free energy of formation of both compounds.[111] This is supported by TA, which showed the similar thermal events as observed in the thermogram of the 20/80 Ti/TiO_2 sample. The increased mass of Ti present within the electrode compared with the 20/80 Ti/TiO_2 electrode caused the mass change to be larger (51.0 %). The mass change was in close agreement with the theoretical value (60.0%) for complete oxidation of Ti metal powder to TiO_2. The sample after TA was also analysed by XRD and confirmed that no other phases apart from rutile was present.

There have been plenty of reports demonstrating the formation of an oxide layer of rutile on the surface of TiN through the solid-gas reaction (Reaction 5-1):[112;113]

$$TiN + O_2 \rightarrow TiO_2 + \tfrac{1}{2}N_2$$

Reaction 5-1

There have been conflicting reports surrounding the mechanism of formation however it is very likely that this is governed by oxygen dissolution diffusing through the oxide cap. The rate of diffusion will depend on the microstructure and grain boundaries of that layer.[114;115] The oxide is likely to be porous with a lamellar structure allowing the rapid penetration of oxygen.[116] Some research indicates that the oxidation reaction proceeds at the TiN/TiO_2 interface, resulting in the formation of an oxynitride layer (sometimes called an 'intermediate') between the sharp oxide/nitride interface.[107] This is also supported by the evidence presented here. It is likely that the dark material shown in Figure 5-21 between the brown and yellow material is the intermediate, having an oxidation state between the oxide (Ti^{4+}) and the nitride (Ti^{3+}). With increasing oxidation time, the 'capping' oxide grows causing the bulk TiN and the intermediate layer to be farther from the surface.[114]

The electrochemical response of the electrodes in conjunction with its characterisation has provided sufficient evidence to suggest that the reference material in contact with the nichrome wire is responsible for the electrochemical responses observed. The gradual voltage drifting is believed to be due to the gradual structural and/or phase transformation of the reference material in the flame over time, in particular the wave of rutile formation from the front of the electrode until contact with the nichrome wire. This is clearly demonstrated with the electrode containing 20/80 Ti/TiO_2. The rapid formation and progression of rutile throughout the electrode and consequently the interaction of the oxide with the wire is thought to be associated with the sudden large voltage shift observed in the electrochemical response. The characteristic large voltage shift is thought to be linked to conductivity solely being dependent upon TiO_2 and no other Ti based material with other oxidation states. This is supported by the ex situ

characterisation evidence presented above. The electrode containing 80/20 Ti/TiO_2 does not experience the characteristic large voltage shift because the oxide growth is slow, therefore not fully interacting with the wire.

The images presented in Figure 5-16 showed that the reference material was exposed to a non-defined, albeit with a large surface area nichrome wire. The consequence of this was that as the oxide moved in an uniform fashion through the electrode, it came in contact with many interfaces along the wire. It is assumed that the undefined interface area of the wire with the reference material was responsible for the prolonged large voltage shift in the 20/80 Ti/TiO_2 reference electrode. The 0.5 mm diameter nichrome wire was replaced with a 1.4 mm diameter polished wire which ensured that only one defined interface was exposed, which the reference material could adhere to, as shown in Figure 5-26a. The use of the 1.4 mm diameter wire also prevented entrainment of air from the back of the ceramic tube. The electrochemical response using this electrode is shown in Figure 5-26b.

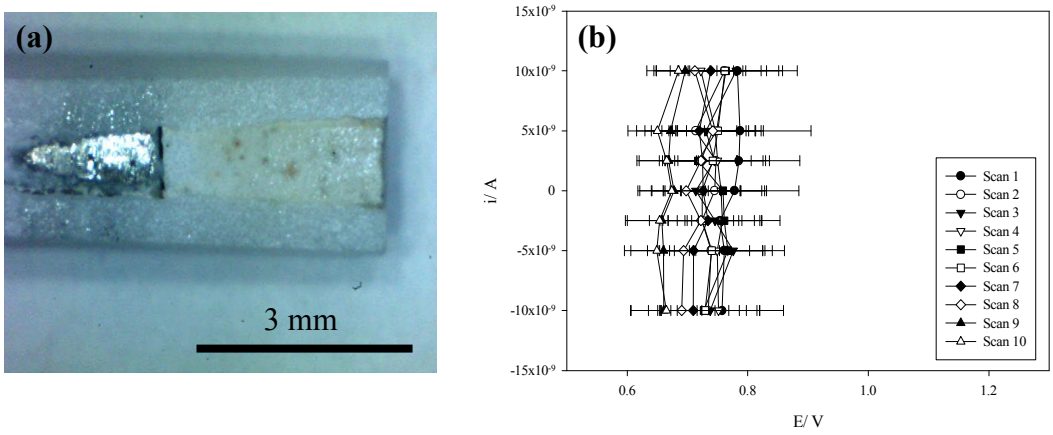

Figure 5-26: (a) Images of 20/80 Ti/TiO_2 Electrode 3 with 1.4 mm diameter nichrome wire, (b) corresponding I-V polarisability curve with step currents (10 s each) from 10 x 10^{-9} A to -10 x 10^{-9} A were passed through the electrode and voltage recorded.

The electrochemical response is similar to that using a 0.5 mm diameter wire, i.e. the voltage moves in a negative direction. The zero current voltage of each scan

using the 1.4 mm diameter wire is lower in comparison to the 0.5 mm diameter wire. This was attributed to no oxide forming at the back of the electrode (no oxygen entrainment) which contributed to the lower overall potential observed. Generally, the observed voltage changes was believed to correspond to the formation of the oxide layer at the front of the electrode moving in a uniform direction towards the defined interface of the wire. The advantage of the defined wire interface is apparent between scan 8 and scan 9 which resulted in a sharp and defined voltage shift. After the large shift, the potential does not continue to shift because all the material is rutile; hence a stable voltage is achieved.

The qualitative and quantitative identification of the materials has given an indication of the complex transformations that take place within the electrode which gives them the ability to become conducting. All electrodes contain different Ti based material(s) of different oxidation states which could have allowed reduction or oxidation of Ti to proceed. Fully oxidised stoichiometric TiO_2 was consistently present within all the electrodes, and is known to be a semiconductor.

Semiconductors, including TiO_2 and other non-stoichiometric Ti oxides such as Ti_3O_5, behave as an electrical insulator at room temperatures, however at elevated temperatures they possess conductive properties. The conductive properties are due mainly through the transportation of electronic charge carriers with a negligible amount of ionic conductivity contributing to the overall conductivity process.[117;118] Conduction occurs in semiconductors because the band gap within the material is small enough that a small increase in temperature promotes a sufficient number of electrons to move from the valence band to the conduction band.[119] The conductivity of rutile can be increased by reducing its band gap (3.0 eV).[120;121] It has been shown that the band gap can be reduced further by substitution with nitrogen doping for oxygen atoms, which is likely to occur in our system since excess nitrogen is present.[96;122]

At elevated temperatures there is an increased presence of intrinsic point defects in the structure of TiO_2.[123] From the aspect of ionic conductivity, two types of intrinsic defects are particularly important as they take direct part in conductivity. The first, known as Schottky disorder is formed when atoms or ions are displaced to the surface of the crystal as in the following scenario (Reaction 5-2):[124;125]

$$O^{2-} \leftrightarrow \frac{1}{2}O_2 + V_{\ddot{O}} + 2e^-$$

Reaction 5-2

Where $V_{\ddot{O}}$ is a doubly ionised oxygen vacancy. Rohnke et *al.* have studied the exchange rate of samples in different oxygen environments.[90] They reported up to 100 times higher exchange rate for samples immersed in an oxygen plasma compared to molecular oxygen environment. They have not given a firm explanation for their results but they believe the increase in exchange was due to the strong negative charging of the sample.

The second most common point defect is Frenkel disorder which involves displacing atoms from the lattice to interstitial sites as in the following reaction (Reaction 5-3):[125]

$$TiO_2 \leftrightarrow Ti^{4+} + O_2 + 4e^-$$

Reaction 5-3

These disorders lead to TiO_2 being described as an n-type semiconductor since both defects create an excess of negative electron charge carriers.[126]

Titanium nitride, also known as a semiconductor, has been shown to have interesting electrical properties with electrical conductivity similar to that of metal conductors. These nitrides acquire their properties through defect structures similar to that of TiO_2.

These materials, TiO_2, Ti_3O_5 and TiN are believed to be the major players in allowing all these electrodes to be conducting. As seen from the ex-situ characterisation, each electrode material undergoes phase transformations that occur over time. These phase changes, containing a number of Ti oxidation states is likely to have contributed to the potential observed.

5.4 Summary

The results presented here have shown that the electrode potential of both 20/80 Ti/TiO_2 and 80/20 Ti/TiO_2 compositions are determined by a set of complex material transformations. For simplicity, two separate and distinct phases have been ascribed to describe how the material influences the electrode potential. Phase I can be described as the transformation of the starting material, Ti and TiO_2 (anatase) into rutile through a host of intermediate reactions. The material change was accompanied by a gradual shift in the electrochemical response. Phase II began once all the electrode material was comprised of rutile. In this phase, the potential was dependent only upon oxygen ion conducting through the material. The result of this was a stable and consistent electrochemical response.

6 Development of Electrode Assembly for Dynamic Electrochemistry

6.1 Introduction

The choice of electrode material and the electrode arrangement within an electrochemical cell plays an important role when trying to record stable and reproducible cyclic voltammograms. Three electrodes are typically used when studying electron transfer reactions in electrochemical experiments, namely, working electrode (WE), reference electrode (RE) and counter electrode (CE).

The three previous chapters have explored three different types of REs. This chapter shall predominantly focus on the WE and CE. A discussion of the materials used for the WE and the CE shall be given, before describing in detail three assemblies, namely: 'Flag Cell', 'Cone Cell', and the 'Bucket Cell' that have been designed and developed. All three assemblies were held above the right hand side of the dual burner with the WE positioned at 10 mm above the burner top. The RE was placed in the left hand side of the dual flame, as close as possible to the WE but not directly underneath to ensure no cross contamination between flames and/or electrodes. These assemblies were designed and built to progressively overcome the complications that shall become apparent within this chapter.

6.2 Working Electrode Material

The WE is the electrode of interest, where redox chemistry can be controlled. A number of common materials are frequently used in the liquid phase; however the criteria for selecting a suitable WE material in a flame are different. A list of

the important factors affecting the selection of a good WE material are given below:

- **Ideally polarisable:** This refers to the electrode having a wide potential range where no electrode reactions can occur, which may affect the reaction of interest. Most noble metals and graphitic materials possess polarisable interfaces and therefore can be used as WEs.

- **High melting point:** The adiabatic temperature of the flame has been calculated as 2200 ºC. A material with a high melting point (>1800 ºC) would be desirable to prevent the material from changing state.

- **High thermal conductivity**: Thermal conductivity indicates the ability of a material to conduct heat. Due to the high temperatures experienced in the flame, a material that can transport heat efficiently and prevent heat build-up would be advantageous.

- **Chemically stable:** The chemical stability of the WE is important since this is the electrode where redox chemistry is to occur. The electrode should stay un-reactive, preventing electrode fouling.

- **Non-toxic:** Materials or its by-products that are toxic nature in natural or flame environments cannot be used as electrode material.

- **Non flammable:** Materials that are flammable in flame environments cannot be used as electrode material.

- **Easily modified:** The physical shape of the material should be easy to machine, modify and manipulate into different and useful geometries. In addition, the surface should be, without any difficulty, easy to clean following a measurement.

- **Cheap:** A material that is cheap in cost would be advantageous to such a project whereby many adjustments may be needed to be made.

Three potential candidates have been shortlisted, namely, platinum (Pt), boron doped diamond (BDD) and graphite. Platinum is frequently used in the liquid phase and has some very important physical properties which can be beneficial in the gas phase. Platinum has a thermal conductivity value of 71.6 W m^{-1} K^{-1} which is relatively good, however the melting temperature of Pt (1782 ºC) is close to the adiabatic temperature of the flame and therefore, if small diameter wires are used, they may melt once placed in the flame. It is likely that its high thermal conductivity ensures the transfer of thermal energy along the electrode efficiently preventing the temperature of Pt from exceeding its melting temperature. Platinum has been shown to readily absorb atoms when added to the flame. The absorption of metals will change the work function of the electrode and will form an amalgam type of electrode.[127] The expense factor of Pt must be taken into consideration. Platinum is an expensive material and would not be feasible to use as an electrode material since different designs would be needed to find the optimum electrode geometry and positioning.

Boron doped diamond has a higher thermal conductivity (approx. 2000 W m^{-1} K^{-1}) and higher melting point (1927 ºC) than Pt.[85] This would suggest that BDD would be a better electrode choice than Pt but other problematic issues still remain with BDD. Boron doped diamond is known to oxidise and subsequently etch slowly forming a rough surface in oxygen-containing environments at high temperatures. Boron doped diamond is a tough material and therefore routine machine work would be required to smooth or polish the electrode surface. The toughness of the material also limits the ability to shape or modify the electrode.

Graphite has a high melting temperature suitable for a flame environment (> 3000 ºC). Due to the soft nature of graphite, the physical shape can be easily machined, modified and/or manipulated into useful geometries. In addition, the

surface can easily be cleaned by coarse and/or fine sanding without extra machinery.

Graphite was deemed to satisfy the criteria given and was chosen to be the WE material. High purity (99.95 %) graphite rods (3 mm diameter) were purchased from Agar Scientific Ltd. These carbon rods were uncoated and absent of binders, providing both excellent chemical and physical compatibility in the flame.

6.3 Counter Electrode Material

The requirements for a CE material are less demanding compared to that of the WE because no reactions of interest occur on this electrode. The purpose of the CE is to supply the current required by the WE without in any way limiting the measured response of the electrochemical cell. The requirements of a good CE material are presented below:

- **Electrochemically inert:** The material should be chemically stable and remain electrically conducting in the flame.

- **Large surface area:** To ensure the CE does not impose any characteristics on the measured data, a large surface area compared to the WE should be used, central to the Langmuir probe technique

Two materials were chosen to act as the CE, namely Pt (99.95 %, supplied by Johnson Matthey Ltd, Cambridge) and mild steel containing 0.2 % carbon (purchased from Ravenace Metals Ltd).

6.4 Electrode assembly

The geometry and orientation of the three electrodes was seen as essential for performing electrochemistry in the flame. As previously mentioned, the surface area of the WE should be smaller than that of the CE. In order to achieve this and also define the surface area of the WE exposed to the flame, a number of options were available.

A non-conducting ceramic sleeve could have been used to cover and hold the WE, only exposing the tip of the electrode to the flame. This would allow for full control over the WE surface area exposed to the flame. Although this was a feasible option, certain disadvantages were noted with using ceramic materials at high temperatures. The difference in the thermal expansion coefficient between ceramic (approx. 8×10^{-6} °C^{-1}) and graphite (2.9×10^{-6} °C^{-1}) would lead to the ceramic expanding at a faster rate compare to the graphite electrode exposing a gap between both materials allowing the WE to fall out. A viable alternative to using a ceramic sleeve was to use the CE to define the WE surface area exposed to the flame. By making a hole in the CE and allowing the WE to slightly protrude, this would ensure only the surface tip of the WE experiences the flame. Three assemblies have been developed with the WE protruding through a hole made in the CE.

6.4.1 The Flag Cell

The Flag Cell assembly consisted of a 0.5 mm thick, square-shaped Pt flag (20 x 20 mm) acting as a CE. A 5 mm diameter hole was made in the centre of the flag to allow a 3 mm diameter graphite WE (40 mm length) to protrude through the gap by 1-2 mm (see Figure 6-1a). A 1 mm gap between the WE and CE was chosen to allow only the WE surface tip to be exposed to the flame. The gap size

was also necessary to ensure that there was no contact between both electrodes (see Figure 6-1b). An additional purpose of the flag was to deflect the flame in a uniformed manner away from other parts of the WE.

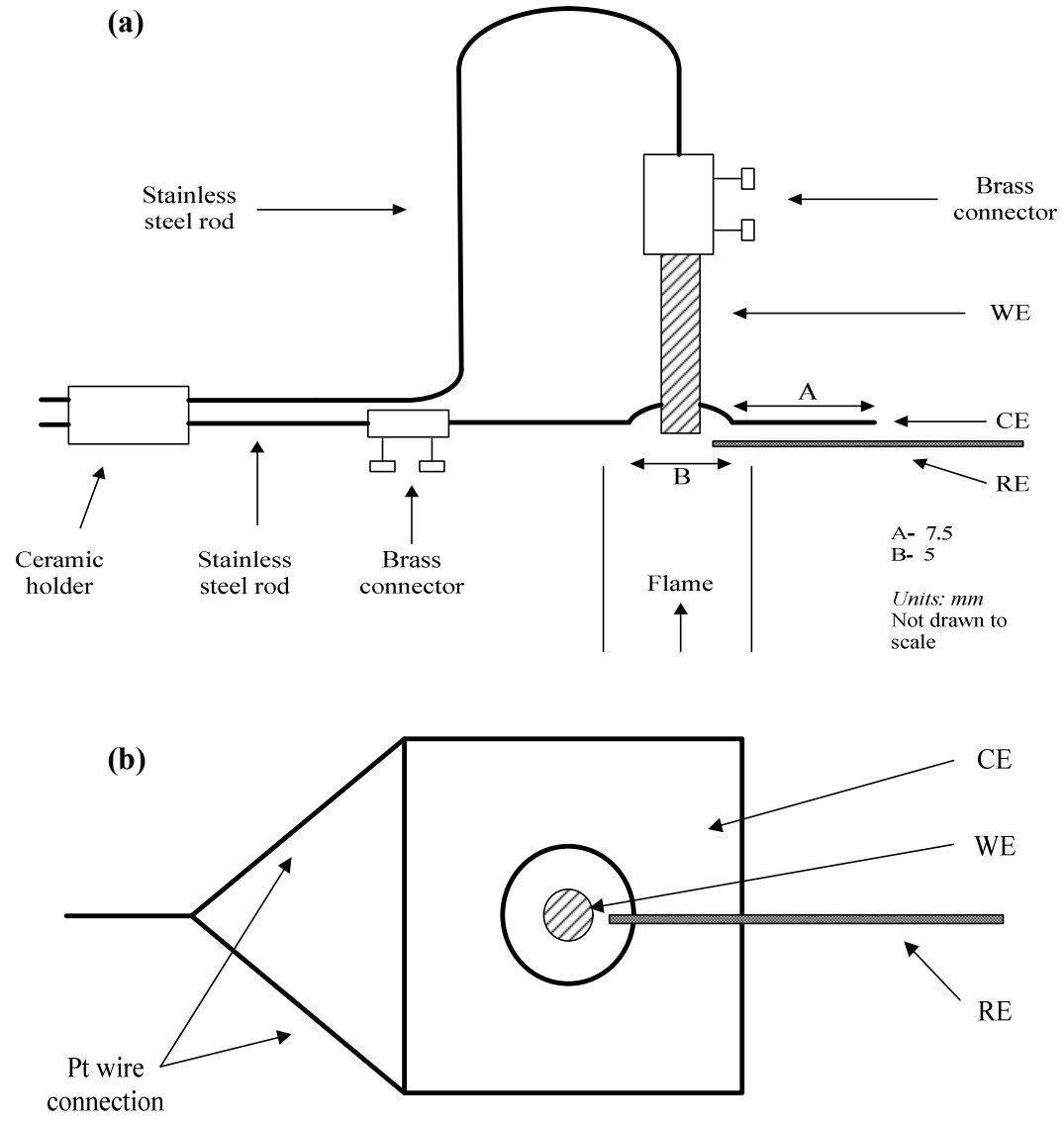

Figure 6-1: (a) Cross sectional view of the Flag Cell which shows the WE protruding through the hole in the CE. (b) End view of the Flag Cell illustrating the large gap between the WE and CE.

Two 40 mm length Pt wires (0.5 mm diameter) were spot welded to the sides of the flag and joined together to form one connection as shown in Figure 6-1b.

Both electrodes were secured using individual brass connectors, which were then both connected to stainless steel rods. A modified 'hook' shaped stainless steel rod was made for the WE to allow it to pass through the CE. Both stainless steel rods were fixed onto a single ceramic holder which was encased in a stainless steel box and securely fastened using screws and mounted onto a micropositioner. The electrical circuit was made complete by connecting the electrical leads to the correct stainless steel rods.

Electrochemical responses similar to the Langmuir probe were obtained using this assembly; however consistency was not observed. An in-depth observation of the set-up while in the flame highlighted some significant problems which may have contributed to the inconsistent responses. A major issue observed was the surface area of the WE exposed to in the flame. The gap between the WE and CE was deemed too large and as a consequence the flame was allowed to pass through the gap between the WE and the CE. This led not only to the tip, but also the sides of the WE experiencing the flame, which ultimately led to an increase in the surface area of the WE. In conjunction, the gap caused the flame to erode the sides of the electrode at a faster rate compared to the surface tip, as shown in Figure 6-2. This ageing process was seen as a by-product of having a large gap between both electrodes. To eliminate these unwanted processes, the distance between the WE and CE had to be reduced, to ensure only the surface tip of the WE experienced the flame.

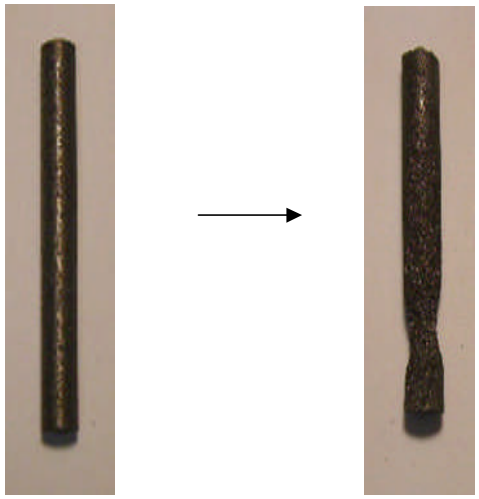

Figure 6-2: The pictures illustrate the 3 mm graphite WE before and after a flame experiment lasting 5 minutes. Although the aim of the Pt CE was to shield the sides of the WE from the flame, it is clearly visible that the flame erodes not only the tip but also the sides of the electrode.

Using the Pt flag as a CE meant that it was light in weight (3.5 g). This resulted in the upward force of the flame constantly agitating the CE. In order to minimise this problem, a more secure CE would be needed, either through a heavier CE or having the CE securely fixed into position. Lastly, to increase reproducibility and standardisation, it was deemed necessary that the electrodes be fixed together into one assembly. It was unlikely if the electrodes remained as separate entities that they could be placed at exact same location of the flame during each new experiment.

To summarise:

- Achievements:
    - Electrochemical response based on the Langmuir probe observed

- Challenges:
    - Observe reproducibility
        - Reduce gap between the WE and CE
        - Stop agitation of the CE in the flame
        - Fix electrodes into one entity

6.4.2 The Cone Cell

The rationale behind developing this cell was to overcome the problems addressed in the previous section with the Flag Cell. This cell consisted of a cone shaped CE made from 304 stainless steel (purchased from Ravenace Metals Ltd) with a 3 mm diameter gap for which the 40 mm length graphite WE (mechanically trimmed to 2.4 mm diameter) was allowed to pass through (see Figure 6-3a). The WE was allowed to protrude 1-2 mm from the end of the cone to ensure only the tip of the WE was exposed to the flame. As previously described in the Flag Cell section, the WE was held in placed using the same modified 'hook' holder and an electrical connection was made to the stainless steel rod. In contrast, an electrical connection for the CE was made directly onto the stainless steel rod as illustrated in Figure 6-3a. Both rods were securely held in place using the same ceramic holder, in similar fashion as described in the Flag Cell design.

The stainless steel cone was chosen to serve the same purpose as the Pt flag; but in addition, to also increase the mass of the CE (32.5 g) allowing the CE to become more stable against the force of the flame. The criteria for an effective CE is to be inert and have a large surface area, thus stainless steel was seen as an

ideal replacement for Pt, which for the mass that was needed would have been expensive to buy and modify.

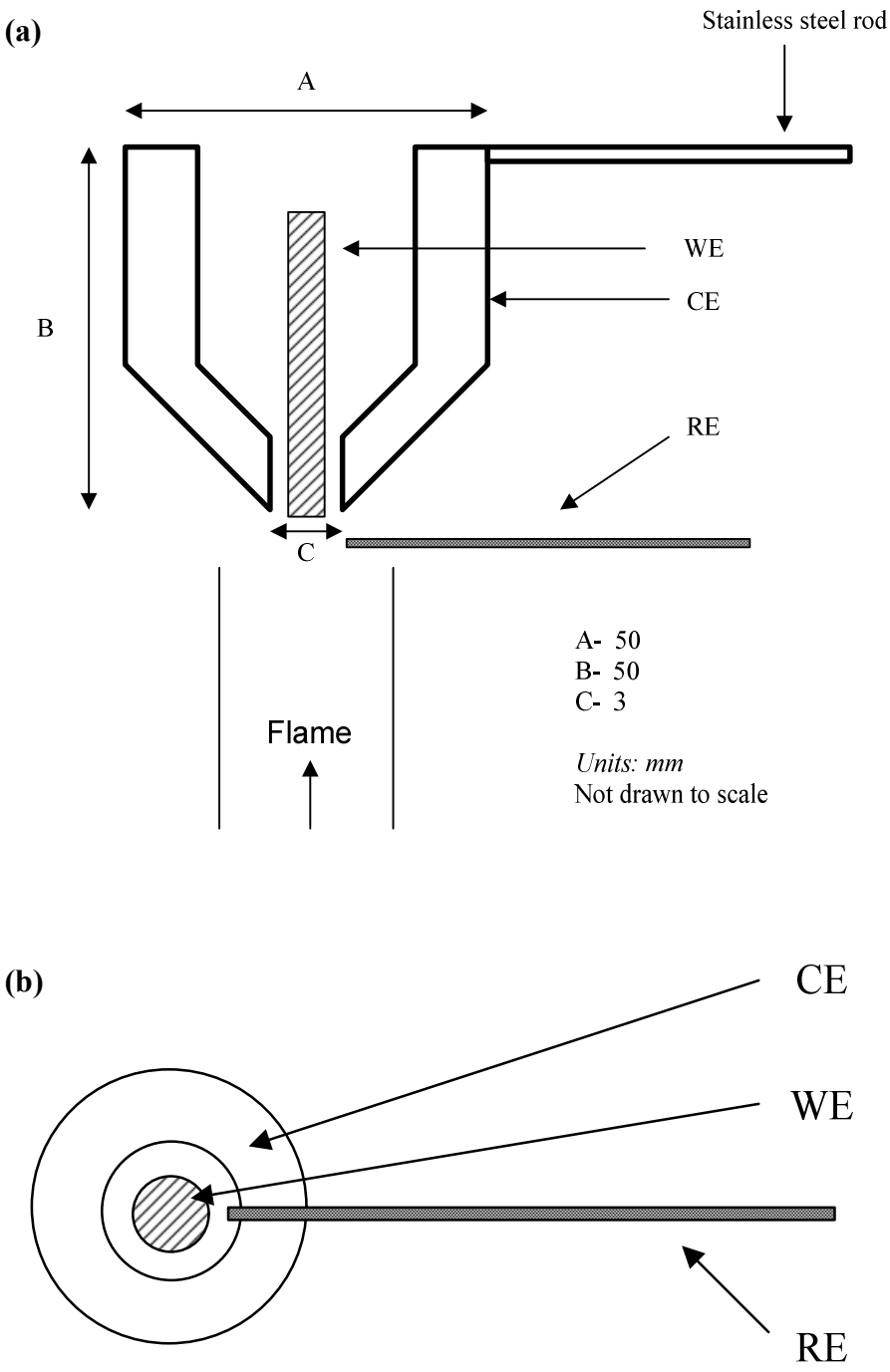

Figure 6-3: (a) Cross sectional view of the Cone Cell showing the WE tip protruding by 1-2 mm below the cone shaped CE. (b) End view of the Cone Cell illustrating the reduced gap (0.3 mm) between the WE and CE.

With the Cone Cell, the gap between the WE and the CE was reduced from 1 mm (observed in the Flag Cell) to 0.3 mm to prevent the flame from passing through the gap and ageing the sides of the WE, as shown in Figure 6-2. The distance was enough to significantly reduce the rate of erosion but not totally eradicate it. The close proximity of both the WE and CE ensured that the electrodes were always at the same location with respect to each other in the flame.

Although this design addressed the issues concerned with the Flag Cell, other unforeseen problems were identified. One such issue was the constant deflection of the flame towards the outer sides of the CE. Unlike Pt, stainless steel is more susceptible to oxidation. It was observed that particular areas (near the tip) of the cone were becoming increasingly oxidised after each experiment. The conductivity between these parts of the cone which were most in contact with the flame were measured to be approximately 50 kΩ, hence the cone was becoming highly resistive and therefore losing its ability to function as a good CE.

In addition to the oxidation of the CE, the procedure to manually align the WE through the hole in the CE was found to be problematic due to the 0.3 mm diameter distance separating both electrodes. This problem led to numerous occasions where both electrodes were in contact.

Both these problems had to be addressed before any reliable measurements were to be taken.

To summarise:

- Achievements:
    - Gap between WE and CE reduced
    - Large CE leading to stability in flame

- Challenges:
    - Further reduce gap between the WE and CE
    - Replace CE material due to oxidation
    - Fix electrodes securely into one entity

The Bucket Cell was designed the overcome the problems associated with the Cone Cell design.

6.4.3 The Bucket Cell

The Bucket Cell is the final electrochemical assembly design used in this work. The assembly incorporates a 2 mm thick Pt CE disc with a 3 mm diameter hole in the centre. As seen with the Cone Cell design, stainless steel (304) is susceptible to quick oxidation so a decision was taken to revert back to using Pt as the CE material. The Pt disc was embedded on a stainless steel support and securely fixed in place by a stainless steel ring as shown in Figure 6-4a and b.

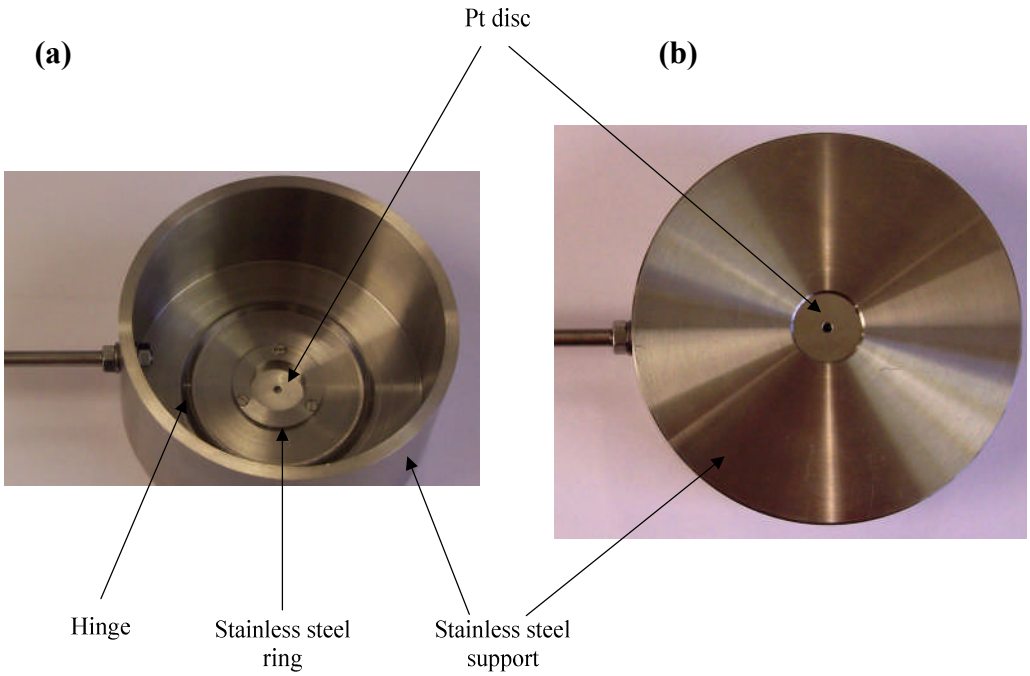

Figure 6-4: (a) Top view of Bucket Cell illustrating the Pt CE embedded into the stainless steel support and secured using the stainless steel ring. (b) Bottom view of the Bucket Cell with the 3 mm hole Pt CE supported by the stainless steel bucket.

A tough type of stainless steel known as stainless steel 316 (also purchased from Ravenace Metals Ltd) was used to prevent rapid oxidation in comparison to stainless steel 304 that was used in the Cone Cell. The bucket shape stainless steel was chosen to increase the mass of the set-up (greater stability from the force of the flame) and also to deflect away the flame in a uniform manner which would prevent possible contamination from the RE when placed nearby to the WE.

To ensure that only the smallest gap possible occurred between the WE and CE, a hole with a 3 mm diameter was chosen in the CE. The length of the WE was 50 mm, however, one side (15 mm) of the graphite electrode was incrementally (0.5 mm), mechanically trimmed from 3 mm until the optimum diameter was discovered. The optimum diameter was found to be 2.7 mm, where no conductivity between the WE and CE was measured outside the flame (see Figure 6-5).

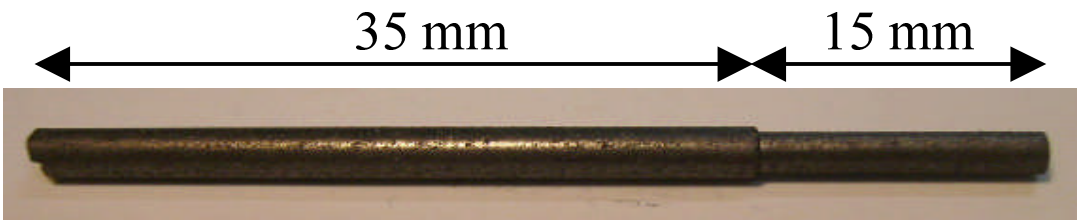

Figure 6-5: A picture showing the graphite WE used in the Bucket Cell. The total length of the WE was 50 mm. The bottom side of the electrode (15 mm) was mechanically machine from 3 mm to 2.7 mm to allow the electrode to fit through the Pt disc CE.

Using the Bucket Cell assembly, the gap between the WE and CE (0.15 mm) was reduced by half the distance compared to that seen in the Cone Cell.

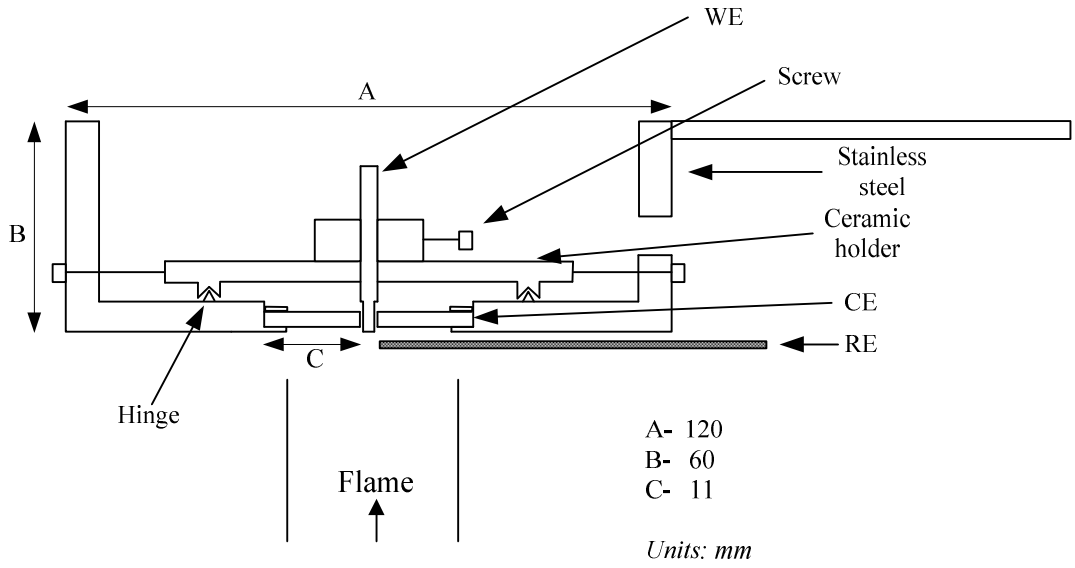

Figure 6-6: Cross sectional illustrating the Bucket Cell assembly which incorporates a Pt disc behaving as a CE stabilised by stainless steel support. The use of a ceramic holder and screws increased the precision between the WE and CE allowing a distance of 0.15 mm between both electrodes.

An advantage of having such a small gap between the WE and CE was the increased surface control of the WE. With this set-up, only the surface tip of the

WE (1-2 mm) was exposed to the flame. In the previous assemblies, the distance between the WE and CE was large enough to allow the flame to travel along the sides of the WE causing unwanted erosion of the WE.

In order to achieve this close proximity, a number of measures were taken. The set-up made use of a ceramic holder with a central hole. The diameter of the central hole was 3 mm (the same diameter as the top part of the WE) allowing the bottom part of the electrode to centrally protrude through the CE without any contact as shown in Figure 6-6.

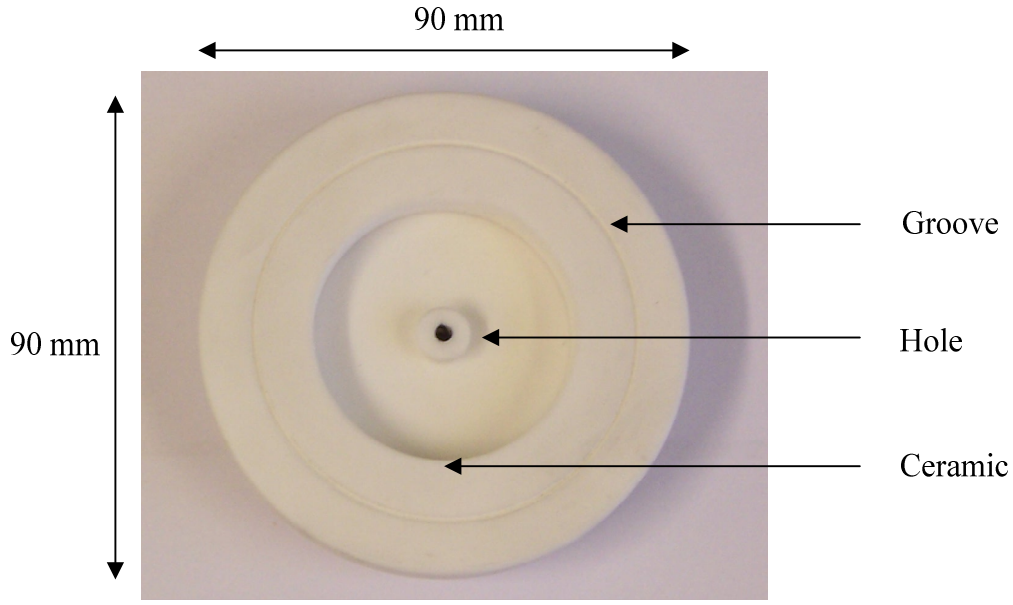

Figure 6-7: End view showing the underside ceramic support with a 3 mm that allows the WE to be stabilise and central while passing through the CE. The groove feature allows minimal heat transfer from the stainless steel support to the ceramic.

A hinge was etched into the stainless steel support with a complementary groove made into the ceramic holder as shown in Figure 6-7 to allow the ceramic holder to sit on the support. The purpose of making the hinge and groove was to minimise the extent of heat transfer from the stainless steel to the ceramic holder.

To further increase the precision in the WE and CE separation, 4 screws were inserted (equal distances apart) through the stainless steel cup into the ceramic holder. A single screw that went through the ceramic holder and made contact with the WE was used to secure the electrode in place, thus being able to further control the area of the electrode exposed to the flame. An added advantage of the single screw was to allow the WE and CE to become a fixed entity which led to the cell becoming easier to maintain and allowing the electrodes to be placed precisely back in the same location of the flame after renewing or cleaning the electrode surface(s).

A crocodile clip was used to make a direct electrical connection to the top part of the graphite WE. A sleeved 0.5 mm Pt wire was spot welded onto the inner side of the Pt disc, to which a crocodile clip was used to make an electrical connection from outside of the bucket.

Due to the large mass of the set-up, the stainless steel rod of the bucket had to be sandwiched between two ceramic plates, which were held in place using stainless blocks. These stainless steel blocks were then mounted and fixed onto the micropositioner. The micropositioners were fixed onto a load-bearing aluminium table. The fixing of the micropositioners onto the table was beneficial since the distance and location of the electrodes into the flame could be accurately measured and remain the same from experiment to experiment.

It was decided that the Bucket Cell was robust and adequately suitable for use in the flame to conduct cyclic voltammetry experiments, as will be explore in the next chapter.

7 Dynamic Electrochemistry

7.1 Introduction

The motivation to further explore flame chemistry using cyclic voltammetry stemmed from unpublished work conducted by Hadzifejzovic *et al*. A single cyclic voltammogram (Figure 7-1) had been achieved using the Flag Cell assembly described in Section 6.4.1.

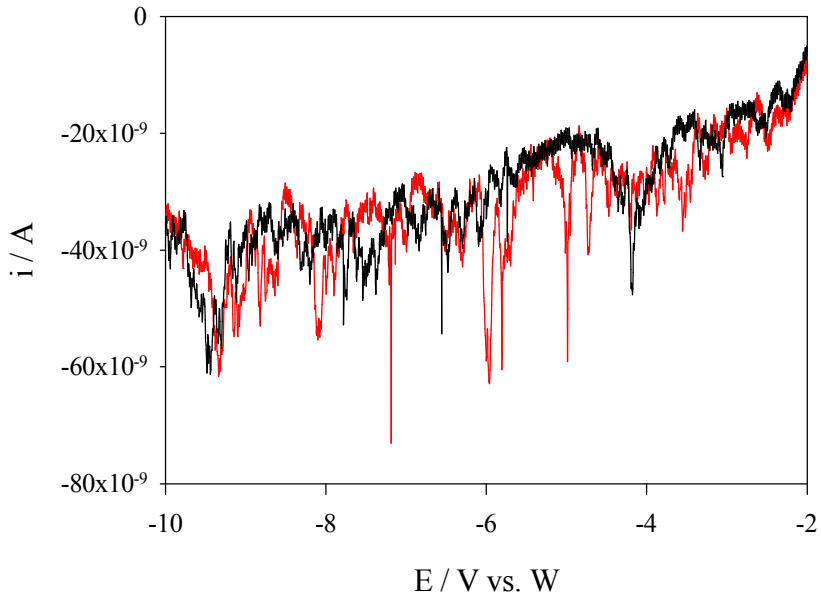

Figure 7-1: A cyclic voltammogram *(forward trace-red and backward trace-black)*, using the Flag Cell with a 3 mm diameter boron doped diamond working electrode and a 50 mm length tungsten wire RE which was placed in a bare flame. Scan rate 1 V s^{-1}. Voltage swept from 0 to -10 V.

The cyclic voltammogram showed a series of distinctive features which were observed both in the forward and backward traces. However, due to inadequate

electrode assembly and poor reference electrode (RE) stability, the replication of this voltammogram has been a major issue of concern.

The work described in this chapter shall explore the ability to obtain successive, stable cyclic voltammograms in a bare flame medium with different REs. The introduction of additives into the flame will provide further evidence that stable cyclic voltammograms can be achieved. In addition, cyclic voltammograms obtained by introducing additives into the flame will be shown to have distinctive features which can be used to characterise each additive.

7.2 Experimental

The Bucket Cell described in Section 6.4.3 with a 3 mm diameter graphite rod (purchased from Agar) was the electrochemical assembly used to conduct all cyclic voltammetry experiments presented in this chapter. The REs developed and described in Chapters 3, 4 and 5 were individually used to complete the electrochemical circuit. The cyclic voltammograms obtained were used as an indication of the RE suitability and practicality.

Two contrasting flames were used in this investigation, a single flame containing no additives (bare flame) and a dual flame. The LHS of the dual flame was bare while additives were introduced into the RHS flame (doped flame). Two metal salt clusters were used as additives (purchased from Sigma Aldrich), namely ammonium molybdate tetrahydrate $((NH_4)_6Mo_7O_{24} \cdot 4H_2O)$ and ammonium metatungstate hydrate $((NH_4)_6H_2W_{12}O_{40} \cdot xH_2O)$. These clusters were chosen due to their high solubility in water and are also routinely used as standards for inductively coupled plasma and atomic absorption spectroscopy.

Refer to Chapter 2 for further details regarding experimental procedures.

7.3 Results and Discussion

7.3.1 Bare flame using different reference electrodes

Sacrificial tungsten metal wire reference electrode

A sacrificial tungsten (W) metal wire, described in Chapter 3, was used as a RE and a series of cyclic voltammograms were collected (Figure 7-2).

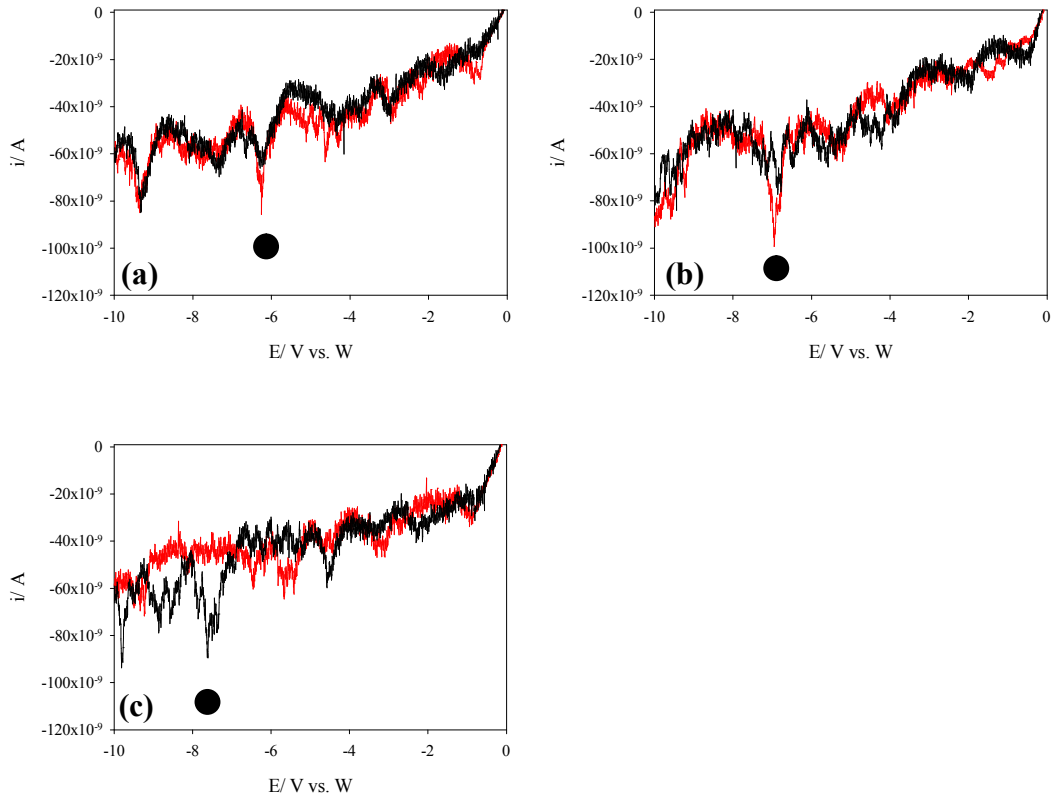

Figure 7-2: A series of successive cyclic voltammograms. (a) 1st scan, (b) 2nd scan, (c) 3rd scan *(forward trace-red and backward trace-black)*, using the Bucket Cell with a 50 mm length W metal wire RE which was placed in a bare flame. Scan rate 1 V s^{-1}. Voltage swept from 0 to -10 V.

The forward trace of the 1st scan (Figure 7-2a) showed a number of peaks positioned at specific voltage points which were also repeated on the backward trace. This scan is very comparable to that obtained by Hadzifejzovic *et al*. shown in Figure 7-1 with peaks observed *ca*. -4 V and -9.5 V. All the peaks observed were negative with no positive peaks. Negative peaks were also apparent in the 2nd scan (Figure 7-2b) and occurred at the same voltage point on both the forward and backward traces. However, the peaks in both the 1st and 2nd scans were not positioned at the same voltage points, possibly due to voltage shifting of the RE. This was demonstrated with the well-defined and dominant peak (black spot) which moved towards a more negative voltage point between scans. The size of this peak seen during the 1st and 2nd scans began to reduce during the 3rd scan (Figure 7-2c) with only the peak on the backward trace still visible. In consistent fashion with the previous two scans, the peak did continue to shift to a more negative voltage point. All three scans have shown poor voltage stability of the RE demonstrated through continuous drifting, which has led to irreproducible cyclic voltammograms.

The peaks observed in the cyclic voltammograms had not been expected as a bare flame was used. Chapter 3 has described the sacrificial nature of W wire once placed into a flame forming a gaseous sheath containing W species. These gaseous species were likely to have been responsible for the negative peaks seen in the cyclic voltammograms.

In situ Raman spectroscopy was used to confirm that tungsten trioxide (WO_3) was adsorbed on the surface of the working electrode (WE) during an electrochemical measurement (Figure 7-3).

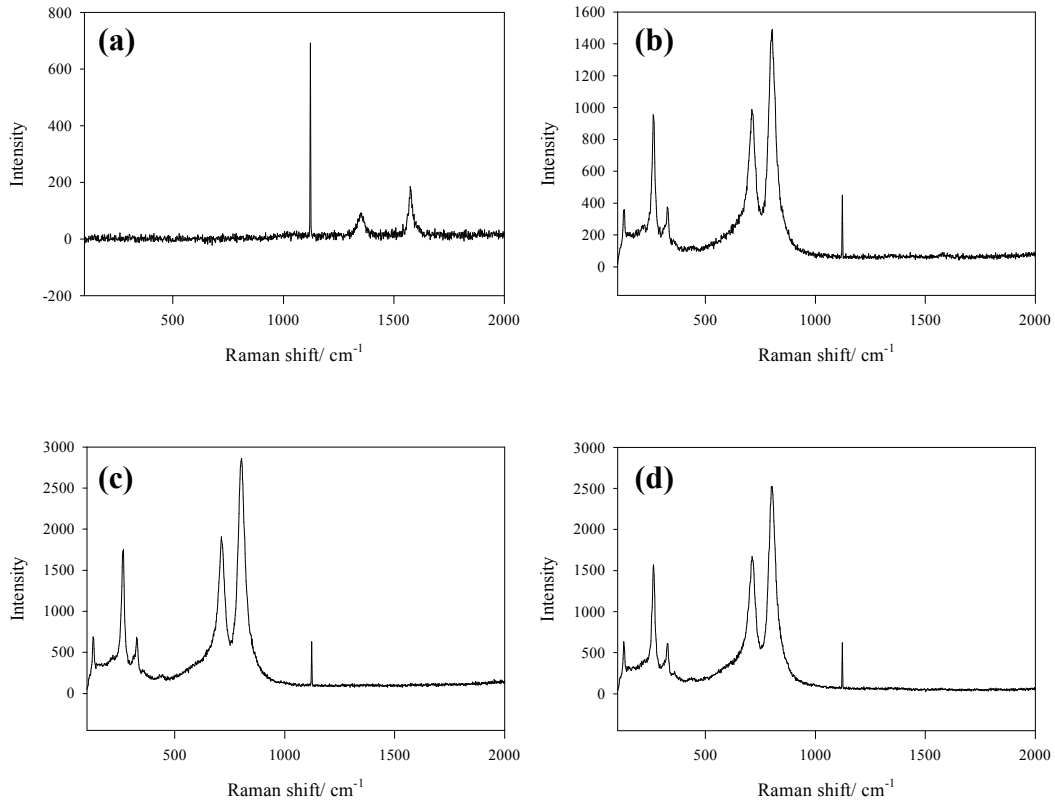

Figure 7-3: *In situ* Raman spectra of graphite rod placed in a bare flame. (a) no W wire in flame, (b) W wire placed and kept in flame for 10 s, (c) W wire kept in the flame for 20 s, and (d) W wire taken out of the flame after being kept in the flame for 20 s and graphite electrode left in flame for a further 120 s.

The spectrum shown in Figure 7-3a indicates that the graphite electrode exhibits a first order graphite peak at 1574 cm^{-1} and an additional peak at 1351 cm^{-1}. After the W wire was placed into the flame for 10 s, the Raman spectrum exhibited not only a lower intensity of the characteristic peaks of graphite but also an increase in the characteristic peaks of WO_3 (Figure 7-3b), consistent with the adsorption of the thermally-stable oxide onto an electrode surface.[128;129] Figure 7-3c shows a spectrum that was collected after 20 s (the time taken to complete one cyclic voltammogram) which indicated that the adsorption process had continued. The intensity of the peaks corresponding to graphite continued to decrease which was accompanied by a rise in the peak intensity associated with WO_3. It is interesting to note that the adsorption process is irreversible since the

intensity of the oxide did not reduce once the W wire was taken out of the flame as shown in Figure 7-3d.

Dynamic tungsten reference electrode

The dynamic RE (as described in Chapter 4) was incorporated into the 3 electrode assembly and a series of cyclic voltammograms were collected. The responses are shown in Figure 7-4.

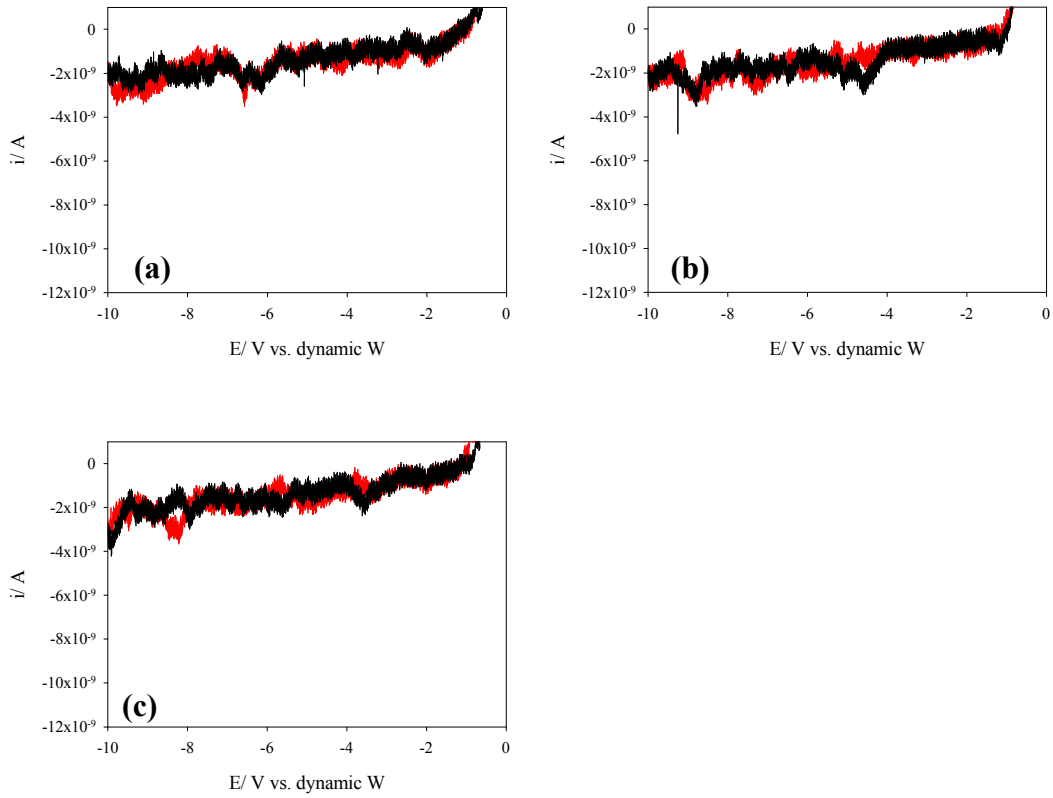

Figure 7-4: A series of successive cyclic voltammograms. (a) 1st scan, (b) 2nd scan, (c) 3rd scan *(forward trace-red and backward trace-black)*, using the Bucket Cell with a dynamic W RE (biased +ve with respect to a Pt coil with 0 V applied). Refer to Figure 7-2 caption for details regarding experimental conditions.

The responses in Figure 7-4 have similarities with those recorded when a *W* wire RE was used. In each scan, negative peaks on both the forward and backward traces were observed which occurred at the same voltage position.

However, the peaks were not consistently positioned at the same voltage points throughout the series of three scans, thus reproducibility was not observed. In contrast to the results obtained with the W wire RE, the magnitude of the current was drastically lower which is indicative of a decrease of gaseous W species reaching the WE. This was confirmed through *in situ* Raman spectroscopy which showed a reduction of WO_3 on the surface of the WE.

Titanium/titanium dioxide reference electrode

A titanium/titanium dioxide (Ti/TiO_2) paste packed into a ceramic support (as described in Chapter 5) was used as a RE and incorporated into the 3 electrode assembly. A series of cyclic voltammograms were performed with the results shown in Figure 7-5. The results presented in Figure 7-5 are similar to those observed with using the dynamic W RE except little or no features (negative peaks) were observed. The absence of these features and reduced current generated (compared with using a W wire RE) suggests the flame is indeed bare, containing no reference material that may have entered into the gas phase through evaporation or sublimation and reached the surface of the WE.

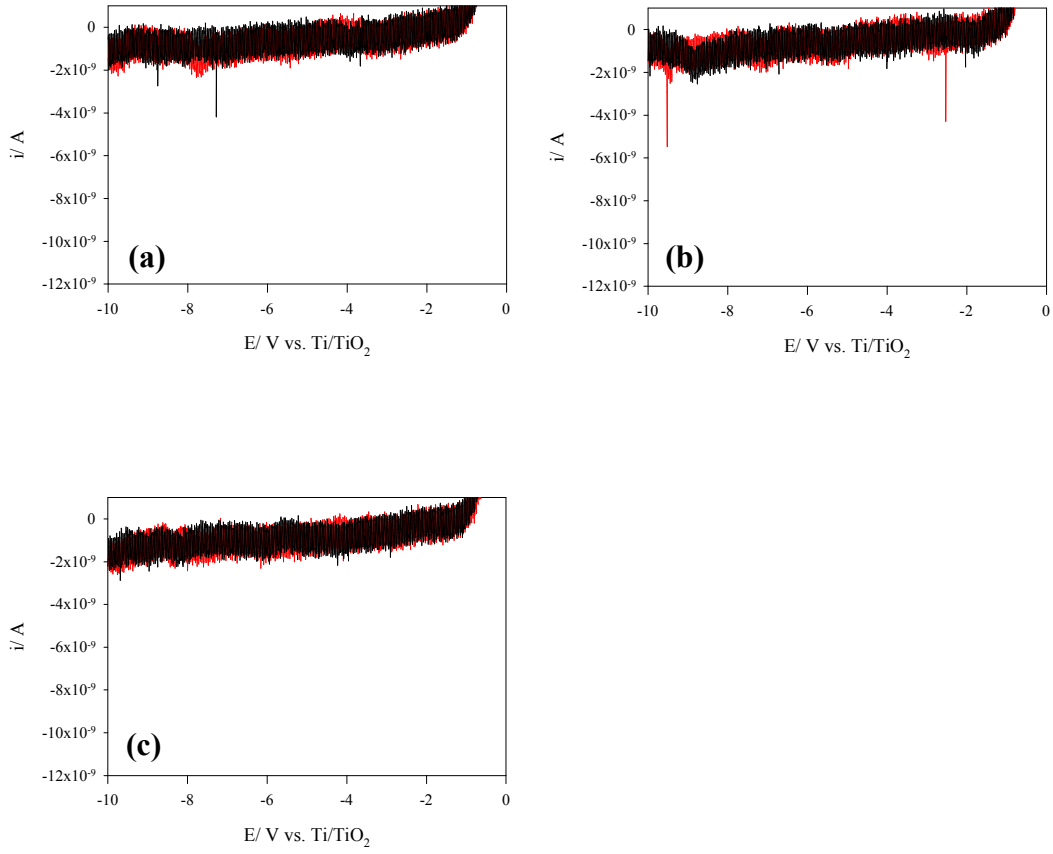

Figure 7-5: A series of successive cyclic voltammograms. (a) 1st scan, (b) 2nd scan, (c) 3rd scan *(forward trace-red and backward trace-black)*, using the Bucket Cell with a Ti/TiO_2 paste RE. Refer to Figure 7-2 caption for details regarding experimental conditions.

Titanium metal wire with oxide pre-treatment reference electrode

A titanium wire (Ti) - similar to that described in Chapter 3, was used as a RE. The wire was pre-treated by being placed into the flame for 30 s to form a solid oxide layer. The electrode was then taken out of the flame before it was incorporated into the 3 electrode assembly and a series of cyclic voltammograms were performed, shown in Figure 7-6.

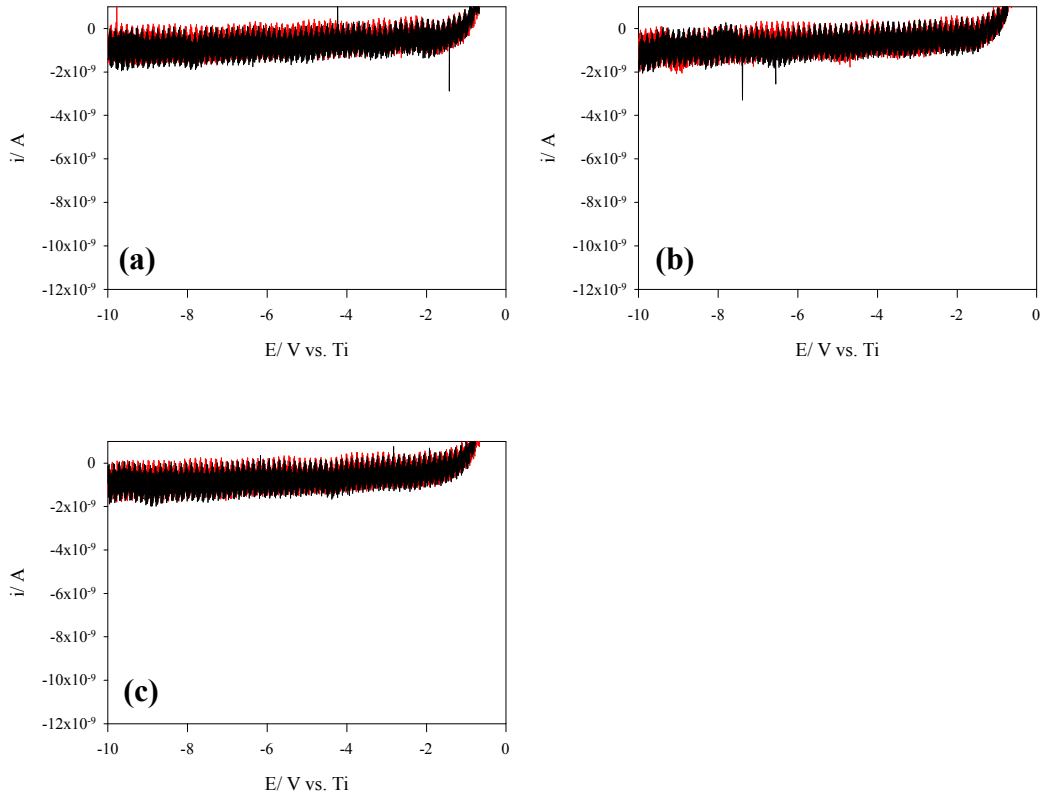

Figure 7-6: A series of successive cyclic voltammograms. (a) 1st scan, (b) 2nd scan, (c) 3rd scan *(forward scan-red and backward scan-black)*, using the Bucket Cell with a 50 mm length Ti metal wire RE. Refer to Figure 7-2 caption for details regarding experimental conditions.

The cyclic voltammograms generated with both the Ti/TiO_2 paste (Figure 7-5) and Ti wire (Figure 7-6) REs are similar and consistent from what would be expected from a bare flame – a flat response/background. The results presented in Chapter 5 (zero current potentiometry and chronopotentiometry experiments) have demonstrated that both REs possess their advantages and drawbacks. The Ti/TiO_2 paste electrode has shown non-polarisable behaviour over a large current range, but over time, it has also showed voltage shifting. In contrast, the Ti wire electrode has also showed non-polarisable behaviour, albeit over a smaller current range, but the voltage was stable over a given length of time.

The Ti wire with its visible coating layer of TiO_2 was chosen as the RE in conjunction with the Bucket Cell to investigate additives introduced into the

flame. The currents expected to be measured were deemed to be within the capability of the Ti wire. The flexibility that can be achieved with using a metal wire electrode is an added advantage for a RE. For example, the wire can easily be modified to move closer towards the WE to reduce the resistance between the two electrodes. In comparison, the rigid structure of the ceramic tube prevents the possibility of modifying the shape or position of the RE.

7.3.2 Doped flame using titanium metal wire with oxide pre-treatment reference electrode

Ammonium molybdate tetrahydrate and ammonium metatungstate hydrate were both introduced as additive into the RHS of the flame (same compartment where the WE was positioned). The LHS flame where the Ti metal wire RE was placed did not contain any additives. A series of cyclic voltammograms with $(NH_4)_6 Mo_7O_{24} \cdot 4H_2O$ present in the flame are shown in Figure 7-7. Each individual scan had a background current of -20 x 10^{-9} A. The forward and backward traces of the 1st scan (Figure 7-7a) were identical with three negative peaks (I, II and III) appearing at 0.5 V, -0.9 V and -2.2 V. These features were also apparent at the same voltage points on both the 2nd scan (Figure 7-7b) and 3rd scan (Figure 7-7c).

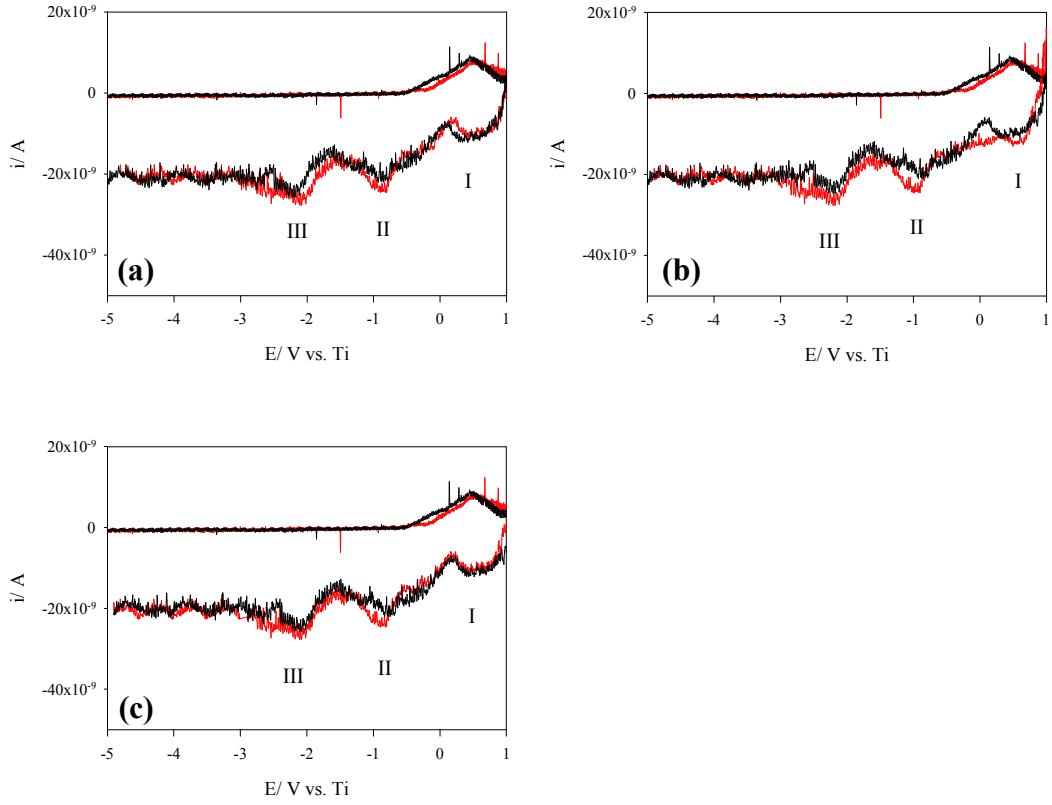

Figure 7-7: A series of successive cyclic voltammograms. (a) 1st scan, (b) 2nd scan, (c) 3rd scan *(forward scan-red and backward scan-black)*, using the Bucket Cell with a 50 mm length Ti metal wire RE which was placed in a flame. The RHS flame was doped with 1 mM ammonium $(NH4)_6Mo_7O_{24} \cdot 4H_20$ with the LHS flame remaining bare. Scan rate 1 V s^{-1}. Voltage swept from 1 to -5 V. The upper scan represents clean water introduced into the flame.

The response generated by introducing $(NH_4)_6H_2W_{12}O_{40} \cdot xH_2O$ into the flame is shown in Figure 7-8.

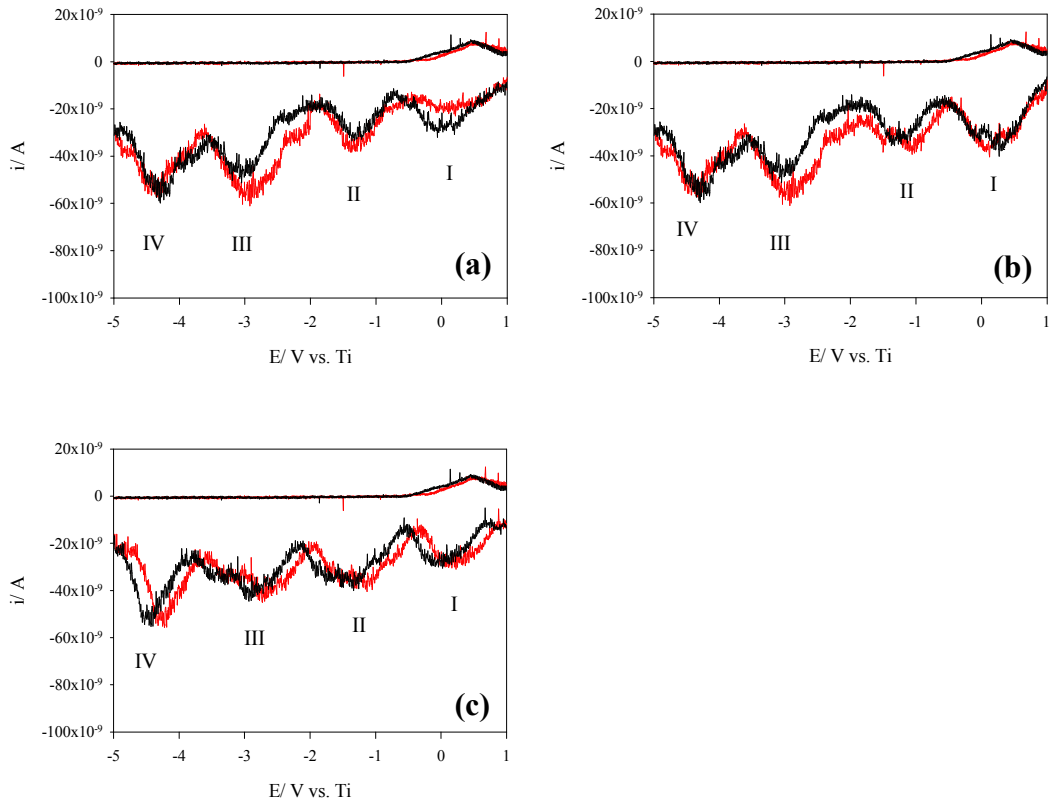

Figure 7-8: A series of successive cyclic voltammograms. (a) 1st scan, (b) 2nd scan, (c) 3rd scan *(forward scan-red and backward scan-black)*, using the Bucket Cell with a 50 mm length Ti metal wire RE. The RHS flame was doped with 1 mM $(NH_4)_6H_2W_{12}O_{40} \cdot xH_2O$ with the LHS flame remaining bare. Refer to Figure 7-7 caption for details regarding experimental conditions.

Similar to the response from introducing $(NH_4)_6Mo_7O_{24} \cdot 4H_2O$ to the flame, the background current of all three scans with $(NH_4)_6H_2W_{12}O_{40} \cdot xH_2O$ was approximately -20 x 10^{-9} A. The forward and backward traces of the 1st scan (Figure 7-8a) are similar with negative peaks observed at the same voltage points. The same peaks were also observed on the forward and backward traces of the 2nd scan (Figure 7-8b) and 3rd scan (Figure 7-8c), which indicates good

reproducibility. The four negative peaks identified (I, II, III and IV) appeared at 0.1 V, -1.3 V, -2.9 V and -4.4 V, respectively.

Through the introduction of $(NH_4)_6Mo_7O_{24} \cdot 4H_2O$ and $(NH_4)_6H_2W_{12}O_{40} \cdot xH_2O$ in the flame, it has been shown they both generate unique and distinctive cyclic voltammograms, with different number of negative peaks appearing at definite voltage positions (summarised in Table 7-1).

Cluster	Peak position (V vs. Ti)
Ammonium molybdate tetrahydrate	0.5, -0.9 and -2.2
Ammonium metatungstate hydrate	0.1, -1.3, -2.9, -and -4.4

Table 7-1: Voltage position of negative peaks observed in cyclic voltammograms for W and Mo metal salt clusters introduced into the flame medium.

Initially, each negative peak in the cyclic voltammogram was associated with the individual cluster that had been introduced into the flame, however it is likely that these clusters will have decomposed to produce mainly their respective metal oxide species, predominantly MoO_3 and WO_3, these being the most stable gas phase oxide of both Mo and W.[130;131] Therefore, the negative peaks observed in the cyclic voltammograms are likely to be due to the reduction of distinct excited state of the oxide species., i.e $MoO_3 + e^- \rightarrow MoO_3^-$ and $WO_3 + e^- \rightarrow WO_3^-$. The peaks observed for these oxides are not due to adsorbed material on the WE. When the clusters were removed from the flame the peaks disappeared from the cyclic voltammogram, even though ex situ Raman spectroscopy showed oxide present on the graphite electrode. This suggests the reduction process takes place exclusively in the gas phase. This idea is supported by the unambiguous correlation of the reduction potentials for peaks obtained for MoO_3 and WO_3, to the vertical detachment energies (VDE) obtained from photoelectron emission spectroscopy (PES) for the oxidation process of MoO_3^- and WO_3^-,[132] as shown in Figure 7-9. In addition, poor correlation was observed

with the VDE of excited states of other oxides, e.g. MoO_x and WO_x where x = 4 and 5, from the same work.

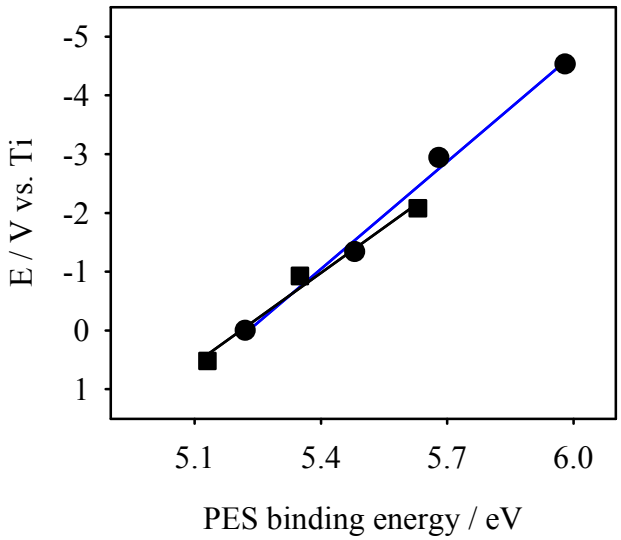

Figure 7-9: Comparison plot of the redox potential measured for peak potentials in the presence of $(NH_4)_6Mo_7O_{24} \cdot 4H_2O$) and $(NH_4)_6H_2W_{12}O_{40} \cdot xH_2O$) against the VDE measured by PES at 193 nm, against MoO_3^- (■) and WO_3^- (●) respectively. PES data from Zhai *et al.*[132]

As the potential is swept from +1 to -5 V, it is the current working assumption that both MoO_3 and WO_3 undergo reduction reactions resulting in the negative peaks observed in the cyclic voltammograms. A schematic energy level diagram for the reduction of MoO_3 in the flame is shown in Figure 7-10.

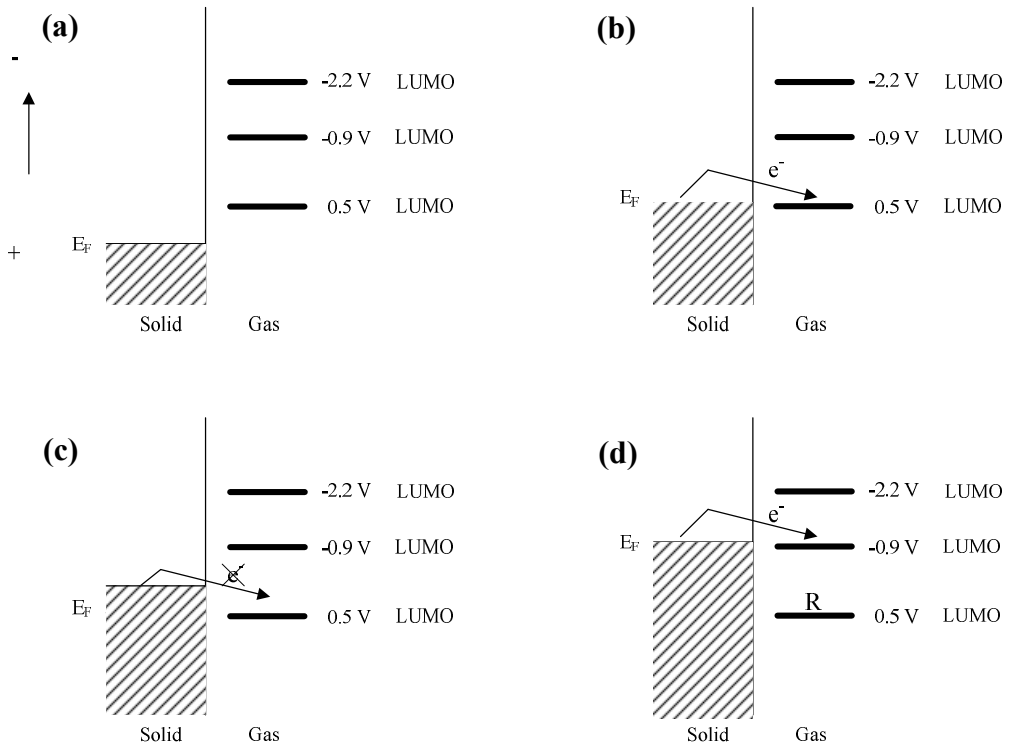

Figure 7-10: Energy states and on an absolute scale, for the gas phase reactant species and the electrons in the solid at different Fermi energies, (a) the electrode potential is insufficient to drive the reduction of a species, (b) electrode potential is at the correct energy level to cause electroreduction at 0.5 V, (c) electrode potential is not at the correct energy level and therefore electron transfer is forbidden, and (d)) electrode potential is at the correct energy level to cause electroreduction at -0.9 V.

The transfer of electrons does not occur in Figure 7-10a because the Fermi Level of the electrode is not high enough to cause electrochemical reduction of MoO_3. Once the energy of the Fermi Level is increased (through the application of a negative electrical potential) and equals the energy of a LUMO level of a free energy state of MoO_3 at 0.5 V, reduction is thermodynamically favourable (Figure 7-10b). The reduction process is accompanied by the increase in current as shown in the cyclic voltammograms. Equally shown in the cyclic voltammograms is the sharp decrease in current which is thought to occur from increasing the Fermi Level of the electrode above the LUMO level (Figure 7-10c). This explanation holds true for gas phase reactions, since the excess reaction energy generated by continued application of a negative voltage cannot

be dissipated into the external environment, resulting in a halt of electron transfer. In contrast and in resemblance to liquid phase reactions, a plateau current would be expected (fast mass transport) for the reduction of adsorbed species on the WE surface. When a large voltage is applied to either a solid or a liquid, it can distribute the excess energy effectively and efficiently to its surrounding environments resulting in continued electron transfer.[6;133] The continuous application of a negative voltage allows the energy of the Fermi Level to match that of the LUMO level of another free energy state of MoO_3 at -0.9 V (Figure 7-10d) and also at -2.2 V. Once the potential has reached -5 V, the potential is swept in the backward direction with the same processes occurring, three identical reduction peaks taking place at identical potentials. The same process can be applied with WO_3 in the flame; four electrochemical reduction processes are seen to take place here.

The height of the negative peaks varied between the two clusters. The cyclic voltammograms with $(NH_4)_6H_2W_{12}O_{40} \cdot xH_2O$ had peak currents *ca*. -6 x 10^{-8} A compared to $(NH_4)_6Mo_7O_{24} \cdot 4H_2O$ which had peak currents *ca*. -3 x 10^{-8} A. The difference is thought to be due to the stoichiometry of the metal per mole of cluster. The $(NH_4)_6H_2W_{12}O_{40} \cdot xH_2O$ cluster introduced into the flame contained 12 W atoms per mole of cluster, whereas the $(NH_4)_6Mo_7O_{24} \cdot 4H_2O$ contained 7 Mo atoms per mole of cluster, hence the difference in current responses between the two compounds. The number of and position of the peaks are clearly dependent on the identity of the cluster introduced into the flame, and together with their quantitative nature is strong evidence supporting that the peaks are Faradaic in nature.

The Faradaic nature of the peaks is further demonstrated by their dependence on concentration of $(NH_4)_6H_2W_{12}O_{40} \cdot xH_2O$. Figure 7-11a shows all four peaks are concentration dependent.

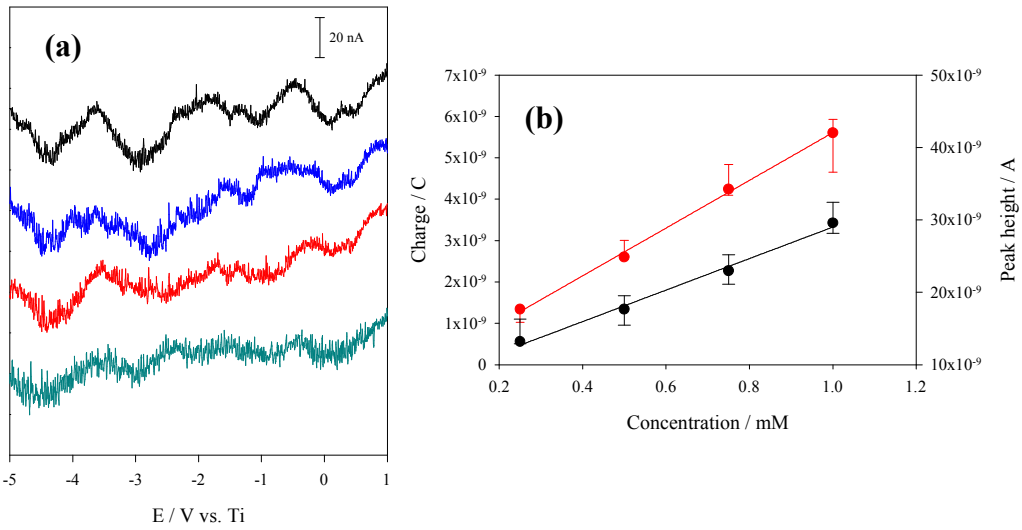

Figure 7-11: Cyclic voltammograms (forward trace only) of varying concentration of $(NH_4)_6H_2W_{12}O_{40} \cdot xH_2O$) – 1 mM (black), 0.75 mM (blue), 0.50 mM (red), and 0.25 mM (cyan). (b) Plot of charge (red) and peak height at -2.9 V (black) versus concentration. Refer to Figure 7-7 caption for details regarding experimental conditions.

When the peak at -2.9 V was analysed, it showed a clear dependence of the integrated charge and height on the concentration of $(NH_4)_6H_2W_{12}O_{40} \cdot xH_2O$ in the solution introduced into the flame between 0.25 to 1 mM (Figure 7-11b). The quantitative nature of these peaks presents further evidence that the features recorded in the voltammograms are due to the electroreduction of species in the flame and reacting at the electrode surface.

7.4 Summary

Four REs have each been incorporated as part of the Bucket Cell. A series of cyclic voltammograms were recorded with no additives introduced into the flame. The results suggested that Ti metal wire was the most suitable RE to continue investigations while additives were introduced into the flame. Three negative peaks were observed when $(NH_4)_6Mo_7O_{24} \cdot 4H_2O$ was used as an

additive. In contrast, four negative peaks were observed when $(NH_4)_6H_2W_{12}O_{40} \cdot xH_2O$ clusters were introduced into the flame as an additive. Critically, the four peaks are positioned at different voltage points when compared to the three peaks seen with $(NH_4)_6Mo_7O_{24} \cdot 4H_2O$. The responses were reproducible indicating that these unique cyclic voltammograms could be used to characterise compounds introduced into the flame as additives. The current assumption for the origin of the peaks, supported by PES, is that they correspond to the reduction of distinct excited states of the metal oxides.

8 Conclusion and Suggestions for Future Work

Conclusion

The development of an electrochemical cell suitable for high temperature gas phase dynamic electrochemistry has until this present study remained undeveloped. An early literature review revealed electrochemistry had primarily been restricted to the liquid phase, with only a small amount of electrochemistry literature in the gas phase. This thesis has described the development of a 3-electrode assembly which was used to characterise two metal salt clusters that were individually introduced into the flame. The resulting cyclic voltammograms of the clusters had different and distinctive features which were reproducible. The Faradaic features were ascribed to the direct electroreduction of the metal oxides that were formed in the flame.

A considerable amount of research was undertaken to construct a non-polarisable reference electrode (RE) that could be used in a high temperature medium. A non-polarisable electrode was needed to ensure that the voltage applied to the working electrode (WE) during an electrochemical measurement was stable and accurate. Three types of REs were designed and studied to assess their voltage stability and polarisability. The REs studied were metal wires, a dynamic-type electrode, and metal/metal oxide pastes packed into ceramic supports.

Once the metal wires were placed into oxygen-containing flame, oxide layers surrounding the metal wires were formed. In some cases, i.e. titanium (Ti) and niobium (Nb) wires, a solid oxide layer was found to form on the surface of the wire. This was due to the sublimation temperature of the metal oxides being higher than the flame temperatures. In contrast, metal wires such as tungsten (W) and molybdenum (Mo) formed gaseous oxide sheaths in the close vicinity of the wires because their metal oxides had sublimation temperatures well below that of the flame temperature. Zero current measurements of the metal wires against a

graphite rod showed a wide range of voltages, demonstrating that each individual material was contributing to the potential difference observed.

Although all metal wires formed oxides, it was found through chronopotentiometry measurements that W and Mo showed least polarisability compared to the other two materials. The difference in behaviour was thought to be associated to the type of oxide layer formed in the flame. The formation of the gaseous sheath containing the metal's ions and/or oxide was thought to have increased the desired non-polarisability feature. However, as a direct consequence of the gaseous sheath, the rate of oxide sublimation and evaporation was increased. This was reflected in voltage measurements which showed poor voltage stability and large noise for W and Mo wires. Both Ti and Nb wires showed similar polarisability behaviour; however, the voltage stabilised faster with Ti wire compared to Nb wire.

The dynamic RE was designed and created to increase the voltage stability and reduce the noise of W and Mo wires. The wires were both polarised positive and negative with respect to a platinum (Pt) coil to keep the voltage stable. The coil was also used as a shield to reduce the extent of sublimation and evaporation of the wire in the flame. When the W wire was polarised positive, the noise could not be increased or reduced by applying a voltage. In contrast, when the polarity was reversed and the tungsten wire was polarised negative, the noise increased by the applied voltage. It was thought that the applied voltage serve to move the equilibrium potential more negative causing the metal oxide to be reduced to its metal. The loosely-bound metal particles were then instantaneously re-oxidised in the oxygen-containing flame causing also loosely-bound oxide particles, which evaporated easily off the surface of the electrode. By applying a more negative voltage, the rate of oxide evaporation that formed on the surface of the electrode could be increased.

To investigate the materials that formed solid oxide layers surrounding their metal wires, Ti was chosen over Nb because its voltage became and remained

stable faster. The REs were made from pastes containing Ti and TiO_2 which were packed into ceramic supports. Once placed in the flame, the pastes became sintered and resembled pellet-like structures. The advantage of using pastes was control of the metal and metal oxide compositions. Electrochemical measurements coupled with ex-situ characterisation studies indicated that the potential recorded was initially due to a complex process involving many Ti based materials (phase I), followed by conductivity being solely dependent upon TiO_2 (phase II).

The Bucket cell was developed to incorporate both the working and counter electrodes. A thick Pt disc with a 3 mm diameter hole in the centre was used as a counter electrode (CE). The disc was embedded on a stainless steel support. The graphite rod WE was mechanically trimmed to 2.7 mm and allowed to protrude through the centre hole of the disc. The close proximity of the WE to the CE ensured full control of the WE surface area exposed to the flame.

Each type of RE described here was used in conjunction with the Bucket Cell to obtain a cyclic voltammogram in a clean flame. The responses using a Ti wire that was pre-treated (an oxide layer was allowed to develop in the flame for 30 s) showed the most reproducible and clean responses. Two metal salt clusters were introduced into the flame and both sets of cyclic voltammograms showed different features which were believed to be due to the complexes introduced into the flame. Three negative peaks were observed when ammonium molybdate tetrahydrate was aspirated into the flame. In contrast, four negative peaks were observed when ammonium metatungstate hydrate was introduced into the flame as an additive. The reproducible responses indicate that these unique cyclic voltammograms could be used as a characterising tool to identify additives introduced into the flame. Cyclic voltammograms using the other types of REs have yet to be obtained while the same metal salt clusters were introduced into the flame.

Suggestions for Future Work

To improve standardisation and optimisation of the electrode assembly, the choice of electrode material and electrode assembly could be altered or modified. The RE could be incorporated into the Bucket cell as shown in Figure 8-1.

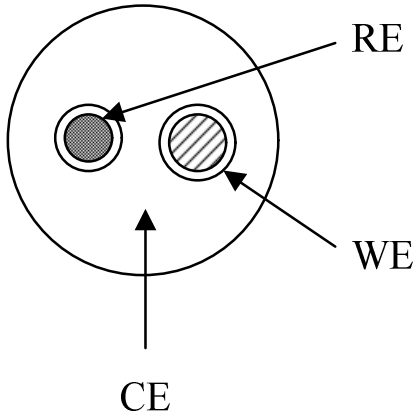

Figure 8-1: Cross sectional view of the platinum counter electrode with two drill holes for the graphite working electrode and the reference electrode to be placed together in the same location in the flame during each experiment (not drawn to scale).

This should not only increase the precision of the RE location in the flame but also in relation to the WE. The graphite WE, which has discrete energy levels, should be replaced with Pt metal that has a continuous energy level. Cyclic voltammograms should be collected in a bare and doped flame and responses compared with those presented in this study. Early investigation within the group has shown there to be no difference in the responses when the two materials are used. The size of the WE could be varied to demonstrate the dependence of measured current on the surface area exposed to the flame.

Once the electrode assembly is satisfactorily optimised, the identity of species in the flame should be of upmost importance. Until now, we have assumed that metal containing compounds oxidise once they enter the flame. The identity of metal ion or oxides will aid to describe the chemical reactions taking place in the gas phase and those that may take place on the surface of the WE. Mass

spectroscopy is unlikely to be useful tool to sample the flame because measurements need to be taken under vacuum. Since the flame is at atmospheric pressure, the probability of sampling the identified species is not possible since the mean free path is likely to be large causing collisions to occur between other species, hence giving the researcher a false identification of the actual flame species. A possible alternative technique is cavity ring–down spectroscopy which has been used in the past used to study gaseous samples which absorb light at specific wavelengths, and consequently being able to determine concentration of the species in the gas phase. *In situ* Surface Enhanced Raman Spectroscopy (SERS) could possibly be used to investigate the surface of the WE for different oxidation states of metals that are absorbed onto the surface. In conjunction with SERS, potential step experiments could be conducted to show a direct relationship between the product of the electrochemical reduced species and applied potential.

The potential window between 1 V and -5 V has been extensively studied; however the window can be further extended to investigate other electrochemical reactions that may take place at further negative potentials. Currently, the voltage stability of the titanium metal wire reference electrode decreases as the window is expanded. The consequence of poor reference voltage stability was cyclic voltammograms with negative peaks still being observed, however they were irreproducible occurring at different potentials. To increase the reference voltage stability while the potential window is widened, the reference electrode made using titanium – titanium dioxide pastes packed into ceramic supports should be further investigated since the relative composition of the metal and metal oxide can be manipulated to obtain the optimum composition. In conjunction with this, the alignment of the RE potential scale with the normal hydrogen electrode or absolute potential scale is still unclear and needs to be investigated.

By adopting a seemingly uncomplicated electrochemical approach, a tool has been developed to study and control electron transfer events at the solid/gas interface. The results presented in this thesis have wide implications which are of

theoretical and technological significance. There are theoretical avenues for research to develop a quantum mechanical level understanding of electron transfer reactions at the solid/gas interface. The scope of technological impact is extensive. The absence of solvent opens the possibility of NO_x and CO_2 electrolysis for management of pollutants or green-house gases with the application of non-thermal technological plasmas. The method extends the utility of plasmas in electrochemistry, beyond conductivity probes for the development of new plasma diagnostic tool.[59;134] Also quantitative gas phase voltammetry may be developed, complementing analytical techniques such as atomic absorption, inductively coupled plasma and fluorescence spectroscopies. In addition, the impact on other less well established fields such as electrostatic charging,[135;136] catalysis[137;138] and astrochemistry[139] where solid/gas surface redox reactions may also be anticipated.

REFERENCES

1. Goodings, J. M.; Guo, J. Z.; Laframboise, J. G. *Electrochemistry Communications* **2002,** *4*, 363-69.

2. Ingolfsson, O.; Weik, F.; Illenberger, E. *International Journal of Mass Spectrometry and Ion Processes* **1996,** *155*, 1-68.

3. Illenberger, E. *Chemical Reviews* **1992,** *92*, 1589-609.

4. Southampton Electrochemistry Group, U. o. S. Instrumental Methods in Electrochemistry, Ellis Horwood: New York, 1993.

5. Monk, P. M. Fundamentals of Electroanalytical Chemistry, John Wiley & Sons Ltd: 2001.

6. Bard, A. J.; Faulkner, A. J. Electrochemical methods. Fundamentals and Applications, 2nd ed.; John Wiley & Sons, Inc: 2001.

7. Abbott, A. P.; McKenzie, K. J. *Physical Chemistry Chemical Physics* **2006,** *8*, 4265-79.

8. Smirnov, B. M. Physics of Ionized Gases, John Wiley & Sons, Inc: 2001.

9. Fridman, A.; Chirokov, A.; Gutsol, A. *Journal of Physics D-Applied Physics* **2005,** *38*, R1-R24.

10. Hippler, R.; Pfau, S.; Schmidt, M. Low Temperature Plasma Physics, Wiley-VCH: 2001.

11. Aydil, E. S.; Economou, D. J. *Journal of the Electrochemical Society* **1992,** *139*, 1396-406.

12. Liston, E. M.; Martinu, L.; Wertheimer, M. R. *Journal of Adhesion Science and Technology* **1993,** *7*, 1091-127.

13. Graves, D. B. *Ieee Transactions on Plasma Science* **1994,** *22*, 31-42.

14. Janek, J.; Rosenkranz, C. *Journal of Physical Chemistry B* **1997,** *101*, 5909-12.

15. Vennekamp, M.; Janek, J. *Solid State Ionics* **2001,** *141*, 71-80.

16. Bogaerts, A.; Neyts, E.; Gijbels, R.; van der Mullen, J. *Spectrochimica Acta Part B-Atomic Spectroscopy* **2002,** *57*, 609-58.

17. Mollah, M. Y. A.; Schennach, R.; Patscheider, J.; Promreuk, S.; Cocke, D. L. *Journal of Hazardous Materials* **2000,** *B79*, 301-20.

18. Hopwood, J. *Plasma Sources Science & Technology* **1992,** *1*, 109-16.

19. Vennekamp, M.; Janek, J. *Zeitschrift fur Anorganische und Allgemeine Chemie* **2003,** *629*, 1851-62.

20. Vennekamp, M.; Janek, J. *Journal of the Electrochemical Society* **2003,** *150*, C723-C729.

21. Vennekamp, M.; Janek, J. *Physical Chemistry Chemical Physics* **2005,** *7*, 666-77.

22. Park, S. K.; Economou, D. J. *Journal of Applied Physics* **1990,** *68*, 3904-15.

23. Ogumi, Z.; Uchimoto, Y.; Tsuji, Y.; Takehara, Z. *Journal of Applied Physics* **1992,** *72*, 1577-82.

24. Ogumi, Z.; Uchimoto, Y.; Takehara, Z. *Advanced Materials* **1995,** *7*, 323-25.

25. Chiodelli, G.; Magistris, A.; Scagliotti, M.; Parmigiani, F. *Journal of Materials Science* **1988,** *23*, 1159-63.

26. Negishi, A.; Nozaki, K.; Ozawa, T. *Solid State Ionics* **1981,** *3-4*, 443-46.

27. Economou, D. J.; Park, S. K.; Williams, G. D. *Journal of the Electrochemical Society* **1989,** *136*, 188-98.

28. Yamane, H.; Hirai, T. *Journal of Crystal Growth* **1989,** *94*, 880-84.

29. Kawabuchi, K.; Magari, S. *Journal of Applied Physics* **1979,** *50*, 6222-29.

30. Axford, S. D. T.; Goodings, J. M.; Hayhurst, A. N. *Combustion and Flame* **1998,** *114*, 294-302.

31. Berden, G.; Peeters, R.; Meijer, G. *International Reviews in Physical Chemistry* **2000,** *19*, 565-607.

32. Goodings, J. M. *Abstracts of Papers of the American Chemical Society* **1991,** *202*, 201-HYS.

33. Caruana, D. J.; McCormack, S. P. *Electrochemistry Communications* **2000,** *2*, 816-21.

34. Caruana, D. J.; McCormack, S. P. *Electrochemistry Communications* **2001,** *3*, 675-81.

35. Mallard, W. G.; Smyth, K. C. *Combustion and Flame* **1982,** *44*, 61-70.

36. Clements, R. M.; Smy, P. R. *Journal of Physics D: Applied Physics* **1974,** *7*, 551-62.

37. Hadzifejzovic, E.; Stankovic, J.; Firth, S.; McMillan, P. F.; Caruana, D. J. *Phys.Chem.Chem.Phys.* **2007,** *9*, 5335-39.

38. Fristrom, R. M. Flame Structure and processes, Oxford university Press: 1995.

39. Fristrom, R. M. *Pure and Applied Chemistry* **1990,** *62*, 839-49.

40. Gaydon, A. G.; Wolfhard, H. G. Flames. Their structure, radiation and temperature, 4th ed.; Chapman and Hall Ltd: 1979.

41. Ray, S. R.; Fernandezpello, A. C.; Glassman, I. *Journal of Heat Transfer-Transactions of the Asme* **1980,** *102*, 357-63.

42. Glassman, I. Combustion, Academic Press: 1996.

43. Eberius, K. H.; Hoyermann, K.; Wagner, H. G. *Symposium (International) on Combustion* **1971,** *13*, 713-21.

44. Brown, N. J.; Fristrom, R. M.; Sawyer, R. F. *Combustion and Flame* **1974,** *23*, 269-75.

45. Brown, N. J.; Eberius, K. H.; Fristrom, R. M.; Hoyermann, K. H.; Wagner, H. G. *Combustion and Flame* **1978,** *33*, 151-60.

46. Axford, S. D. T.; Hayhurst, A. N. *Journal of the Chemical Society-Faraday Transactions* **1995,** *91*, 827-33.

47. Ashton, A. F.; Hayhurst, A. N. *Combustion and Flame* **1973,** *21*, 69-75.

48. Jensen, D. E.; Padley, P. J. *Transactions of the Faraday Society* **1966,** *62*, 2140-49.

49. Kelly, R.; Padley, P. J. *Transactions of the Faraday Society* **1969,** *65*, 355-66.

50. Axford, S. D. T.; Hayhurst, A. N. *Journal of the Chemical Society-Faraday Transactions* **1995,** *91*, 835-41.

51. Mott-Smith, H. M.; Langmuir, I. *Physical Review* **1926,** *28*, 727-63.

52. Calcote, H. F. *Symposium (International) on Combustion* **1963,** *9*, 622-37.

53. Bradley, D.; Ibrahim, S. M. A. *Journal of Physics D-Applied Physics* **1974,** *7*, 1377-90.

54. Bradley, D.; Ibrahim, S. M. A. *Journal of Physics D-Applied Physics* **1973,** *6*, 465-78.

55. Calcote, H. F.; King, I. R. *Symposium (International) on Combustion* **1955,** *5*, 423-34.

56. Travers, B. E. L.; Williams, H. *Symposium (International) on Combustion* **1965,** *10*, 657-72.

57. Maclatchy, C. S. *Combustion and Flame* **1979,** *36*, 171-78.

58. D'Arcy, R. J. *Journal of Physics D: Applied Physics* **1974,** *7*, 1391-401.

59. King, I. R.; Calcote, H. F. *Journal of Chemical Physics* **1955,** *23*, 2203-04.

60. Guo, J.; Goodings, J. M. *Chemical Physics Letters* **2000,** *329*, 393-98.

61. Gileadi, E. Electrode Kinetics for Chemists, Chemical Engineers, and Materials Scientist, VCH Publishers, Inc.: 1993.

62. Vijh, A. K. *Surface Technology* **1985,** *25*, 335-41.

63. Vijh, A. K. *Materials Chemistry and Physics* **1986,** *14*, 47-56.

64. Wetzel, D. M.; Brauman, J. I. *Chemical Reviews* **1987,** *87*, 607-22.

65. A.C.Fisher Electrode Dynamics, Oxford University Press: 1996.

66. Rieger, P. H. Electrochemistry, 2nd ed.; Chapman & Hall, Inc.: New York, 1994.

67. Bagotsky, V. S. Fundamentals of Electrochemistry, 2nd ed.; John Wiley & Sons, Inc.: New Jersey, 2006.

68. Turrell, G.; Corset, J. Raman Microscopy, Academic Press Limited: London, 1996.

69. Einstein, A. *Annalen der Physik* **1905,** *17*, 132-48.

70. Berglund, C. N.; Spicer, W. E. *Physical Review A-General Physics* **1964,** *136*, 1030-&.

71. Koopmans, T. Ordering of Wave Functions and Eigenenergies to the Individual Electrons of an Atom. Physica 1, 104-113. 1933.
Ref Type: Journal (Full)

72. Ladd, M.; Palmer, R. Structure Determination by X-ray Crystallography, 4th ed.; Kluwer Academic / Plenum Publishers: New York, 2003.

73. Will, G. Powder Diffraction: The Rietveld Method and the Two-Stage Method to Determine and Refine Crystal Structures from Powder Diffraction Data, Springer: Berlin, 2006.

74. Krawitz, A. D. Introduction to diffraction in materials science and engineering, John Wiley & Sons, Inc.: New York, 2001.

75. Jaffe, H. W. Introduction to crystal chemistry, Student ed.; Cambridge University Press: Cambridge, 1988.

76. Bragg, W. L. The Development of X-ray Analysis, G. Bell and Sons Ltd: London, 1975.

77. Warren, B. E. X-Ray Diffraction, Dover Publications, Inc.: New York, 1990.

78. Authier, A.; Lagomarsino, S.; Tanner, B. X-Ray and Neutron Dynamical Diffraction: Theory and Applications, Plenum Press: New York and London, 1996.

79. Buerger; M.J. Elementary crystallography: an introduction to the fundamental geometrical features of crystals, Revised ed.; The MIT Press: Cambridge, 1978.

80. Khanna.Y.P. A Guide to Materials Characterization and Chemical Analysis, 2nd ed.; VCH Publishers, Inc.: New York, 1996.

81. Gabbott, P. Principles and Applications of Thermal Analysis, Blackwell Publishing Ltd: Oxford, 2008.

82. Sorai, M. Comprehensive Handbook of Calorimetry & Thermal analysis, John Wiley & Sons: Chichester, 2004.

83. Haines, P. J. Principles of Thermal Analysis and Calorimetry, The Royal Society of Chemistry: Cambridge, 2002.

84. Mackenzie, R. C. Differential Thermal Analysis, Academic Press Inc.: London, 1970.

85. Lide, D. R. Handbook of Chemistry and Physics, 73rd ed.; CRC Press: 1992.

86. Behr, M. J.; Gaulding, E. A.; Mkhoyan, K. A.; Aydil, E. S. *Journal of Vacuum Science & Technology B* **2010,** *28*, 1187-94.

87. Donnelly, C. M.; McCullough, R. W.; Geddes, J. *Diamond and Related Materials* **1997,** *6*, 787-90.

88. Refke, A.; Philipps, V.; Vietzke, E. *Journal of Nuclear Materials* **1997,** *250*, 13-22.

89. Skinner, S. J.; Kilner, J. A. *Materials Today* **2003,** *6*, 30-37.

90. Rohnke, M.; Janek, J.; Kilner, J. A.; Chater, R. J. *Solid State Ionics* **2004,** *166*, 89-102.

91. Vogtenhuber, D.; Podloucky, R.; Neckel, A.; Steinemann, S. G.; Freeman, A. J. *Physical Review B* **1994,** *49*, 2099-103.

92. Lindau, I.; Spicer, W. E. *Journal of Applied Physics* **1974,** *45*, 3720-25.

93. Gong, S. L.; Lu, J. T.; Yan, H. Q. *Journal of Electroanalytical Chemistry* **1997,** *436*, 291-93.

94. Giner, J. *Journal of the Electrochemical Society* **1964,** *111*, 376-77.

95. Zhang, M. S.; Yin, Z.; Chen, Q. *Fourteenth International Conference on Raman Spectroscopy* **1994,** 730-31.

96. Ma, H. L.; Yang, J. Y.; Dai, Y.; Zhang, Y. B.; Lu, B.; Ma, G. H. *Applied Surface Science* **2007,** *253*, 7497-500.

97. Chen, C. A.; Huang, Y. S.; Chung, W. H.; Tsai, D. S.; Tiong, K. K. *Journal of Materials Science-Materials in Electronics* **2009,** *20*, 303-06.

98. Mazza, T.; Barborini, E.; Piseri, P.; Milani, P.; Cattaneo, D.; Bassi, A. L.; Bottani, C. E.; Ducati, C. *Physical Review B* **2007,** *75*.

99. Kondo, S.; Tateishi, K.; Ishizawa, N. *Japanese Journal of Applied Physics* **2008,** *47*, 616-19.

100. Onoda, M. *Journal of Solid State Chemistry* **1998,** *136*, 67-73.

101. Liu, G. H.; Chen, K. X.; Zhou, H. P.; Ren, K. G. *Journal of the American Ceramic Society* **2007,** *90*, 2918-25.

102. Hyett, G.; Green, M. A.; Parkin, I. P. *Journal of the American Chemical Society* **2007,** *129*, 15541-48.

103. Bokhimi, X.; Morales, A.; Pedraza, F. *Journal of Solid State Chemistry* **2002,** *169*, 176-81.

104. Baumard, J. F.; Panis, D.; Anthony, A. M. *Journal of Solid State Chemistry* **1977,** *20*, 43-51.

105. Afir, A.; Achour, M.; Saoula, N. *Journal of Alloys and Compounds* **1999,** *288*, 124-40.

106. Swift, G. A.; Koc, R. *Journal of Materials Science* **1999,** *34*, 3083-93.

107. Montero, I.; Jimenez, C.; Perriere, J. *Surface Science* **1991,** *251*, 1038-43.

108. Jiang, C. C.; Goto, T.; Hirai, T. *Journal of Alloys and Compounds* **1993,** *190*, 197-200.

109. Zhecheva, A.; Sha, W.; Malinov, S.; Long, A. *Surface & Coatings Technology* **2005,** *200*, 2192-207.

110. Ajikumar, P. K.; Kamruddin, M.; Shankar, P.; Gouda, R.; Balamurugan, A. K.; Nithya, R.; Tyagi, A. K.; Jayaram, V.; Biswas, S. K.; Raj, B. *Scripta Materialia* **2009,** *61*, 403-06.

111. Lu, F. H.; Jiang, B. F.; Lo, J. L.; Chan, M. H. *Journal of Materials Research* **2009,** *24*, 2400-08.

112. Ernsberger, C.; Nickerson, J.; Smith, T. *Journal of Vacuum Science & Technology A-Vacuum Surfaces and Films* **1986,** *4*, 2784-88.

113. Wu, H. Z.; Chou, T. C.; Mishra, A.; Anderson, D. R.; Lampert, J. K.; Gujrathi, S. C. *Thin Solid Films* **1990,** *191*, 55-67.

114. Saha, N. C.; Tompkins, H. G. *Journal of Applied Physics* **1992,** *72*, 3072-79.

115. Lu, F. H.; Lo, J. L. *Journal of the European Ceramic Society* **2002,** *22*, 1367-74.

116. Desmaison, J.; Lefort, P.; Billy, M. *Oxidation of Metals* **1979,** *13*, 505-17.

117. Dittrich, T.; Weidmann, J.; Koch, F.; Uhlendorf, I.; Lauermann, I. *Applied Physics Letters* **1999,** *75*, 3980-82.

118. Bak, T.; Nowotny, J.; Stranger, J. *Ionics* **2010,** *16*, 673-79.

119. Yildiz, A.; Lisesivdin, S. B.; Kasap, M.; Mardare, D. *Optoelectronics and Advanced Materials-Rapid Communications* **2007,** *1*, 531-33.

120. Reyes-Coronado, D.; Rodriguez-Gattorno, G.; Espinosa-Pesqueira, M. E.; Cab, C.; de Coss, R.; Oskam, G. *Nanotechnology* **2008,** *19*.

121. Mikhailov, M. M. *Inorganic Materials* **2004,** *40*, 1054-57.

122. Batzill, M.; Morales, E. H.; Diebold, U. *Physical Review Letters* **2006,** *96*.

123. Diebold, U. *Surface Science Reports* **2003,** *48*, 53-229.

124. Nowotny, J.; Bak, T.; Nowotny, M. K.; Sheppard, L. R. *Journal of Physical Chemistry C* **2008,** *112*, 602-10.

125. Nowotny, J.; Radecka, M.; Rekas, M.; Sugihara, S.; Vance, E. R.; Weppner, W. *Ceramics International* **1998,** *24*, 571-77.

126. Bak, T.; Nowotny, M. K.; Sheppard, L. R.; Nowotny, J. *Journal of Physical Chemistry C* **2008,** *112*, 12981-87.

127. Galiani, J. A. S.; Hadzifejzovic, E.; Harvey, R. A.; Caruana, D. J. *Electrochimica Acta* **2008,** *53*, 3271-78.

128. Baserga, A.; Russo, V.; Di Fonzo, F.; Bailini, A.; Cattaneo, D.; Casari, C. S.; Bassi, A. L.; Bottani, C. E. *Thin Solid Films* **2007,** *515*, 6465-69.

129. Cazzanelli, E.; Vinegoni, C.; Mariotto, G.; Kuzmin, A.; Purans, J. *Journal of Solid State Chemistry* **1999,** *143*, 24-32.

130. Schofield, K. *Energy & Fuels* **2003,** *17*, 191-203.

131. Schofield, K. *Energy & Fuels* **2005,** *19*, 1898-905.

132. Zhai, H. J.; Kiran, B.; Cui, L. F.; Li, X.; Dixon, D. A.; Wang, L. S. *Journal of the American Chemical Society* **2004,** *126*, 16134-41.

133. Kissinger, P. T.; Heineman, W. R. Laboratory Techniques in Electroanalytical Chemistry*,* 2nd ed.; Marcel Dekker, Inc.: 2011.

134. Maclatchy, C. S.; Smith, H. C. L. *Ieee Transactions on Plasma Science* **1991,** *19*, 1254-58.

135. McCarty, L. S.; Winkleman, A.; Whitesides, G. M. *Journal of the American Chemical Society* **2007,** *129*, 4075-88.

136. Liu, C. y.; Bard, A. J. *Journal of the American Chemical Society* **2009,** *131*, 6397-401.

137. Wilson, E.; Grau-Crespo, R.; Pang, C.; Cabailh, G.; Chen, Q.; Purton, J.; Catlow, C.; Brown, W.; de Leeuw, N.; Thornton, G. *Journal of Physical Chemistry C* **2008,** *112*, 10918-22.

138. McKenna, K. P.; Shluger, A. L. *Nature Materials* **2008,** *7*, 859-62.

139. Caruana, D. J.; Holt, K. B. *Physical Chemistry Chemical Physics* **2010,** *12*, 3072-79.